



UNIVERSITÀ
DEGLI STUDI
DI PADOVA

UNIVERSITÀ DEGLI STUDI DI PADOVA

Dipartimento di Ingegneria Civile, Edile e Ambientale (ICEA)

SCUOLA DI DOTTORATO DI RICERCA IN
SCIENZE DELL' INGEGNERIA CIVILE ED AMBIENTALE
XXVIII CICLO

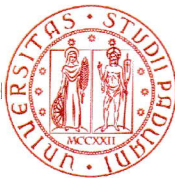
**RAINFALL-INDUCED LANDSLIDES: SIMULATION AND VALIDATION
THROUGH CASE STUDIES WITH A MULTIPHASE POROUS MEDIA
MODEL IN CONJUNCTION WITH THE SECOND ORDER WORK
CRITERION**

Direttore della Scuola: Ch.mo Prof. Stefano Lanzoni

Supervisori: Ch.mo Prof. Lorenzo Sanavia

Ch.mo Prof. Bernhard Schrefler

Dottoranda: Evanthia Kakogiannou



UNIVERSITÀ
DEGLI STUDI
DI PADOVA

UNIVERSITÀ DEGLI STUDI DI PADOVA

Dipartimento di Ingegneria Civile, Edile e Ambientale (ICEA)

SCUOLA DI DOTTORATO DI RICERCA IN
SCIENZE DELL' INGEGNERIA CIVILE ED AMBIENTALE
XXVIII CICLO

**RAINFALL-INDUCED LANDSLIDES: SIMULATION AND VALIDATION
THROUGH CASE STUDIES WITH A MULTIPHASE POROUS MEDIA
MODEL IN CONJUNCTION WITH THE SECOND ORDER WORK
CRITERION**

Direttore della Scuola: Ch.mo Prof. Stefano Lanzoni

Supervisor: Ch.mo Prof. Lorenzo Sanavia

Ch.mo Prof. Bernhard Schrefler

Dottoranda: Evanthia Kakogiannou

ACKNOWLEDGEMENTS

First and foremost, I would like to express my sincere gratitude to my thesis supervisors, Prof. Lorenzo Sanavia and Prof. Bernhard Schrefler, for giving me the opportunity to carry out this PhD thesis at the ICEA department, at the University of Padova. I am particularly grateful for their support and their patient guidance on this research work, as well as for giving me the opportunity to present my work at several international schools, meetings and conferences.

I wish to express my sincere thanks to Prof. François Nicot for welcoming me so warmly at IRSTEA Institute in Grenoble during my secondment; for his constant support and for his willingness to devote time so generously to work with me and answer to all my questions concerning the second order work criterion. I would also like to thank Prof. Félix Darve for his collaboration and all his valuable remarks.

Many thanks are also directed to Dr. Marco Lora and his supervisor Prof. Paolo Salandin for their collaboration concerning the analysis of the slope stability experimental test. Thank you Marco for trusting me your work and your data, for our useful discussions and your very good sense of humour.

I could not forget at this point Prof. Simonetta Cola, who contributed significantly to my understanding of the Pastor-Zienkiewicz constitutive model. Many thanks Professor! I would also like to thank Researcher Dr. Fabio Gabrieli and Dr. Francesca Ceccato for the useful scientific discussions that we had.

I wish to express also my special thanks to Prof. Pablo Mira who reviewed and evaluated this thesis.

My thanks are also directed to all the members of MuMoLaDe Project team (7th Framework Programme of the European Union-ITN MuMoLaDe project 289911) especially Prof. Wei Wu for coordinating the Project and all of the former PhD students and Postdocs: Aleksandra Jakubczyk, Xiaogang Guo, Caroline Chalak, Maria Lazari, Konstantin Melnikov, Barbara Switala, Lorenzo Benedetti, Alessandro Leonardi, Xiannan Meng, Pablo Agustín Becker, Adel Albaba, Vasileios Matziaris, Miguel Angel Cabrera, Duc Toan Cao, Chong Peng, for all our discussions, mutual support and every moment that we passed together during our meetings.

Further I would like to thank all my office fellows: especially Dr. Alessandro Frigo (and excellent musician) and Dr Raffaella Santagiuliana, for their kindness, their help with the Italian language and all their valuable advice and support throughout these years. Also, many thanks to Dr. Lorenzo Zanelli, for his help with the linear algebra. And of course my thoughts go to all of the colleagues at ICEA Department: Dr Mattia Pizzocaro, Dr Filippo Lorenzoni, Msc Pietro Mascheroni, Msc Claudio Gavagnin, Msc Pietro Favia, Dr Silvia Todros, Dr Paola Pachera, Msc Paolo Rizzato for the lunches at the canteen, our daily routine and the mutual support.

I wish to express also my thanks to all of my dear friends back home who have been there for me during all these years and never stopped contacting me although I was away, showing their interest and their care: Vasia, Christina, Elly, Dimis, Tatiana, J. Dikaros, Tasos, Yiannis, Mitsos 1st, Elias, George, Iro, Fanis. We made it fellows, just like the proverb says: “When the going gets tough, the tough get going”. The most special thanks go to my old flatmate from Padua and new friend Christina Glytsou who made me believe that true friendships can occur even later in life. Christina thank you for being there at every moment of effort and of joy and for being you.

Finally, my most heartfelt thanks go to my family; to my beloved parents Panos and Dina and to my indescribably great sister Maria. Without your love and unconditional support I wouldn't have made it this far. This thesis is dedicated to you.

ABSTRACT

Rainfall is one of the most common triggering factors of landslides. Due to the usual large extension of rainfall events, hydrologically-driven instability can be triggered over large areas and frequently results in a diffuse, flow type of failure which occurs abruptly, involving a shallow soil deposit of different grading and origin. Considering the destructiveness of this type of landslides, the forecast of this risk consists a fundamental issue.

This PhD thesis is primarily motivated by the need for a better understanding of the slope's mechanical response to rainfall infiltration and for a more accurate and realistic prediction of the location and time of the slope failure occurrence with regards to physical, mathematical and numerical modelling. To this end, the modelling of rainfall induced landslides is considered as a coupled variably saturated hydro-mechanical problem. For the numerical simulations the geometrically linear finite element code Comes-Geo is used, in which soils are considered as non-isothermal elasto-plastic multiphase solid porous materials.

Furthermore, this PhD manuscript is dedicated to the concept of material instability in multiphase geomaterials, with particular reference to rainfall-induced landslides. A recently proposed criterion, the second order work criterion, based on Hill's sufficient condition of stability (Hill, 1958) has been implemented on the abovementioned code. It consists in studying the sign of the second order work at the material point level and it is used for the detection of the onset of the local failure. The definition of the second order work criterion is reviewed and three different expressions are presented additionally, which could be used in the case of variably saturated porous materials; the second order work is expressed in terms of effective stress, of total stress and thirdly by taking into account the hydraulic energy contribution for the case of partially saturated soils.

The abovementioned modelling framework in conjunction with Hill's criterion is applied for the finite element analysis of three initial boundary value problems: a plane strain compression test on dense sand and isochoric granular material where strain localisation is observed; the failure initiation of a well-documented flowslide (Sarno-Quidinci event, southern Italy 1998); a large scale slope stability experimental test subjected to rainfall infiltration (University of Padua, 2014).

Keywords: Landslides; Rainfall infiltration; Multiphase porous material; Material instability; Hill's criterion; Localised mode of failure; Diffuse mode of failure.

SOMMARIO

La pioggia è una delle maggiori cause delle frane. A causa della grande estensione dei fenomeni piovosi, l'instabilità idro-geologica può verificarsi su aree estese, e spesso si trasforma in una rottura di tipo diffusa causando colate che avvengono improvvisamente, coinvolgendo strati superficiali di suolo di diversa origine e classificazione. Considerando la capacità distruttiva di questo tipo di eventi, la valutazione del rischio corrispondente è di fondamentale importanza.

Questa tesi è motivata principalmente dalla necessità di una migliore conoscenza della risposta di un pendio all'infiltrazione della pioggia e da una predizione più precisa e realistica dell'istante e del luogo del distacco di frane mediante opportuna modellazione fisico-matematica e numerica. A questo scopo, la modellazione delle frane causate dalla pioggia avviene considerando questi eventi come un problema idro-meccanico accoppiato in condizioni di saturazione variabile. Per le simulazioni numeriche è stato utilizzato il codice agli elementi finiti "Comes-Geo", in cui il materiale costituente i pendii è analizzato come un solido poroso multifase elasto-plastico in condizioni non-isoterme.

In questa tesi inoltre è discusso il problema dell'instabilità dei geomateriali multifase, con particolare applicazione alle frane indotte dalla pioggia. A tal fine, il criterio del lavoro del secondo ordine, basato sulla condizione sufficiente di stabilità di Hill (1958), è stato implementato nel codice di calcolo agli elementi finiti sopra menzionato. Esso consiste nello studio del segno del lavoro del secondo ordine a livello di punto materiale ed è utilizzato nella tesi per rilevare la rottura locale. La formulazione analitica di questo criterio è stata modificata per i solidi porosi proponendo tre diverse espressioni che possono essere utilizzate per i materiali porosi multifase in condizione di saturazione variabile; il lavoro del secondo ordine è stato espresso in funzione della tensione efficace (i), della tensione totale (ii) e considerando il contributo dell'energia idraulica nel caso di terreni parzialmente saturi (iii).

L'approccio modellistico sopra menzionato e il criterio di Hill sono stati applicati all'analisi agli elementi finiti di tre problemi di collasso di suoli: un test di compressione biassiale (in stato piano di deformazioni) di una sabbia densa e un materiale granulare isocorico, in cui è stata osservata sperimentalmente la localizzazione di deformazioni, il distacco di una frana ben documentata della zona di Sarno-Quindici (Italia meridionale, 1998), un test di stabilità di un pendio sperimentale di grande scala soggetto a pioggia (Università degli Studi di Padova, 2014).

Parole chiave: Frane, infiltrazione piovosa; materiale poroso multifase; instabilità di materiale; criterio di Hill; rottura localizzata; rottura diffusa.

Table of Contents

1	Introduction.....	1
1.1	General context of the thesis	1
1.2	Thesis objectives and contributions	3
1.3	Outline of the thesis	3
2	Stability in Geomaterials and Second order work criterion.....	5
2.1	Introduction	5
2.2	Definitions.....	5
2.3	Examples of failure modes in geomaterials	7
2.3.1	Homogeneous laboratory tests	7
2.3.2	Rainfall- induced landslides types	9
2.4	Material instability or bifurcation in geomaterials.....	10
2.4.1	Plastic limit criterion.....	10
2.4.2	Rice localisation criterion	11
2.4.3	Hill’s sufficient condition of stability	12
3	Physical processes in rainfall-induced landslides and numerical modelling methods	19
3.1	Introduction	19
3.2	Unsaturated soil mechanics.....	19
3.2.1	Matric suction in the soil.....	19
3.2.2	Soil water retention curve	22
3.2.3	Relative permeability functions for partially saturated soils.....	24
3.2.4	Effective stresses in unsaturated soils	25
3.3	Hydraulic mechanisms in rainfall–induced landslides.....	26
3.3.1	Groundwater table rise or formation of a perched water table from surface infiltration	26

3.3.2	Loss of matric suction from surface infiltration.....	26
3.3.3	Exfiltration (spring) from the bedrock	27
3.4	Transient hydraulic response of slopes to rainfall infiltration.....	27
3.5	Controlling factors for rain infiltration and pore water pressure changes in unsaturated slopes	29
3.6	Stress paths in soil slopes	31
3.7	Modelling options for the simulation of the failure onset of the rainfall-induced landslides	33
3.7.1	Limit equilibrium analysis	33
3.7.2	Finite element method analysis	35
4	Mechanics of porous media: mathematical model.....	39
4.1	Introduction	39
4.2	Averaging principles	40
4.2.1	Averaging process	41
4.2.2	Microscopic balance equations	44
4.2.3	Macroscopic balance equations.....	45
4.3	Macroscopic balance equations for a non-isothermal partially saturated porous medium.....	47
4.3.1	Kinematic equations	48
4.3.2	Mass balance equations.....	51
4.3.3	Linear momentum balance equation	55
4.3.4	Angular momentum balance equation.....	55
4.3.5	Balance of energy equation.....	56
4.3.6	Entropy inequality	56
4.4	Constitutive equations	57
4.4.1	Stress tensor in the fluid phases	58

4.4.2	Gaseous mixture of dry air and water vapour	58
4.4.3	Sorption equilibrium	59
4.4.4	Clausius-Clapeyron equation	60
4.4.5	Pore size distribution.....	61
4.4.6	Equation of state for water	61
4.4.7	Darcy's law	62
4.4.8	Fick's law.....	63
4.4.9	Stress tensor in the solid phase and total stress.....	64
4.4.10	Solid density.....	65
4.4.11	Fourier's Law.....	66
4.5	General field equations	67
4.5.1	Mass balance equation	67
4.5.2	Linear momentum balance equation	71
4.5.3	Energy balance equation	72
4.6	Physical approach: extended Biot's theory	73
4.6.1	The physical model	73
4.6.2	Constitutive equations.....	79
4.6.3	Governing equations	81
4.7	Quasi – static case	85
4.7.1	Equilibrium equation of the multiphase medium.....	85
4.7.2	Mass balance equations.....	86
4.7.3	Energy balance equation	86
4.7.4	Further developments of the model.....	87
4.8	Boundary and initial conditions	87
5	The code Comes-Geo.....	89

5.1	Introduction	89
5.2	Finite element method	90
5.2.1	Method of Weighted Residuals: discretization in space	90
5.2.2	Linearization. Discretization in time	92
5.3	Finite element library	94
5.3.1	Four node quadrilateral elements	94
5.3.2	Eight node quadrilateral elements	95
5.3.3	Nine node quadrilateral elements	95
5.4	Numerical integration.....	96
5.5	Matrix solution procedure	97
5.6	Convergence and error analysis	98
6	Numerical results and numerical investigation of the second order work criterion ..	101
6.1	Introduction	101
6.2	Finite element analysis of a globally undrained dense sand sample	102
6.3	Finite element analysis of the Sarno flowslide.....	113
6.4	Finite element analysis of an experimental slope.....	125
7	Conclusions and perspectives for future research.....	137
8	References.....	141

List of figures

Fig. 2.1 Equilibrium configuration: (a) indifferent or neutral, (b) stable, (c) unstable equilibrium condition (Lammers & Zurcher 2011).	6
Fig. 2.2 Example of localization with shear plane along a triaxial test; after J.L. Colliat-Dangus Doctoral Thesis, cited by (Desrues & Chambon 2002).....	8
Fig. 2.3 Example of liquefaction after an undrained triaxial test due to a “perturbation” after the deviatoric stress peak q (Servant et al. 2005).....	8
Fig. 2.4 Coexistence of localization pattern within a chaotic displacement field at East Gate Mudslide, Glacier National Park, Canada (Nicot & Darve 2011)	10
Fig. 2.5 Existence of a discontinuity, orientation, and normal direction (Nicot & Darve 2011).	11
Fig. 2.6 CIU stress path of saturated, loose sand (Darve et al. 2004)	12
Fig. 2.7 Arbitrary volume schematic of an unsaturated geomaterial (Buscarnera & Mihalache 2014)	16
Fig. 3.1 Schematic composition of soil	20
Fig. 3.2 Capillary tube analogy	21
Fig. 3.3 Definitions of variables associated with the soil water retention curve (Fredlund 1998)	23
Fig. 3.4 Schematic diagram of groundwater circulation and of the hydraulic interactions between bedrock and the upper soil layer ((Askarinejad 2013) modified after Johnson & Sitar 1990)	27
Fig. 3.5 Physical processes in the hydrologic cycle of natural slopes (Lu & Likos 2004)	29
Fig. 3.6 Reference schemes adopted for the shallow landslides induced by rainfall directly infiltrating the slope surface and spring from the bedrock (Cascini et al. 2010).....	32
Fig. 3.7 Slope, slices and general unknowns in conventional methods (Laouafa & Darve 2002)	34
Fig. 4.1: Typical averaging volume dv of a porous media consisting of three constituents ..	41
Fig. 4.2 Averaged value z versus size of the average volume dv	42
Fig. 4.3: Contact area between two grains in the partially saturated case	77
Fig. 5.1 Schematic division in simply regions.....	90
Fig. 5.2 Four node quadrilateral element.....	95

Fig. 5.3 Eight node quadrilateral element.....	95
Fig. 5.4 Nine node quadrilateral element.....	96
Fig. 6.1 Description of the geometry, boundary and loading conditions	103
Fig. 6.2 Numerical results after 27s of loading (values plotted at the Gauss points): a Equivalent plastic strain contour [-]; b Negative values of the second order work W_2 contour [Pa]; c Positive values of the volumetric strain contour [-]	105
Fig. 6.3 Numerical results after 27s of loading (values plotted at the nodal points): a Capillary pressure contour [Pa]; b Water degree of saturation contour [-]; c Vapor pressure contour [Pa].....	106
Fig. 6.4 Numerical results of the second order work [Pa] after 27s of loading (values plotted at the Gauss points): a in terms of total stresses W_{2tot} ; b expression for partially saturated soils W_{2unsat}	107
Fig. 6.5 a Material points location; b evolution of the W_2 (equation 2.15); c of the water saturation degree; d of the equivalent plastic strain; e of the capillary pressure; f of the volumetric strain, at these points	108
Fig. 6.6 a Comparison between the results obtained from the three different expressions of the second order work in the middle of the shear band; b evolution of the $W_{2unsat} - W_2$ difference; c evolution of the $W_{2tot} - W_2$ difference; d evolution of the $W_{2tot} - W_{2unsat}$ difference	109
Fig. 6.7 Numerical results after 0.77 s of loading using the von Mises constitutive model: a equivalent plastic strain contour [.] ; b nil and negative values of the second order work W_2 [Pa] contour; c evolution of the equivalent plastic strain and of W_2 in the middle of the shear band.....	110
Fig. 6.8 Field site plan- geometry and stratigraphy of the section A-A (Cascini et al. 2008)	113
Fig. 6.9 a Rainfall recorded at the toe of Pizzo d'Alvano massif (Cascini et al. 2003); b Rainfall loading function on the upper surface.....	115
Fig. 6.10 a Discretisation of the section A-A; b finite element discretization at the basis of the slope; c stratigraphic section of the slope at toe. The vertical line indicates the vertical boundary of the mesh at toe (figure 6.10b).....	116

Fig. 6.11 Distribution of the deviatoric stress after the equilibrium with the initial and boundary hygro-thermal conditions	117
Fig. 6.12 a Displacement contour [m]; b displacement vectors at the end of May 6 (lower part of the slope)	117
Fig. 6.13 a Equivalent plastic strain [-]; b water saturation [-] contour at the end of May 6 (lower part of the slope)	118
Fig. 6.14 a Displacement contour [m]; b displacement vectors at the end of May 5 (spring zone).....	119
Fig. 6.15 a Equivalent plastic strain [-] contour; b water saturation [-] contour; c second order work W_2 [Pa] contour at the end of May 5 (spring zone)	119
Fig. 6.16 Node location for the analysis at the lower part of the slope	120
Fig. 6.17 a Evolution of the displacements [m]; b the equivalent plastic strain [-] at the lower part of the slope.....	120
Fig. 6.18 a Evolution of the water saturation [-]; b the relative water pressure [kPa] at the lower part of the slope	121
Fig. 6.19 a Evolution of the mean stress [kPa]; b deviatoric stress [kPa] at the lower part of the slope	121
Fig. 6.20 a Second order work contour in terms of effective stresses at the beginning of May 6th (lower part of the slope); Comparison between the evolution of the second order work W_2 and the displacement rate b ; and the equivalent plastic strain c , at the material point level in the lower pumice layer at toe	122
Fig. 6.21 Second order work contour at the beginning of May 6th (lower part of the slope): a in terms total stresses, W_{2tot} ; b expression for partially saturated soils, W_{2unsat}	123
Fig. 6.22 Geometry and stratigraphy of the slope (longitudinal section) and representation of the measurement positions (Lora 2015).....	125
Fig. 6.23 Retention curves of the loose sand layer: (a) the relation of the effective saturation with the pressure head; (b) the relation of the relative conductivity with the effective saturation (Lora 2015)	129
Fig. 6.24 Description of the discretization of the slope, initial and boundary conditions	130
Fig. 6.25 Evolution of the wetting front (a) and the water table (b) , during the rainfall infiltration	131

Fig. 6.26 Comparison between computed and in-situ measured volumetric water content at the positions 5 and 6 (TDR5 and TDR6 respectively).....	132
Fig. 6.27 Displacement contours (a) and displacement vectors (b) , equivalent plastic strain (c) and second order work contours (d) , at the end of the analysis (after 1.8hr of rainfall input).....	133
Fig. 6.28 Evolution of: the capillary pressure and the mean stress (a) ; deviatoric stress (b) ; equivalent plastic strain and the second order work (c)	134
Fig. 6.29 Displacement contours (a) and displacement vectors (b) , equivalent plastic strain (c) and second order work contours (d) , at the end of the analysis (after 1.8hr of rainfall), using the Pastor-Zienkiewicz model (Pastor et al. 1990)	135
Fig. 6.30 Evolution of the capillary pressure (a) , of the volumetric strains (b) of the water saturation degree (c) of the mean (d) of the second order work (e) and of the deviatoric stress at TDR2 (node 187)	136

List of Tables

Table 1: Characteristic length l for some materials.....	43
Table 2 Type of element and order of integration.....	97
Table 3 Material parameters assumed for dense sand (Sanavia et al. 2006).....	104
Table 4 Geotechnical characterization of soil layers	114
Table 5 Soil parameters used in the computation for the DP model.....	126
Table 6 Additional soil parameters (Bahda 1997) used in the computation with the PZ model	129
Table 7 Parameters used for the Brooks & Corey retention and relative permeability curves (Brooks & Corey 1964)	130

1 Introduction

1.1 General context of the thesis

Hydrologically-driven slope instability represents a major threat to human life and property. Due to the usual large extension of rainfall events this type of slope failure can be triggered over large areas and generally involves shallow soil deposit of different grading and origin (Cascini et al. 2009). Considering the destructiveness of these landslides, the understanding and the hydro-mechanical modelling of the mechanisms occurring inside the source areas are a fundamental issue for the mitigation of the posed risk to life and facilities.

The most common approach for the numerical modelling of rainfall induced slope failure in engineering practice is to uncouple the fluid flow and slope stability problems and treat them in a sequential fashion. In this sense, a seepage analysis is performed first (assuming a rigid solid skeleton) for the calculation of the water pressure distribution, which is then followed by a limit equilibrium analysis for the slope stability problem.

However, the behaviour of a soil slope under rainfall conditions is closely related not only to the distribution of pore-water pressure but also to the stress state during infiltration. Pore-water pressure changes due to rainfall infiltration and seepage, will lead to changes in stresses and consecutively deformation of the soil. In reverse, stress changes will modify the seepage process, because soil hydraulic properties such as porosity, permeability and water storage capacity are affected by the changes in stresses. Therefore, the seepage and stress-strain analysis are considered to be strongly linked in unsaturated soils under rainfall conditions (Zhang et al. 2005).

More exact solutions to the coupled governing equations for deformation and seepage should be obtained when the soils in the slope are considered as deformable and in variably saturated conditions. For this reason, during this research work the modelling of rainfall induced landslides is considered as a coupled unsaturated hydro-mechanical problem. For the numerical simulations the geometrically linear finite element code Comes-Geo developed at the University of Padova, Italy, is used, in which soils are considered as non-isothermal elasto-plastic multiphase solid porous materials as developed in (Sanavia et al. 2006; Sanavia et al. 2008; Sanavia 2009) following the works of (Lewis & Schrefler 1998) and (Hassanizadeh & Gray 1979a; Hassanizadeh & Gray 1979b; Gawin & Schrefler 1996).

The second matter, which is addressed in this thesis, is the concept of material instability in multiphase geomaterials. As it is well known, slope failure is the ultimate outcome of instability mechanisms acting within the soil strata. These mechanisms can lead to a localized or diffuse mode of failure. In fact, these are the two main types of failure attributed to shallow rainfall induced landslides; the shear failure, meaning the formation of shear bands due to strain localization which cause soil slips and flowslide (related sometimes to static liquefaction processes), with no shear band formation resulting in flow-type failures (Eichenberger 2013).

Although the first type of failure can be described using localization theory, diffuse failure mode cannot be described either by classical empirical methods or plasticity theories (Lignon et al. 2009). Therefore, there is the need for a more generalized criterion to be used which will be able to capture the instability independently of the failure mode. To this end, the second order work criterion, based on Hill's sufficient condition of stability in elasto-plastic solids (Hill 1958), has been applied for multiphase porous elasto-plastic solids and is being examined in this research study to investigate the stability of initial boundary value problems. It consists in computing the sign of the second order work for each material point of the domain, enabling to judge the potential instability of a spatial domain in which a set of local negative values occur and giving information for the detection of the onset of the failure. The argument for that is that the second order work criterion is considered as a more generalized criterion since it has been proved mathematically that it is the first bifurcation criterion to be reached along a loading path (Laouafa & Darve 2002) with respect to failure by divergence instabilities. What has been proved to be mathematically valid is being tested also numerically hereafter, also numerically in this thesis, on different cases of multiphase finite element analyses.

1.2 Thesis objectives and contributions

The content of this thesis which is outlined in the next section contributes to the following objectives:

1. Identification of key physical processes and factors governing rainfall-induced landslides.
2. Numerical modelling of progressive failure and hydro-mechanically coupled phenomena in rainfall-induced landslides.
3. Numerical investigation of the second order work criterion when applied for the multiphase finite element analysis of initial and boundary value problems.
4. Numerical investigation and comparison between the different expressions of the second order work criterion which could be used in the case of variably saturated porous materials.
5. Numerical investigation on the use of advanced constitutive models in conjunction with second order work criterion.

1.3 Outline of the thesis

The content of this thesis is organised as follows:

In **Chapter 2**, which constitutes a review on the description of instability and failure in geomaterials, the definitions of these two concepts are proposed as well as that of the bifurcation, in a general context. Some representative examples of failure modes are described then, both for the case of experimental tests and for large-scale problems with particular reference to rainfall-induced landslides. Finally, the main criteria for the study of geomaterials stability are presented with extended reference to the second order criterion which has been proved mathematically to be a more generalised criterion.

Chapter 3, provides an overview of the physical processes and the governing factors of the failure mechanisms in non-cohesive soil slopes subjected to rainfall. Furthermore, a review is presented of the existing numerical methods for the study of slope stability problems. Based on the review of the physical processes, a suitable modelling approach is chosen for the numerical simulations performed in chapter 6.

In **Chapters 4 and 5**, the mathematical and numerical model is presented, which is selected for the coupled thermo-hydro-mechanical processes taking place in partially saturated

deforming porous media. Firstly, the governing equations of the T-H-M model following (Lewis & Schrefler 1998), are presented. Subsequently, the description of the discretization in space and in time domain of the governing equations follows and of the F.E.M. modelling approach used for the solution of the initial boundary problem.

In **Chapter 6**, the numerical results of the multiphase analyses of three initial and boundary value problems are presented and discussed. In particular it concerns the analyses of a plane strain compression test on dense sand and isochoric grain matter where strain localisation is observed and the failure initiation of a well-documented flowslide (Sarno-Quidici events, southern Italy 1998); in both abovementioned analyses the different expressions of the second order work criterion are employed and investigated. Finally, a large scale slope stability experimental test subjected to rainfall infiltration (University of Padova, 2014) is simulated with a classic and an advanced constitutive model in conjunction with the second order work criterion.

Chapter 7 provides general conclusions and summarises the principal achievements of this thesis. Furthermore, perspectives for future research are highlighted.

2 Stability in Geomaterials and Second order work criterion

2.1 Introduction

Landslides or questions related to slope stability are usually considered in the framework of plastic limit analyses. Recent progress has made it possible to describe some failure modes in the framework of the theories of bifurcation of the strain mode by plastic strain localization and the shear-banding phenomenon (Darve & Laouafa 2000). In this context, the definitions of instability, bifurcation and their relation to failure of geomaterials are provided in this chapter. Furthermore, a brief description of the major failure modes which prevail in geomaterials is given, as observed in the laboratory as well as in-situ in the case of shallow rainfall-induced landslides. Finally, the question of stability analysis is reconsidered by taking into account three different instability criterions with an extended reference to the second order work criterion which is being investigated throughout this thesis.

2.2 Definitions

In the context of geomechanics there are three main concepts that are widely met: failure, instability and bifurcation (or loss of uniqueness). Hereafter an attempt is made to clarify their meanings and their definitions.

The notion of failure

By definition, a system is said to be in a state of failure (or collapse) when a small increase in load results in **high deformation rate** and a **loss of load capacity** in a very short time. According to (Daouadji et al. 2011) failure appears as a phenomenon associated with the

existence of some limit stress states which cannot be passed by the material for any possible monotonous loading path. At such a limit stress state if an additional load is imposed, the state of the material changes suddenly with the occurrence of large deformations, cracks, fragmentation, etc. Indeed it becomes impossible to apply this additional load. This brutal change is called roughly ‘failure’.

The notion of instability

In physics stability is defined in the following way: it is the property of a system in which any departure from an equilibrium state gives rise to forces or influences which tend to return the system to equilibrium. This is also known as static stability.

Figure **Fig. 2.1** shows three different configurations of stability: In the stable configuration, a ball always rolls toward the equilibrium point at the bottom of the valley. In the indifferent or neutral configuration, the ball can roll anywhere and remain equally stable or unstable. In the unstable equilibrium condition, the ball is stable only if it remains perfectly balanced at the top of the hill.

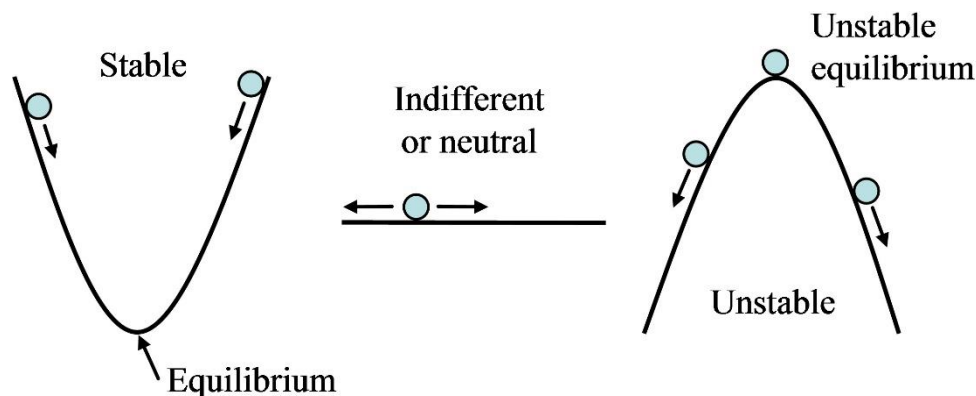


Fig. 2.1 Equilibrium configuration: (a) indifferent or neutral, (b) stable, (c) unstable equilibrium condition (Lammers & Zurcher 2011).

Conversely, a commonly admitted definition of instability is the following: a system is reputed unstable, if and only if **an infinitesimal perturbation induces finite changes** in the state of a system; which corresponds to the Lyapunov (Lyapunov 1907) definition of stability, adapted in the field of interest (solid mechanics and geomechanics) by the following statement: a small variation in any loading parameter or in any variable characterizing the mechanical state of the geomaterial will induce only a small variation of the response variables.

The notion of bifurcation (or loss of uniqueness)

According to (Nicot & Darve 2011) bifurcation is a widely used notion in physics: the first intuitive definition establishes the existence of **more than one response path** from a given state for the same loading path (Leger & Potier-Ferry 1993; Nguyen 1987). The system may follow different bifurcated branches, departing from the fundamental response path. Another definition can also be given: a bifurcation is the sudden change in the nature of the response of the system under continuous evolution of the internal variables (or loading parameters). According to (Nicot & Darve 2011) this definition is particularly relevant, as it relates the notions of both bifurcation and failure. Indeed, failure can be regarded as a state from which a transition from a quasistatic regime to a dynamical regime is possible under certain constant loading parameters.

Overall, the failure of materials is certainly complex, but is inarguably related to material instability and a loss of uniqueness problem, although the converse may not be true (Daouadji et al. 2011; Laouafa et al. 2011). In fact, taking into account the above definitions, failure can manifest itself as a sudden transition from a static regime to a dynamic one with an exponential growth of strains and for this it can be seen as a bifurcation phenomenon. Furthermore, as a property of bifurcated states, the attending failure will depend on perturbations and imperfections in the system. Because of this dependence on small perturbations, failure can also be viewed as an instability phenomenon in the basic Lyapunov sense (Lyapunov 1907). Indeed, for a given bifurcation state on the stress–strain curve, any additional and vanishingly small loading will lead to infinitely large responses (Daouadji et al. 2011).

2.3 Examples of failure modes in geomaterials

The two material failure modes that are of basic interest when considering geomaterials are: the localized and the diffuse mode of failure. These two modes of failure are widely met in the laboratory while carrying out conventional laboratory tests as well as in-situ (e.x. landslides).

2.3.1 Homogeneous laboratory tests

The most conventional laboratory tests to model the material behaviour of soil samples assumed to be homogeneous, up to failure are the triaxial tests. The localised failure mode can

be seen through a triaxial test performed on a dense sand for example, where the deviatoric stress (q) – axial strain (ϵ_1) curve presents a peak. At this peak, there has been transition from a homogeneous strain pattern to a discontinuous one, characterized by the appearance of a system of bands in which strains concentrate and shear bands develop (Nicot & Darve 2011), as illustrated in Figure **Fig. 2.2**.



Fig. 2.2 Example of localization with shear plane along a triaxial test; after J.L. Colliat-Dangus Doctoral Thesis, cited by (Desrues & Chambon 2002)



Fig. 2.3 Example of liquefaction after an undrained triaxial test due to a “perturbation” after the deviatoric stress peak q (Servant et al. 2005)

On the other hand, the diffuse failure mode is characterised by a sudden collapse and corresponds to a more homogeneous occurrence of failure without any substantial occurrence

of cracking or localised deformation. The case of (static) liquefaction is considered a type of a diffuse failure mode. The undrained triaxial test performed on (very) loose sand allows to highlight this mode of failure. If the test is strain-controlled it is possible to be continued until the loss of the effective stresses (without a significant acceleration of the deformations). If the test is stress-controlled (i.e. the axial force is controlled) the sample collapses abruptly at the peak deviatoric stress but always with no evidence of localisation occurrence (Khoa 2005; Darve et al. 2007). Such an example of collapse is presented in Figure **Fig. 2.3**.

2.3.2 Rainfall- induced landslides types

At large scales, the localised and the diffused failure mode are the two main mechanisms that also seem to prevail for shallow rainfall-induced landslides which are mainly studied in this thesis. The three main types of shallow rainfall-induced landslides that are widely met in practice are: the soil slips (or slides), slides turning into flow and the flowslides.

Flow-type landslides are most often attributed to the mechanism of static liquefaction. Static liquefaction occurs in saturated or initially slightly unsaturated, collapsible soils submitted to undrained or drained loading conditions leading to an unstable stress state, in which large strains and excess pore pressures develop simultaneously while the shear strength of the soil decreases (Lade & Pradel 1990; Lade 1993). In this case slope failure occurs abruptly with rapid post-failure acceleration (Iverson 2000).

Slides or soil slips are mainly attributed to shear failure and localised strain softening in slopes, caused by inhomogeneous suction reductions and stress states could then lead to a **progressive** global slope failure (Eichenberger 2013). In this case soil slopes can respond slowly to rainfall and move at very low speeds (Swanson & Swanston 1977).

Slide-to-flow is the case where both failure modes coexist (**Fig. 2.4**). It is the case when localised failures occurred due to restricted seepage, which can lead to global shear failure and a subsequent flow-type post failure stage, (e.g. (Take et al. 2004), (Lee et al. 2008)). As mentioned also in (Cascini et al. 2010) slide –to –flow failure comes as a result of complex mechanisms characterised by a decreasing in the shear strength due to local hydraulic conditions. At the adjacent zones the shear stresses increase due to unbalanced driving forces both in loose and dense soil and further slides occur. The latter is characterised by a high initial acceleration that can consequently turn into a flow.



Fig. 2.4 Coexistence of localization pattern within a chaotic displacement field at East Gate Mudslide, Glacier National Park, Canada (Nicot & Darve 2011)

2.4 Material instability or bifurcation in geomaterials

In this thesis, we are interested only in instabilities which may arise from specific characteristics of the material behaviour. Instabilities which are related to geometric effects, (e.x. beam buckling) or to dynamic effects (effects of mass and inertia) are not addressed in this thesis. In this section we present a summary of the major criterions used for the analysis of the material stability.

2.4.1 Plastic limit criterion

The problems of stability analysis have been generally studied using a plasticity criterion with the assumption of a flow rule for the behaviour of the material.

Let us recall within the elasto-plasticity theory context, the general constitutive expression linking the stress increments $d\sigma$ and the strain increments $d\epsilon$:

$$d\sigma = \mathbf{M} : d\epsilon \quad (2.1)$$

where \mathbf{M} is the fourth order tangent constitutive tensor.

From a theoretical point of view, the notion of failure corresponds to the existence of limit states. In the classical views a limit stress state is reached asymptotically and it is not possible to go through this stress state. If so, a limit stress state will be characterised in elasto-plasticity by an undefined deformation for a nil incremental stress:

$$d\boldsymbol{\sigma} = 0 \text{ and } \|d\boldsymbol{\varepsilon}\| \text{ undefined} \quad (2.2)$$

Conditions (2.2) imply for incrementally linear constitutive relations:

$$\det \mathbf{M} = 0 \quad (2.3)$$

where the above condition corresponds to the ‘limit plastic condition’ or loss of uniqueness of the solution (i.e. defines a limit surface in the six-dimensional stress space).

$$\mathbf{M} : d\boldsymbol{\varepsilon} = 0 \quad (2.4)$$

The last condition is related to the flow rule, i.e. this equation gives the direction of $d\boldsymbol{\varepsilon}$ (but not its norm) when the plasticity criterion is reached.

2.4.2 Rice localisation criterion

However, the experiments have shown that some failure modes with localization patterns (shear banding phenomenon or compaction–dilatation band formation) do not fulfil the plasticity criterion (Daouadji et al. 2011). This localised failure mode which is characterised by a shear band formation, due to strain localization has been well described by Rice (Rice 1976) taking into account the continuity of the stress vector through the band and the kinematics of the shear band and establishing a proper localization criterion.

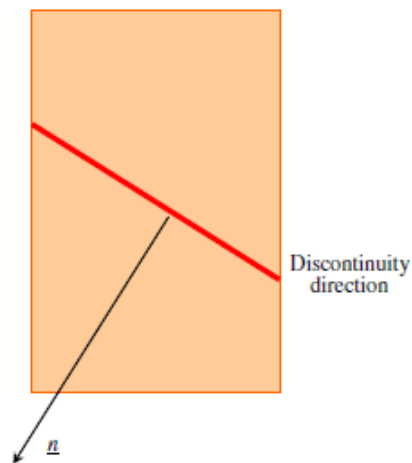


Fig. 2.5 Existence of a discontinuity, orientation, and normal direction (Nicot & Darve 2011).

The Rice criterion corresponds to the vanishing of the determinant of the acoustic tensor:

$$\det ({}^t \mathbf{n} \mathbf{M} \mathbf{n}) = 0 \quad (2.5)$$

where vector n indicates the normal to the discontinuity direction (**Fig. 2.5**).

2.4.3 Hill's sufficient condition of stability

It has been shown that material instabilities can lead to diffuse modes of failure inside the plastic limit condition, which are characterized by the lack of localization patterns and for this reason cannot be detected neither by a plastic limit criterion nor by a localization criterion (Darve et al. 2004; Nicot et al. 2011). A characteristic example of this kind of failure can be illustrated through an undrained triaxial test on loose sand. If a small additional force is applied at the stress peak value, a sudden failure occurs with no localisation pattern strictly inside the Mohr-Coulomb plastic limit condition (**Fig. 2.6**).

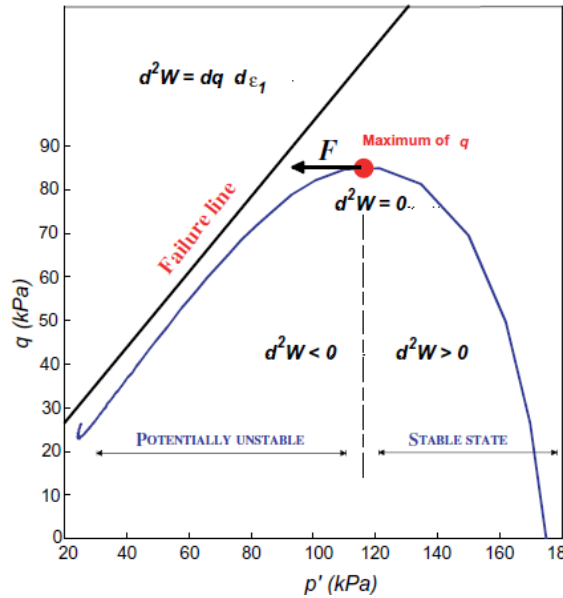


Fig. 2.6 CIU stress path of saturated, loose sand (Darve et al. 2004)

In 1958, Hill (Hill 1958) proposed the following sufficient condition of stability for an elastoplastic body:

$$\int_V \delta s \, d\left(\frac{\partial \mathbf{u}}{\partial \mathbf{x}}\right) dV > 0 \quad \forall \left\| d\left(\frac{\partial \mathbf{u}}{\partial \mathbf{x}}\right) \right\| \neq 0 \quad (2.6)$$

where V is the volume of the body at time t , s the component of the nominal stress tensor (the transpose of the first Piola–Kirchhoff tensor), and $d(\partial \mathbf{u} / \partial \mathbf{x})$ the gradient velocity. In the

case of a small strain assumption and by neglecting geometrical effects, the condition (2.6) reads:

$$\int_V d\boldsymbol{\sigma} : d\boldsymbol{\varepsilon} dV > 0 \quad \forall \|d\boldsymbol{\varepsilon}\| \neq 0 \quad (2.7)$$

with $d\boldsymbol{\sigma}$ the incremental Cauchy stress tensor, and $d\boldsymbol{\varepsilon}$ the incremental strain tensor.

At the material point level Hill's condition of stability is expressed through the second order work criterion as follows: a mechanical stress–strain state is considered as stable if, for any couple $(d\boldsymbol{\sigma}, d\boldsymbol{\varepsilon})$ linked by the rate-independent constitutive relation the second order work W_2 is strictly positive:

$$\forall d\boldsymbol{\varepsilon} \in \mathbb{R}^{2n} \setminus \{0\} \text{ with } d\boldsymbol{\varepsilon} = \mathbf{M} : d\boldsymbol{\sigma}, W_2 = d\boldsymbol{\sigma} : d\boldsymbol{\varepsilon} > 0 \quad (2.8)$$

where n is the dimension of the stress (or strain) space and \mathbf{M} is the tangent constitutive tensor.

Different interpretations of this criterion have been provided by considerable amount of studies with the aim to give to it an additional physical meaning. These studies have led to the notions of controllability and sustainability.

The **controllability** notion which was introduced by Nova (Nova 1994), related Hill's criterion with the boundary and loading conditions (control conditions) imposed to a porous solid. It was developed by examining the conditions in which a prescribed loading program involving specific loading parameters (also referred to as control parameters) can be applied to a system, from a given mechanical state after a given loading history. If the considered loading program can be applied, then this program is said to be controllable. Following the definition given by Nova (Nova 1994), starting from a given mechanical state, a loading program can be applied if and only if at each step it produces a unique incremental response to the incremental loading governed by the control parameters. Finally, loss of controllability of a certain loading path can be described as loss of uniqueness of the incremental solution and has been investigated in a number of studies (see for instance (Vardoulakis et al. 1978; Vardoulakis & Sulem 1995; Petryk 1993; Darve et al. 1995; Bigoni & Hueckel 1991; Chambon & Caillerie 1999)).

The notion of **loss of sustainability** was introduced by Nicot (Nicot & Darve 2007; Nicot et al. 2007) and relates the second order work criterion with the transition from a stationary regime to a dynamic one, without any external input and accompanied with a burst of kinetic

energy. In more detail, Nicot (Nicot & Darve 2007) showed the link between the violation of condition (2.6) and an increase of the kinetic energy of the medium from a zero value; a system made up of a volume V of a given material, in equilibrium at time t under a prescribed external loading, is considered. The instantaneous evolution of the system, in equilibrium configuration C at time t , is governed by the following equation that includes dynamical effects:

$$\delta E_C(t) = \int_{\Gamma} \boldsymbol{\sigma} \cdot \mathbf{n} \delta \mathbf{u} dS - \int_V \boldsymbol{\sigma} \frac{\partial(\delta \mathbf{u})}{\partial \mathbf{x}} dV > 0 \quad (2.9)$$

where E_C represents the system's current change in kinetic energy related to the incremental displacement field $\delta \mathbf{u}$. $\boldsymbol{\sigma}$ is the Cauchy stress tensor and \mathbf{n} is the current normal to the boundary (Γ) at the point considered.

Differentiating the above equation leads to the following relation according to (Nicot & Darve 2007; Nicot et al. 2007; Nicot & Darve 2011) :

$$2E_C(t + \delta t) = B_2 - W_2 \quad (2.10)$$

where B_2 is a second-order boundary term involving loading parameters (parameters defining how the loading is applied on the boundary of the system) and $W_2 = \int_V \delta \boldsymbol{\sigma} \delta \boldsymbol{\varepsilon} dV > 0$ denotes the second-order work of the system, associated with the incremental evolution $(\delta \boldsymbol{\sigma}, \delta \boldsymbol{\varepsilon})$. This expression of the second-order work assumes that geometrical changes can be omitted over the incremental evolution considered. If this assumption does not hold, a Lagrangian formulation must be adopted to express the second-order work, replacing the Cauchy stress tensor with the Piola–Kirchhoff stress tensor (Nicot & Darve 2007; Nicot et al. 2007).

In the case of constant control parameters, the term B_2 vanishes and Equation (2.10) finally reads as:

$$2E_C(t + \delta t) = -W_2 \quad (2.11)$$

Consequently, when Hill's condition is violated, the kinetic energy of the system can evolve with a second-order rate with respect to time (Prunier et al. 2016) representing the bifurcation in the response of the system from a quasi-static to a dynamic regime. Hence the notion of loss of sustainability links the notions of both bifurcation and failure as indeed failure can be

regarded as a state from which a transition from a quasistatic regime to a dynamical regime is possible even under certain constant loading parameters (Nicot & Darve 2011).

Based on the above concepts, the vanishing of the second order work indicates potential instability.

As it is proved below the second order work criterion coincides with the vanishing of the determinant of the symmetric part of the constitutive tensor as:

$$W_2 = {}^t d\boldsymbol{\varepsilon} : d\boldsymbol{\sigma} = {}^t d\boldsymbol{\varepsilon} : \boldsymbol{M} : d\boldsymbol{\varepsilon} = {}^t d\boldsymbol{\varepsilon} : \boldsymbol{M}^s : d\boldsymbol{\varepsilon} \quad (2.12)$$

$$\text{with } \boldsymbol{M}^s = \frac{1}{2}(\boldsymbol{M} + {}^t \boldsymbol{M}) \quad (2.13)$$

Thus, for incrementally linear constitutive relations and eigenvalues varying in a continuous manner from the virgin state during the loading process, condition (2.8) is equivalent to:

$$\det \boldsymbol{M}^s = 0 \quad (2.14)$$

For associated materials (the flow rule coincides with the yield surface), the constitutive matrix \boldsymbol{M} is symmetric. Thus the unstable states will coincide with the plastic limit states. In the case of non-associated materials, the second order work becomes zero (which first vanishes together with the symmetric part of the stiffness tensor \boldsymbol{M}) before the vanishing of the determinant of the tensor itself (because of the non-symmetry of the tensor) and of the determinant of the acoustic tensor (Lignon et al. 2009; Laouafa & Darve 2002; Daouadji et al. 2011). Hence, it can be stated that it is the first bifurcation criterion reached along a loading path and for this reason is considered as a more generalized criterion.

There is still an open question regarding the type of stress that should be used in equation (2.8) when studying the stability of a multiphase porous body. There is the debate on using effective or total stress; furthermore, in the case of a partially saturated medium, the hydraulic contribution for the stability of the porous body can be raised. In fact, the stability of a material specimen is related to the skeleton stability. The specimen collapses if the skeleton collapses. However, the skeleton stability depends on the pore pressures applied to the particles. The fluid phases are therefore involved in the specimen stability, similarly to the so-called weak phases, surrounding force chains, which actively participate to the strength of a dry granular specimen

(Sibille et al. 2015). Thus, three different expressions are presented hereafter for the second order work, which could be used in the case of variably saturated porous materials.

Firstly, it is written in terms of effective stress, where $\boldsymbol{\sigma}'(\mathbf{x}, t)$ is the generalized Cauchy effective stress, as it seems to be the most natural choice when modelling variably saturated geomaterials:

$$W_2 = d\boldsymbol{\sigma}' : d\boldsymbol{\varepsilon} \quad (2.15)$$

Subsequently, the second order work is expressed in terms of total stresses:

$$W_{2_{tot}} = d\boldsymbol{\sigma} : d\boldsymbol{\varepsilon} = d(\boldsymbol{\sigma}' - [p^g - S_w p^c] \mathbf{1}) : d\boldsymbol{\varepsilon} = W_2 + d(S_w p^c) d\varepsilon_v - dp^g d\varepsilon_v \quad (2.16)$$

as the total energy of a porous system, from which the second order work criterion is derived, involves total stress. Turning back to the physical origin of the second-order work, stemming from an energy conservation equation that embeds force balance, the total stress stands as the natural stress candidate. It is worth noting that in the previous equation, the total stress has also been written in terms of generalized effective stress (Schrefler 1984).

Finally, the extended expression of the second order work for the case of a partially saturated medium is presented, as it was proposed by (Buscarnera & Prisco 2012).

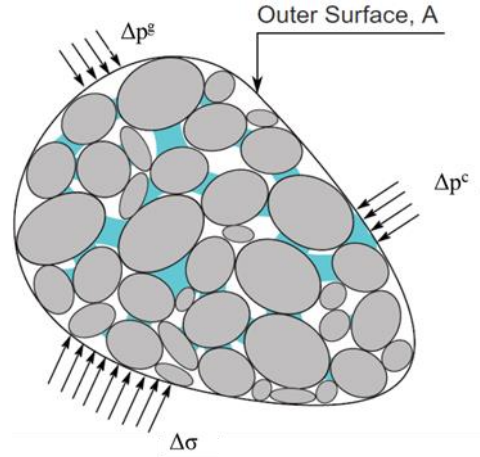


Fig. 2.7 Arbitrary volume schematic of an unsaturated geomaterial (Buscarnera & Mihalache 2014)

Starting from the re-definition of the second order work energy input to the material which involves the identification of the perturbations acting at the boundary of an arbitrary volume of unsaturated soil (**Fig. 2.7**) it concludes to the following expression:

$$W_{2_{unsat}} = d\boldsymbol{\sigma}' : d\boldsymbol{\varepsilon} - ndp^c dS_w = W_2 - ndp^c dS_w \quad (2.17)$$

where $p^c = p^g - p^w$ is the capillary pressure, with p^g the gas pressure and p^w the liquid water pressure, n is the porosity of the material and S_w the liquid water degree of saturation.

The expression (2.17) indicates that the second-order work input in a partially saturated medium depends simultaneously on two components: a first one that is mechanical in nature (i.e., it is directly associated with the skeletal deformations) and a second one that depends exclusively on the evolution of the hydraulic state (Buscarnera & Mihalache 2014).

3 Physical processes in rainfall-induced landslides and numerical modelling methods

3.1 Introduction

In this chapter, after the description of the fundamental aspects concerning partially saturated soils, an overview of the current state of knowledge on the physical processes and the failure mechanisms which take place in partially saturated slopes subjected to rainfall infiltration is presented. Subsequently, the governing factors which are necessary to be taken into account along with the main existing modelling options for the study of the phenomenon are presented.

3.2 Unsaturated soil mechanics

Partial saturation plays an important role for the hydraulic and mechanical behaviour of steep soil slopes subjected to rain infiltration. To this end, in this section the basic notions related to unsaturated soil mechanics are discussed. A more extensive description of the porous media mechanics which includes also the case of partially saturated soils, is given in the 4th chapter.

3.2.1 Matric suction in the soil

The term “unsaturated” or “partially saturated” soils refers to the soils where the pore space is simultaneously occupied by two fluid phases: the liquid and the gas phase (Figure **Fig. 3.1**), in contrast with the saturated soils where the pore space consists only of the liquid phase and behave in the same way as the dry soils where the effective stress concept is introduced by (Terzaghi 1936).

The voids of the soil skeleton are filled partly with water and partly with moist air (mixture of dry air and water vapour), which is referred to as gas. The degree of water saturation S_w is given as the ratio between the pore space occupied by the water V_w and the total pore volume V_v :

$$S_w = \frac{V_w}{V_v} \quad (3.1)$$

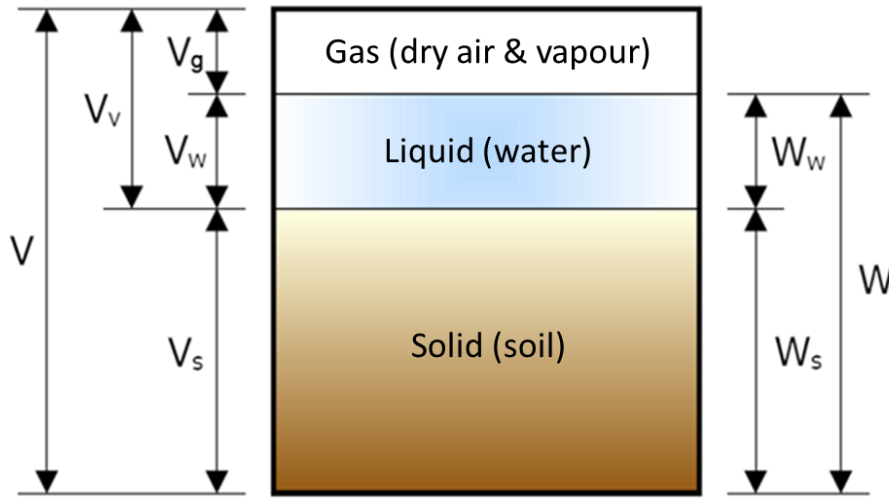


Fig. 3.1 Schematic composition of soil

The water and gas phase form interphases of negligible thickness (Fredlund & Rahardjo 1993), which possess their own physical properties and tensile stress states originating from the surface free energy of the bulk fluid. These interphases curve to form capillary menisci when in contact with solid grains. The curvature of an interphase, which leads to a contact angle $\theta_{\text{cont}} < 90^\circ$ between soil grains and water, is a result of an excess of adhesive forces between the solid and the wetting fluid (water) over cohesive forces in the wetting fluid (Tarantino 2010).

This is well demonstrated through the capillary tube analogy (Figure Fig. 3.2): when a tube of capillary size is dipped in a larger container filled with water, the water in the capillary tube rises above the water level in the container to a height that depends on capillary size. Although strictly speaking, the water still finds its level, it does so in such a way as to maintain an overall minimum surface energy. In this situation, the adhesion force allows water to rise up in the

capillary tube while gravity acts in the opposite direction. The water rises until there is a balance between these two opposing forces.

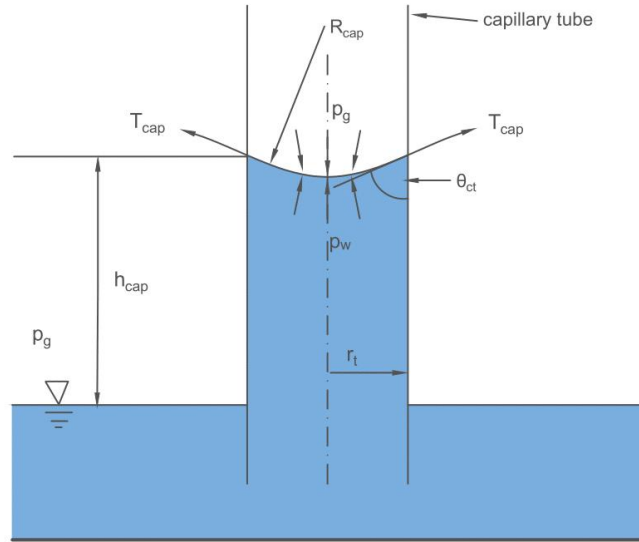


Fig. 3.2 Capillary tube analogy

The differential force between adhesion and gravity is the capillary force. This force per unit area is the capillary pressure. The vertical force equilibrium of the capillary meniscus shown in **Fig. 3.2** is written as:

$$\rho_w g h_{cap} = p^g - p^w = \frac{2T_{cap}}{R_{cap}} \quad (3.2)$$

where $\rho_w g$ is the specific weight of water, h_{cap} is the capillary height, T_{cap} the surface tension and $R_{cap} = \frac{r_t}{\cos \theta_{ct}}$ the radius of curvature of the capillary meniscus.

In analogy to the capillary tube model, the difference between pore gas and pore water pressure is termed capillary pressure:

$$p^c = p^g - p^w \quad (3.3)$$

As far as non-cohesive soils are concerned, the micromechanical mechanism which governs their macroscale response is the generation and vanishing of capillary menisci during saturation and desaturation. However, in the case of clayey soils, the dominant mechanism for the generation of negative pore water pressures at relatively low values of water content is the short range water adsorption effects (Lu & Likos 2004). Both, capillary and osmotic adsorption

mechanisms are generated by the solid matrix. Due to their common origin, the suctions generated by capillary pressure and water adsorption are grouped together to define the matric suction:

$$s = p^c - s_{ads} \quad (3.4)$$

For the higher ranges of degree of saturation considered in rainfall-induced landslides ($S_w > 0.5$) and non-cohesive soil types, matric suction is assumed to be governed by the capillary component, while short-range adsorption effects become negligible.

3.2.2 Soil water retention curve

According to (Fredlund 1998), the soil water characteristic curve is a relationship between the amount of water in the soil and soil suction. The amount of water in the soil is generally quantified in terms of volumetric water content, θ , but is sometimes represented in terms of gravimetric water content, w , or degree of saturation S_w . Total suction, ψ , is composed for both matric, s and osmotic suction, π . It is primarily the matric suction component that is of interest with regard to the engineering behavior of unsaturated soils. Laboratory data have indicated that a change in total suction is essentially equivalent to a change in the matric suction for many unsaturated soil situations. The high suction range of the soil-water characteristic curve is required primarily when studying evaporative processes near the ground surface.

The water retention curve is characterized by a main wetting and a main drying curve, which delineate the domain of possible attainable states and along which the retention behavior is irreversible (Wheeler et al. 2003). Along a drying path, the degree of saturation held in a soil is higher than along a wetting path for the same level of matric suction.

Typical features of the drying and wetting portions of the soil-water characteristic curves are defined in **Fig. 3.3**.

In the “boundary effect stage” almost all the soil pores are filled with water. The air-entry value of the soil identifies the pressure at which air enters the largest pores of the soil and is sometimes referred to as “bubbling” pressure. The coefficient of the permeability up to the air-entry value is equal to the saturated coefficient of permeability, k_s . Flow, takes place through the voids in manner similar to that of the saturated soil.

The soil starts to desaturate in the “transition stage”. The flow of water is in the liquid phase as suction increases. The soil desaturates significantly during this stage and a dramatic change in unsaturated soil properties takes place. The water content in the soil reduces significantly with increasing suction. As soil suction increases, flow occurs through increasingly smaller size pores. The connectivity of the voids or pores continues to reduce with increased values of suction and, as a result,

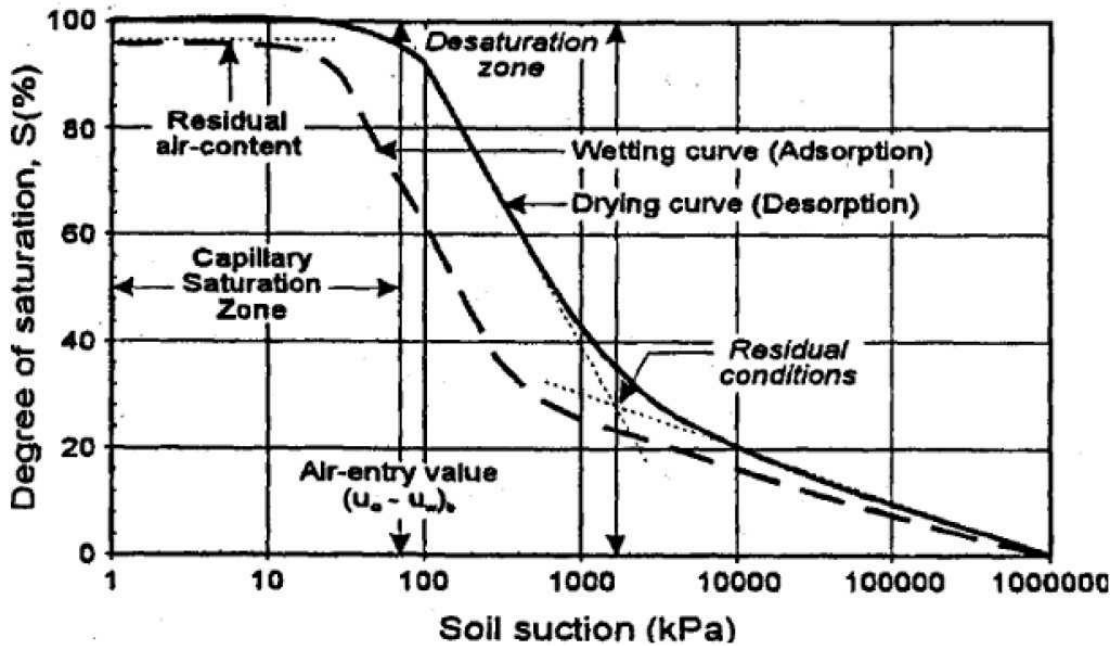


Fig. 3.3 Definitions of variables associated with the soil water retention curve (Fredlund 1998)

the unsaturated coefficient of permeability reduces with increased values of suction and due to this, the unsaturated coefficient of permeability reduces by several orders of magnitude. Also, the wetted area reduces as desaturation continues. The contribution of suction to the increase in shear strength decreases with desaturation during this stage. As a result, there is a non-linear variation in the shear strength of the soil with respect to soil suction beyond the air-entry value of the soil.

Large increases in suction eventually lead to a relatively small change in water content (or degree of saturation). This stage is referred as the “residual stage of desaturation”. There appears to be a fraction of the “relatively immobile” water in the pores of the soil at this stage, and there is little or no flow through the pores. The water content of the soil at the commencement of this stage is generally referred to as the “residual water content”. The wetted contact area has reduced significantly, and changes in soil suction may not significantly

contribute towards an increase in the shear strength of the soil. The various stages along the soil-water characteristic curve provide a physical model for understanding the unsaturated soil property functions. Both the coefficient of permeability and the shear strength behaviour of an unsaturated soil have a close relationship to the soil-water characteristic curve.

3.2.3 Relative permeability functions for partially saturated soils

Darcy's law remains applicable to describe the flow through partially saturated soils, generalized to allow for relative permeability to be taken into account. The relative permeability $k^{r\pi}$ (where $\pi = w, g$ accounting for water or gas) is a dimensionless parameter varying from zero to one.

The relations $k^{r\pi}(S_w)$ are either predicted by models based on some more or less realistic capillary assumption or experimentally determined in laboratory as well as field conditions. For typical curves of relative permeabilities to water and also air the reader is referred to Corey (Corey 1957).

The relative permeability goes to zero before the saturation reaches the value zero. The water saturation at which the relative permeability goes to zero is termed the residual water saturation or displacement residual water saturation.

Relationships used in the following are e.g. those by Brooks and Corey (Brooks & Corey 1966):

$$k^{rw} = S_e^{\frac{(2+3\lambda)}{\lambda}} \quad (3.5)$$

$$p^c = \frac{P^b}{S_e^{\frac{1}{\lambda}}} \quad (3.6)$$

where $S_e = \frac{S_w - S_{wc}}{1 - S_{wc}}$ is the effective saturation, S_{wc} is the irreducible saturation, λ the pore size distribution index, p^b the bubbling pressure (air-entry value).

3.2.4 Effective stresses in unsaturated soils

The main question when modelling the partially saturated soil behaviour concerns the appropriate combination of the stress state variables, which are the external mechanical stress σ , the pore-water pressure p^w and the gas pressure, p^g (or air pressure p^{ga} if we take into account only dry air neglecting vapour pressure). Two out of the three independent stress state variables are necessary and sufficient for the definition of the stress state of an unsaturated soil (Fredlund & Morgenstern 1977).

The two common approaches used for hydro-mechanical constitutive modelling are the independent stress variable approach and the effective stress approach. In the first case, the volumetric and strength behaviour of partially saturated soils is analysed by using the sum of two independent contributions, the applied net stress $\sigma_{net} = \sigma - p^{ga}$ and the matric suction s (e.g. (Alonso et al. 1990)). While in the second case (effective stress approach), soil deformation is directly related to effective stress σ' , which is expressed as a function of matric suction. In this work the effective stress approach is used as it offers several advantages from a modelling point of view which are mentioned later on.

Following Terzaghi's principle of effective stress (Terzaghi 1936), Bishop (Bishop 1959) proposed an effective stress for partially saturated soils combining total stress σ , pore (dry) air pressure p^{ga} and pore water pressure p^w in a single expression:

$$\sigma' = \sigma - p^{ga} \mathbf{I} + \chi (p^{ga} - p^w) \mathbf{I} = \sigma_{net} + \chi s \mathbf{I} \quad (3.7)$$

where σ is the total stress tensor, \mathbf{I} is the identity tensor and χ is Bishop's parameter, which varies between 0 for dry soil and 1 for saturated soil. Different mathematical formulations have been proposed for Bishop's parameter, either as a function of suction alone or suction and degree of saturation, as extensively reviewed in (Nuth & Laloui 2008). According to (Schrefler 1984) a straightforward assumption is to replace χ by the degree of saturation S_w :

$$\sigma' = \sigma - p^{ga} \mathbf{I} + S_w (p^{ga} - p^w) \mathbf{I} = \sigma_{net} + S_w s \mathbf{I} \quad (3.8)$$

The use of Schrefler's effective stress in the hydromechanical constitutive framework presented in Eq. (3.8) has the following implications for geomechanical modelling of unsaturated soils (Nuth & Laloui 2008):

- 1) The ability to shift from unsaturated to saturated states as Terzaghi's effective stress is recovered for $S_w = 1$;
- 2) The inclusion of hydraulic couplings in the stresses and in the case where the soil water retention curve model is hysteretic, inclusion of hydraulic hysteresis effects on mechanical behaviour since matric suction and degree of saturation appear in the effective stress definition;
- 3) Under the hypothesis of a unique critical state line for partially saturated soils using Schrefler's effective stress, unsaturated residual shear strength is reproduced even by a constitutive model for saturated soils.

The above three points constitute major advantages of the effective stress approach over the independent stress variable approach. A more thorough analysis on the effective stress approach is detailed in section 4.6 .

3.3 Hydraulic mechanisms in rainfall-induced landslides

Rainfall-induced landslides generally occur as a result of pore water pressure changes and seepage forces for which the main following hydraulic mechanisms can be responsible:

3.3.1 Groundwater table rise or formation of a perched water table from surface infiltration

This mechanism is favoured in slopes with stratified soil layers and with permeability contrasts. For example, shallow slips can take place in steep slopes with shallow soil deposits overlaying a more consistent, less permeable bedrock. The latter is mainly responsible for the build-up of the pore water pressures which will lead to the reduction of the effective stresses and of the shear strength as well as to the formation of a perched water table exerting downhill seepage forces to the soil mass (Johnson & Sitar 1990). The failure mechanism associated with the formation of a seepage layer or a groundwater table rise is often referred to as "bottom-up" mechanism (Springman et al. 2012).

3.3.2 Loss of matric suction from surface infiltration

Loss of matric suction plays one of the most important triggering mechanisms of rainfall-induced landslides. Especially in the case of steep slopes, for example, and even more for steep slopes of sandy or silty soils, safety factors may yield well below unity if the contribution of matric suction is not taken into consideration. Loss of matric suction in a slope subjected to

infiltration, is referred to as the “top-down” saturation mechanism after (Springman et al. 2012).

3.3.3 Exfiltration (spring) from the bedrock

A fractured bedrock can act as a source and deliver water to the overlying soil causing a pore-pressures build-up at the interface between the soil and the bedrock. This process is known as exfiltration and is schematically illustrated in **Fig. 3.4**. The role played by bedrock groundwater flow in the triggering of landslides has been highlighted in many cases through in situ measurements and hydrogeological analyses coupled with geomorphological analyses as for example in (Johnson & Sitar 1990; Anderson et al. 1997; De Vita et al. 2006; Cascini et al. 2000; Cascini et al. 2008).

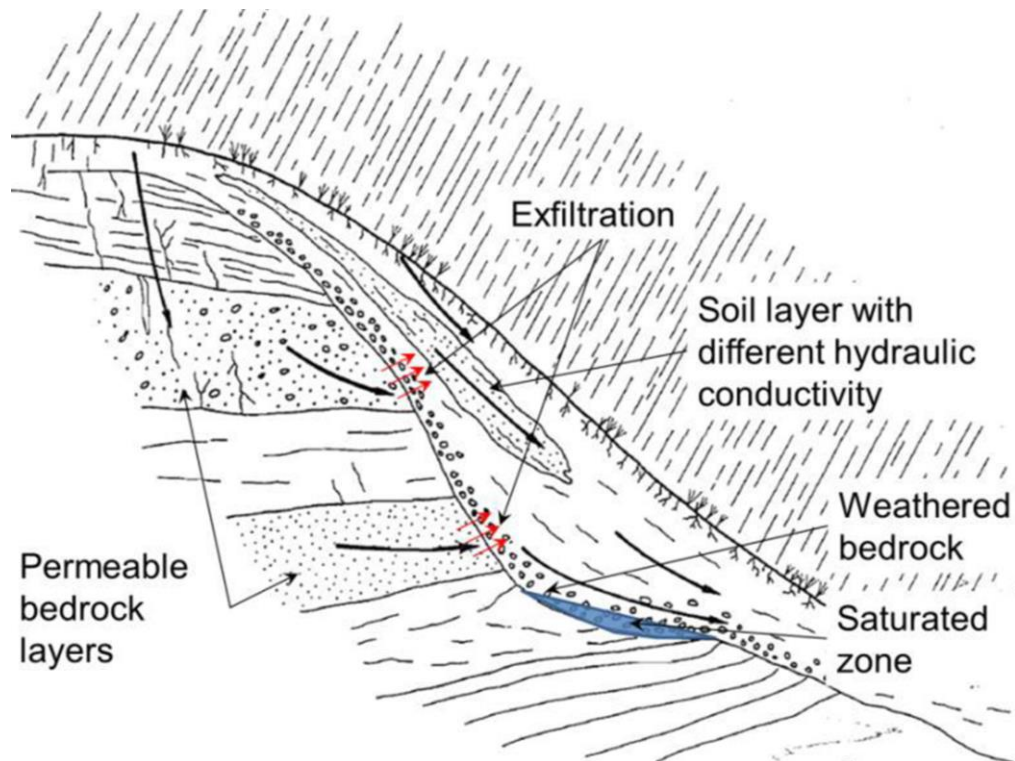


Fig. 3.4 Schematic diagram of groundwater circulation and of the hydraulic interactions between bedrock and the upper soil layer ((Askarinejad 2013) modified after Johnson & Sitar 1990)

3.4 Transient hydraulic response of slopes to rainfall infiltration

In this section the hydrologic processes (**Fig. 3.5**) that take place at hill slope scale are discussed.

According to (Take et al. 2004), the hydrologic equilibrium of a slope compromises four independent processes:

Unsaturated infiltration

Soil slopes are typically unsaturated. In the case where rainfall intensity is lower than the infiltration capacity at the soil surface the total amount of rainfall will infiltrate into the soil percolating quasi vertically downwards into the soil under the influence of gravity until it reaches a less permeable substratum or a groundwater table. In this case, suction will decrease but the slope (or the soil layers) might not necessarily become saturated. The observation of the development and propagation of this distinctive wetted zone is commonly described with the “wetting front” term. The wetting front is defined as the visible limit between the unsaturated zone that has not changed its water content yet and the zone which has experienced an increase in water content due to water infiltration.

Saturated transmission

In the latter case (where the underlying soil layer is less permeable) the infiltrating water will form a thin seepage layer (formation of water table) which will follow the contours of the low permeability material. As the flow quantity must increase with distance along the slope catchment area due to the integration of the rainfall infiltration applied over this area, the depth of the seepage layer will correspondingly increase in the down-slope direction.

Storage

If, the slope of the low permeability substratum decreases, a localised zone of high transient pore water pressure will be created within upper layer. By definition, one area of the slope in which the hydraulic gradient must change significantly is the toe of the slope. This is also arguably the most critical region of the slope from a stress perspective (Take et al. 2004).

Leakage

The exit gradient of the seepage flow will also influence the transient pore water pressures within the slope, and most particularly within the permeable layer. The elevated pore water pressures from such a scenario will be temporary, localised, and mostly dependent on the rainfall intensity, duration, and antecedent conditions.

When the transient pore water pressures reach a permeable layer, infiltrating rain water will be preferentially transmitted downslope within the permeable layer. If the inclined layer is close-ended, the leakage (or outflow) from the layer can be exceeded by the rate of

transmission of the seepage water, thereby ensuring a local transient build-up of pore water pressures.

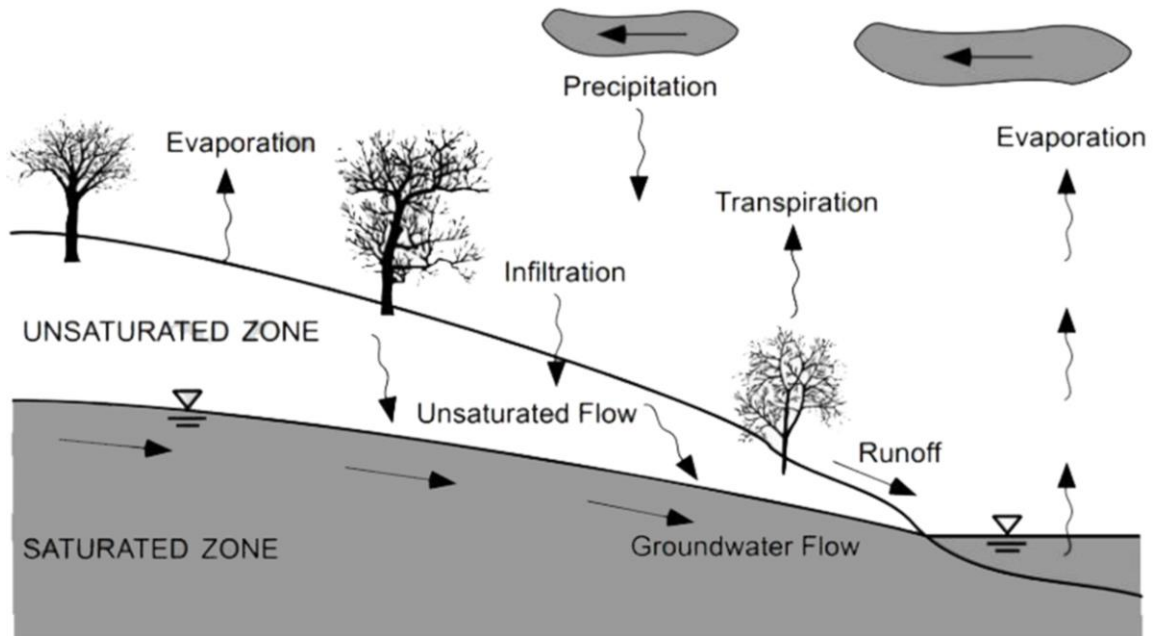


Fig. 3.5 Physical processes in the hydrologic cycle of natural slopes (Lu & Likos 2004)

Additionally, in the case where the rainfall intensity is higher than the infiltration capacity, the soil controls the amount of water infiltrating at the surface and the surplus of water results in runoff. The infiltrability is a time-dependent value controlled by the soil's saturated coefficient of permeability, the water relative permeability function and water retention properties. As rainfall stops, evaporation starts to be the dominant process which leads to the re-increase of matric suctions from the top down. Cycles of wet and dry periods lead to formation of wetting fronts which are followed then by drying fronts in the soil.

3.5 Controlling factors for rain infiltration and pore water pressure changes in unsaturated slopes

Slope stability analysis, especially for the case of rainfall-induced landslides, involves many parameters which are related to soil properties, slope geometry, groundwater conditions, initial conditions and rainfall characteristics.

According to (Rahardjo et al. 2007), the slope geometry and the initial water table determine the initial safety factor. The worst combination for safety factors constitute slopes with a high slope angle, a high slope height and a shallow initial depth of groundwater table and the actual failure conditions are much affected by rainfall characteristics and properties of the soils in the slope. Thus, attention should be paid to soil properties and rainfall characteristics when dealing with rainfall-induced landslides.

Soil hydraulic properties related to rainfall-induced slope failure include the soil–water retention behaviour (i.e. the air entry value and the slope of the soil-water characteristic curve) and the unsaturated permeability function. It has been shown that the saturated permeability of soil is considered as one of the most important soil properties in rainwater infiltration. According to (Tsaparas et al. 2002), for the same rainfall, the higher the value of k_{sat} , the greater the increment of pore water pressures from the initial conditions, the wetting front advances more rapidly, water table mounding is favoured and suction recovery after rainfall stops is faster. Hence the safety factor of the slope with a higher value of k_{sat} is smaller. Additionally, for a relatively low value of k_{sat} , pore water pressures increase strongly close to the surface while deeper layers remain unaffected. However, as for the same rainfall intensity (I), the effect of k_{sat} , on the reduction of safety factor can be different, it is suggested, according to (Kasim 1997; Zhang et al. 2004), to use the ratio I/k_{sat} rather than I in order to investigate the effect of soil hydraulic properties.

The effects of rainfall intensity, rainfall duration, and antecedent rainfall are the also the key factors when studying infiltration and slope stability analysis. It is generally accepted that the intensity of the rainfall is the primary factor which controls the magnitude of suction losses and the evolution of the groundwater table (Rahardjo et al. 2007). However, rainfall intensity and duration are dependent parameters. For a certain return period, the rainfall intensity and duration follow a certain relationship, called the intensity–duration–frequency (IDF) curve (i.e. the relationship between the rainfall intensity and duration for various return periods), which can be determined from statistical analysis of regional rainfall data. Based on this, the critical rainfall intensity and duration for a rainfall-induced slope failure can be determined; for more details see (Pradel & Raad 1993; Cho & Lee 2002). Finally, antecedent rainfall is also another factor which affects the slope stability under rainfall as suction will decrease due to rain flux

and the slope might be marginally safe before the major rainfall (Rahardjo et al. 2007; Tsaparas et al. 2002).

3.6 Stress paths in soil slopes

In the following a reference scheme (**Fig. 3.6**) is proposed by (Cascini et al. 2010) which outlines the major differences among slides, slides turning into flow, and flowslides and takes into account both direct rainfall infiltrating the slope surface and spring from the bedrock.

In particular, **Fig. 3.6** provides the effective stress paths in terms of the stress invariants q , p , for which the effective stress tensor is defined as in equation (3.8). In **Fig. 3.6** the displacement (δ), resisting force (F_r) and driving force (F_d) curves versus time are also presented.

As analyzed by (Cascini et al. 2010), for slides, (**Fig. 3.6b**), soil mechanical behaviour is controlled, in drained conditions, by the hydrologic response up to the failure onset. Resisting force (F_r) decreases up to the value of the driving force (F_d) along a slip surface that includes the zone where the spring from the bedrock is located, (Point A in **Fig. 3.6**) [**Fig. 3.6b**, $t=t_1$]. Drained conditions also remain, both for loose and dense soils, during the postfailure stage and small accelerations develop [**Fig. 3.6b**, $t>t_1$].

In loose saturated soils, the above process is associated with a volume reduction of the soil. If the pore-water pressure cannot freely dissipate, partially or totally undrained conditions develop during the post-failure stage and a flowslide occurs [**Fig. 3.6d**, $t=t_1$]. Particularly, in the spring zone (Point A in **Fig. 3.6**), pore water pressures build up and the soil follows a stress path 0 to 1, leading to a catastrophic failure [**Fig. 3.6d**, $t>t_1$]. Actually, the soil cannot sustain the imposed deviatoric stress q which leads to acceleration along the stress path from 1 [**Fig. 3.6d**, $t>t_1$].

Alternatively, slides can turn into flows (**Fig. 3.6c**), as a result of complex mechanisms characterized by a decreasing in the shear strength due to local hydraulic boundary conditions that can lead to fail the portion of the slope related to the spring zone [**Fig. 3.6b**, $t=t_1$]. Above this zone (Point B in **Fig. 3.6**), the mobilized shear stresses increase, both in loose and dense soils, due to the unbalanced driving forces along an upslope potential slip surface [**Fig. 3.6c**, $t>t_1$] and a further slide can occur [**Fig. 3.6c**, $t=t_2$]. The latter is characterized by a high initial acceleration and it consequently turns into a flow [**Fig. 3.6c**, $t>t_2$].

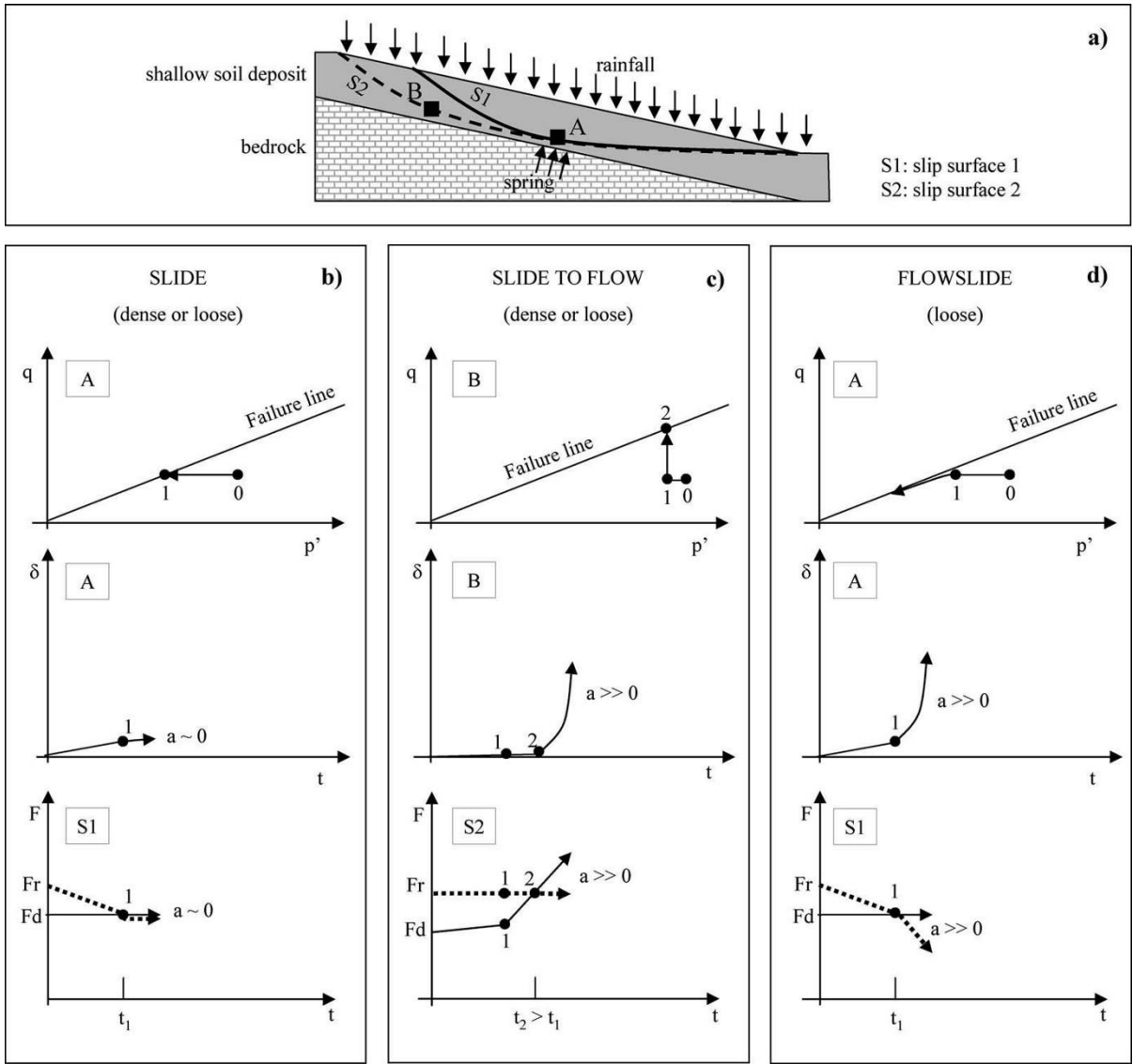


Fig. 3.6 Reference schemes adopted for the shallow landslides induced by rainfall directly infiltrating the slope surface and spring from the bedrock (Cascini et al. 2010)

Major differences between a flowslide (**Fig. 3.6d**) and a slide turning into flow (**Fig. 3.6c**) can be also outlined focusing on pore-water pressures at failure. For the analyzed schemes, pore water pressures reach the highest values at Point A (spring zone) due to both rainfall and local hydraulic boundary conditions (i.e., spring from bedrock) and the lowest values at Point B (above the spring zone) being related only to the rainfall. Finally, the pore water pressure values at failure can be negative at Point B (**Fig. 3.6c**) and slides turning into flow can also occur in portions of the slope characterized by unsaturated conditions.

What has to be taken also into account is the type of failure. In the cases presented in (**Fig. 3.6b** and **c**), drained failure takes place at the critical state line, and it can be of localized type (Pastor et al. 2002; Pastor et al. 2004).

On the contrary, fully or partially undrained post-failure stage of very loose materials (**Fig. 3.6d**) is of diffuse type (Fernandez Merodo et al. 2004; Darve & Laouafa 2000), and generation of pore water pressures has to be carefully considered by using suitable constitutive and mathematical models.

3.7 Modelling options for the simulation of the failure onset of the rainfall-induced landslides

The most common approach for the numerical modelling of slope failure in engineering practice is to uncouple the fluid flow and slope stability problem and treat them in a sequential fashion. In this sense, a seepage analysis is performed first (assuming a rigid solid skeleton) for the calculation of the water pressure distribution, which is then followed by a limit equilibrium analysis for the slope stability problem, as for example in (Cascini et al. 2005). However, as mentioned in (Cascini et al. 2010), in order to properly reproduce rainfall-induced landslides and the onset of the phenomenon, it is necessary to use: i) a mathematical model describing the coupling between pore fluids and soil skeleton; ii) a suitable constitutive relationship able to describe the unsaturated soil behavior; and iii) a numerical model where i) and ii) are implemented.

In this section, a brief overview of the modelling options that can be used in practice to study slope stability problems and more in particular the failure onset of rainfall-induced landslides, is presented.

3.7.1 Limit equilibrium analysis

In practice, the most conventional method for analysing slope stability is the limit equilibrium method (Taylor DW. 1948). As discussed also in (Laouafa & Darve 2002), much research has been carried out in this field since the first attempt by Culmann in 1866 to treat the slope stability problem mathematically. The most popular methods include the ordinary methods of slices proposed by Fellenius (Fellenius 1936), Bishop's modified method (Bishop 1955), Janbu's generalized procedure of slices (Janbu 1968), the Morgenstern and Price method (Morgenstern & Price 1965) and Spencer's methods (Spencer 1967). All these

methods are presented in Duncan's review (Duncan 1996) and presented in a general framework by (Espinoza et al. 1992).

Let us consider a simple slope as presented in **Fig. 3.7**.

If the potential sliding surface is decomposed into n slices as depicted in **Fig. 3.7(a)**, then the analysis based on static limit equilibrium leads to a total of $6n-2$ unknowns [**Fig. 3.7 (b)**]. From the static equilibrium conditions (3 equations per slice) of each slice, we obtain $3n$ equations. Additional assumptions have to be made in order to obtain a statically well-defined problem. It is commonly assumed in this theory that the normal and shear forces acting on the base of each slice follow the Mohr–Coulomb failure criterion, which induces n supplementary equations. The needed additional equations are then equal to $2n-2$. The differences between the conventional methods lie in the auxiliary constraints assumed in order to solve the problem.

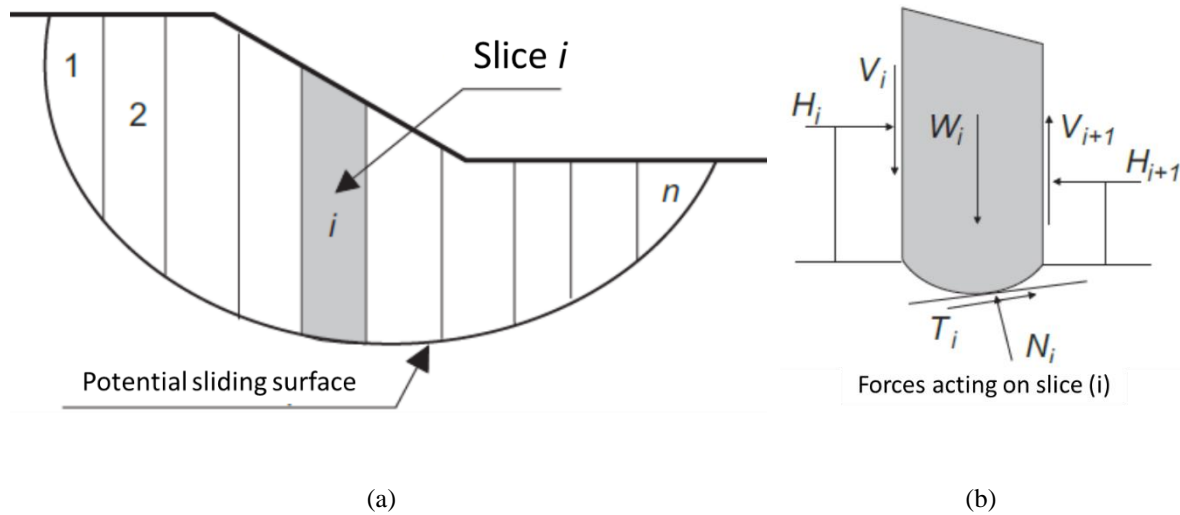


Fig. 3.7 Slope, slices and general unknowns in conventional methods (Laouafa & Darve 2002)

A common parameter introduced in the equilibrium methods is the so called factor of safety (FOS). This non-dimensional scalar is defined as follows:

$$FOS = \frac{\text{shear strength of the soil } (\tau_{max})}{\text{shear strength required for equilibrium } (\tau)} \quad (3.9)$$

The FOS could be defined as the factor by which the shear strength of the slope soil has to be reduced in order to bring the slope to the state of failure. For a given problem, the slope is considered to be stable as soon as FOS is greater than one.

Although these methods are widely used in practice, they have certain shortcomings and inaccuracies including (Laouafa & Darve 2002):

- The factor of safety is a local parameter that is assumed constant along the slip line.
- The sliding mass of soil is assumed to be rigid. The sliding mechanism creates complex stress and strain distributions inside the sliding mass and the remaining soil, which are not taken into account.
- Stress path dependency and stress-strain history are not considered.
- Velocity and strain (at the material point level or global level) are not taken into account.
- The sliding mechanism is supposed to affect instantaneously the whole sliding surface (all material points belonging to the slip surface) at the same time which excludes the possibility, in other words, of an initiation at some stage of loading and progressive development of the sliding surface.
- These methods do not involve time evolution of any mechanical or physical quantities.
- The normal stress distribution is not well reproduced (Tavenas et al. 1980) and the conventional analyses consistently ignore the incremental genesis of the slope (Chowdhury 1981) and thus can never give the true stress distribution.
- The shape of the sliding or the slip surface is in general a priori assumed.
- The soil is assumed not to have a stress–strain behaviour with softening.
- The stability of the slope is only checked by the mean of a shear strength criterion, while there exist other modes of failure at lower stress levels.

3.7.2 Finite element method analysis

According to (Laouafa & Darve 2002), numerical non-linear analysis based on the finite element method in conjunction with accurate constitutive models describing soil behaviour constitutes the other modelling alternative in slope stability analysis. This numerical method

can be applied to a wider and more complex geotechnical field including transient problems, thermo-hydro mechanical coupling and non-linear static and dynamic problems.

Slope stability analysis using the finite element method has received wide attention in research community. For reviews, see (Duncan 1996) and (Griffiths & Lane 1999).

Here the approach can be coupled or also uncoupled. An uncoupled stress-strain model can be obtained based on the simplifying assumption that the deformation rate is neglected from the mass balance equations as described in (Cascini et al. 2010). In this case the pore pressure influences the mechanical behavior but in turn the latter does not influence the former. More exact solutions to the coupled hydro-mechanical analysis are obtained when the soils in the slope are considered deformable and in variably saturated conditions. For this reason, in this work the modelling of rainfall induced landslides is considered as a coupled variably saturated hydro-mechanical problem. For the numerical simulations the geometrically linear finite element code Comes-Geo developed at the University of Padova, Italy, is used, in which soils are considered as non-isothermal elasto-plastic multiphase solid porous materials as developed in (Sanavia et al. 2006; Sanavia et al. 2008; Sanavia 2009) following the works of (Lewis & Schrefler 1998) and (Hassanizadeh & Gray 1979a; Hassanizadeh & Gray 1979b; Hassanizadeh & Gray 1980). The mathematical and numerical model are extensively detailed in chapters 4 and 5.

In addition, in this case of slope stability analysis we can distinguish two main trends as mentioned in (Laouafa & Darve 2002). The first aims at describing the mechanism of failure by a plasticity criterion and the second is based on the bifurcation of the strain field into a localised mode (localisation theory).

The FE method overcomes the shortcomings already discussed by reducing considerably the number of assumptions. The factor of safety, as emphasized by (Griffiths & Lane 1999), emerges naturally from the FEM analysis without any assumption of a particular mechanism on sliding.

Although the robustness of FEM analysis and its ability to predict slope stability are well recognised, the question of the sliding or failure criterion and its definition remain. There is no unique definition of a global failure. Zienkiewicz and Taylor, (Zienkiewicz & Taylor 1989) for example, utilized the non-convergency of the iterative algorithm to define the failure, which represents a purely numerical definition. One of the principal features of a finite element

analysis of slope stability, except for those including the localisation of strains, is that at a local level (i.e. at a material point level), the failure is driven by a plastic failure criterion. This failure criterion is in some approaches reduced by a scalar (shear strength reduction method in (Matsui & San 1992), (Griffiths & Lane 1999)) during the analysis until the chosen global failure criterion is fulfilled.

However, non-associated materials such as soils and rocks, exhibit unstable stress states strictly inside the failure domain. These states are reached before the plastic limit and one can find at these specific states a set of perturbation loads which lead to large responses. The material response for such loading will not obey to any plastic flow rule, as expected on the failure surface. In other words, strictly inside the set of admissible stresses defined by the failure envelope, there exists at least one loading (stress controlled, strain controlled or mixed) such that no bounded response exists.

The second trend in finite element analysis of slope stability is based on the localisation of deformation in a narrow band (Leroy & Ortiz 1989; Leroy et al. 1987; Rugeiro & Borja 1999). This phenomenon (Rudnicki & Rice 1975; Rice 1976) constitutes a particular material instability which leads, at a given time step of loading, to a bifurcation of the solution. A certain class of landslides can be well described and explained using localisation theory. When the sliding process is driven by the inception of a narrow band (localised deformation into a shear band), the finite element model will be able to detect the singularity of the phenomenon and one can expect to perform accurate modelling of the mechanical problem. However, the material instability could lead to diffuse modes of failure and not only localised modes. Such cases can be predicted by a material stability analysis based on the sign of the second order work as it has been analysed in chapter 2 and it will be shown in the case studies which are presented in chapter 6.

4 Mechanics of porous media: mathematical model

4.1 Introduction

In this chapter the governing equations for the fully dynamic behaviour of a partially porous medium are developed (Lewis & Schrefler 1998). In particular, the voids are considered to be filled with water and moist air. The description of multiphase systems made of interpenetrating continuous bodies, such as porous media, is today based either on mixture theory integrated by the concept of volume fractions, or on averaging methods and from a classical viewpoint on Biot's theory. Since the averaging theories offer the possibilities of a better understanding of the microscopic situation and its relation to the macroscopic one, which is, however, the natural domain of all continuum mechanical models, we use in the following the averaging theory based on spatial averaging operators. Within this theory we make use of macroscopic variables which correspond to real measurable quantities directly linked to laboratory practice, e.g. in soil mechanics. It is noted that, under appropriate assumptions, the averaging theory yields the same equations as the classical mixture theory, as shown in (de Boer et al. 1991). Care has to be taken, however, in the linear momentum balance equation as explained in section 4.3.3.

For the reader mainly interested in the resulting governing equations and their numerical solution we derive these equations again in section 4.6 using Biot's theory. This also permits us to establish a link between the classical, phenomenological approach and the description of the real microscopic composition of the multiphase system. Furthermore, it shows the essential correctness of Biot's findings.

Tensorial notation is used throughout this chapter.

4.2 Averaging principles

Here only a short summary of the principles necessary for the development of the governing equations is given. For a full account of the averaging theories the reader is referred to (de Boer et al. 1991) and (Bear & Bachmat 1984). Sections 4.1 and 4.3 follow, in particular, the work by Hassanizadeh and Gray (Hassanizadeh & Gray 1979a), (Hassanizadeh 1986) and by de Boer et al. (de Boer et al. 1991).

We introduce the following definitions (Lewis & Schrefler 1998):

- **microscopic level:** we consider the real non-homogeneous structure of the porous medium domain (**Fig. 4.1**). The scale of inhomogeneity is of the order of magnitude of the dimensions of a pore or a grain, say d . Attention is focused on what happens at a mathematical point within a single phase and the field variables describing the status of a phase are defined only at the points occupied by that phase. For the practical description of the processes taking place in a porous medium, this level is not useful since microscopic quantities are generally not measurable. Only their average values are measurable.
- **macroscopic level:** the real multiphase system that occupies the porous medium domain is replaced by a model in which each phase is assumed to fill up the entire domain. This means that at every point all phases are supposed present at the same time (overlapping continua). This is the level of interest of continuum mechanics, where we investigate the continuous distribution of the constituents through a macroscopic control space. At this level, we usually deal with homogeneous media, but non-homogeneities may still be present, e.g. strata. Their scale is of the order of magnitude comparable with the order of magnitude of the entire domain, say L .
- **megascopic level:** at this level the conditions are similar to those of the previously defined level. The difference depends on the fact that some macroscopic inhomogeneities are eliminated by averaging and/or on the fact that the mathematical model is stated in a domain which has less dimensions than the real domain, e.g. 2-D problem with field values averaged over the thickness (Bear & Corapcioglu 1981; Simoni & Schrefler 1989). Typical applications of this level are found in the simulation of land subsidence problems of regional scale.

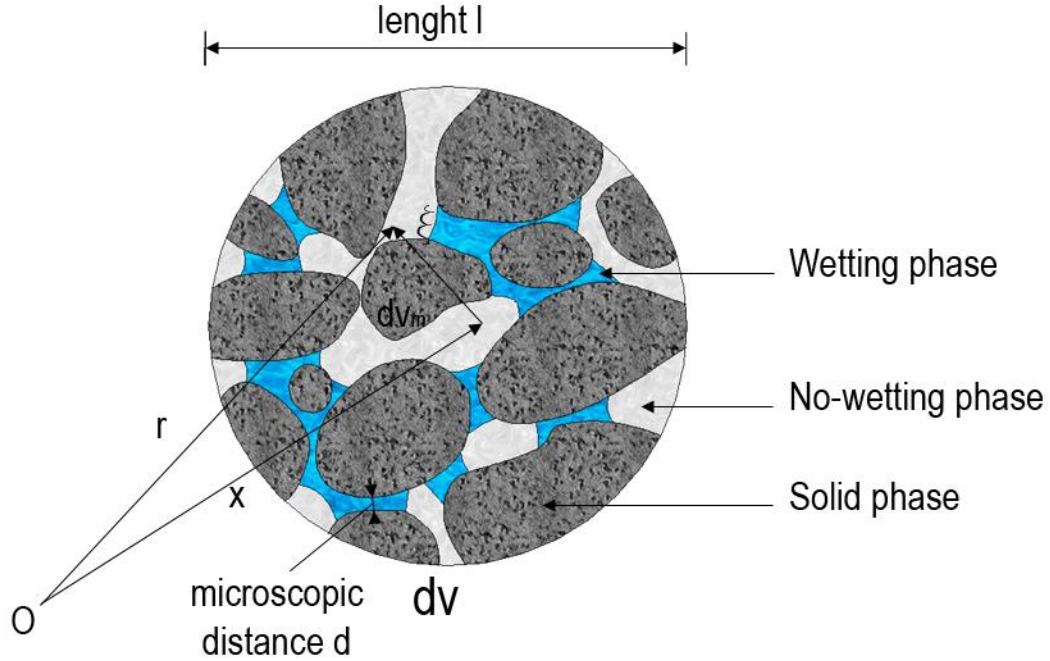


Fig. 4.1: Typical averaging volume dv of a porous media consisting of three constituents

4.2.1 Averaging process

We consider here a multiphase system occupying a total volume, V , and bounded by surface, A . According to (Lewis & Schrefler 1998), the constituents $\pi=1,2,\dots,k$ have the partial volumes V_π . Each point of the total volume, V , is considered to be the centroid of a representative elementary volume (R.E.V.) or average volume element, dv . The position of the centre of an R.E.V. in a global coordinate system is described by position vector x while r indicates the position of a microscopic volume element, dv_m , see Figure **Fig. 4.1**. The volume of constituent π within a R.E.V, called average volume element dv^π , is obtained by defining a phase distribution function, γ^π :

$$\gamma^\pi(\mathbf{r}, t) = \begin{cases} 1 & \text{for } \mathbf{r} \in dv^\pi \\ 0 & \text{for } \mathbf{r} \in dv^\alpha \quad \pi \neq \alpha \end{cases} \quad (4.1)$$

where $\mathbf{r} = \mathbf{x} + \boldsymbol{\xi}$ and the integration refers to the microscopic local coordinate system with its origin in x (**Fig. 4.1**).

Similarly we write for the part of area $d\alpha^\pi$ of the R.E.V, occupied by constituent π :

$$d\alpha^\pi(\mathbf{x}, t) = \int_{da} \gamma^\pi(\mathbf{r}, t) da_m \quad (4.2)$$

where da_m is the microscopic area element.

The knowledge of dv^π enables the introduction of the concept of volume fraction, η^π , which is of paramount importance in multiphase systems:

$$\eta^\pi(\mathbf{x}, t) = \frac{dv^\pi}{dv} = \frac{1}{dv} \int_{dv} \gamma^\pi(\mathbf{r}, t) dv_m \quad (4.3)$$

with $\sum_{\pi=1}^{\kappa} \eta^\pi = 1$.

In fact, as indicated under the heading "macroscopic level" in paragraph 4.1, substitute continua fill the entire domain simultaneously, instead of the real fluids and the solid which each fill only part of it. These substitute continua have a reduced density which is obtained through the volume fractions.

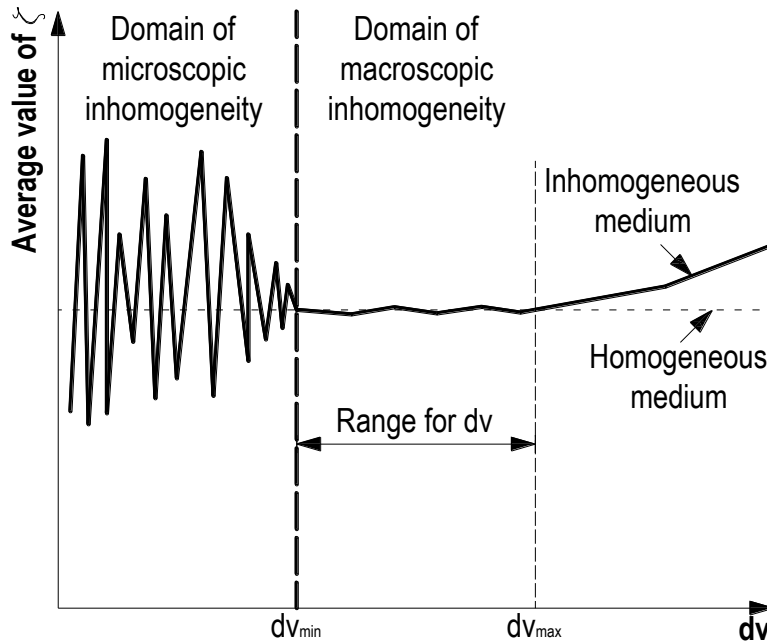


Fig. 4.2 Averaged value z versus size of the average volume dv

In the following, averaged quantities are obtained by integrating (averaging) a microscopic quantity over the volume, dv , or the area, $d\alpha$, of an R.E.V. A field of macroscopic variables results from this, where the average volume, dv , and the average area, $d\alpha$, is associated with material points.

The importance in the choice of size of an R.E.V. is self-evident. Average quantities have to be independent of the size of the average volume and continuous in space and time. Thus an R.E.V. has to fulfil the following requirements:

- dv has to be small enough to be considered as infinitesimal, i.e. the partial derivatives appearing in the governing equations must make sense
- dv must be large enough, with respect to the heterogeneities of the material to give average quantities without fluctuations depending on the size of the R.E.V., Figure **Fig. 4.2**.

To obtain meaningful average values, the characteristic length, l , of the average volume must satisfy the inequality: $d \ll l \ll L$, where l is dependent on the specific material which constitutes the medium.

Some typical values of l are given in (Lemaitre & Chaboche 1988)

Table 1: Characteristic length l for some materials

	l (mm)
metals	0.5
plastic	1.0
wood	10

The following average operators are now defined and applied to a function, ζ , which is a microscopic field variable.

Volume average operators

- Phase average:

$$\langle \zeta \rangle_{\pi}(\mathbf{x}, t) = \frac{1}{dv} \int \zeta(\mathbf{r}, t) \gamma^{\pi}(\mathbf{r}, t) dv_m \quad (4.4)$$

- Intrinsic phase average:

$$\langle \zeta \rangle_{\pi}^{\pi}(\mathbf{x}, t) = \frac{1}{dv^{\pi}} \int \zeta(\mathbf{r}, t) \gamma^{\pi}(\mathbf{r}, t) dv_m \quad (4.5)$$

From the definition of volume fraction (4.3) it follows that:

$$\langle \zeta \rangle_\pi(\mathbf{x}, t) = \eta^\pi(\mathbf{x}, t) \langle \zeta \rangle_\pi^\pi(\mathbf{x}, t) \quad (4.6)$$

Mass average operator, with $\rho(\mathbf{r}, t)$ microscopic mass density as weighting function:

$$\bar{\zeta}^\pi(\mathbf{x}, t) = \frac{\int_{dv} \rho(\mathbf{r}, t) \zeta(\mathbf{r}, t) \gamma^\pi(\mathbf{r}, t) dv_m}{\int_{dv} \rho(\mathbf{r}, t) \gamma^\pi(\mathbf{r}, t) dv_m} \quad (4.7)$$

with constant microscopic mass density the following equation holds:

$$\frac{1}{\eta^\pi(\mathbf{x}, t)} \langle \zeta \rangle_\pi(\mathbf{x}, t) = \bar{\zeta}^\pi(\mathbf{x}, t) \quad (4.8)$$

Area average operator

$$\bar{\zeta}^\pi(\mathbf{x}, t) = \frac{1}{da} \int_{da} \zeta(\mathbf{r}, t) \mathbf{n} \gamma^\pi(\mathbf{r}, t) da_m \quad (4.9)$$

with \mathbf{n} the outward normal unit vector of an area element da_m and ζ has a tensorial nature.

In the following, averages of velocity, external body force, internal energy, external supply of heat, internal entropy, external supply of entropy and total production of entropy are obtained through the mass average operator (Hassanizadeh & Gray 1979a).

4.2.2 Microscopic balance equations

We now consider the classical balance equations of continuum mechanics which are used to describe the microscopic situation of any π phase (Lewis & Schrefler 1998). At the interfaces with other constituents, the material properties and thermodynamic quantities may present step discontinuities.

For a generic conserved variable, ψ , the conservation equation within the π phase may be written as:

$$\frac{\partial(\rho\psi)}{\partial t} + \text{div}(\rho\psi\dot{\mathbf{r}}) - \text{div} \mathbf{i} - \rho\mathbf{b} = \rho\mathbf{G} \quad (4.10)$$

where $\dot{\mathbf{r}}$ is the local value of the velocity field of the phase in a fixed point in space, \mathbf{i} is the flux vector associated with ψ , \mathbf{b} is the external supply of ψ and \mathbf{G} is the net production of ψ .

At the interface between two constituents π and α , the jump condition holds:

$$\left[\rho\psi(\mathbf{w} - \dot{\mathbf{r}}) + \mathbf{i} \right] \Big|_{\pi} \cdot \mathbf{n}^{\pi\alpha} + \left[\rho\psi(\mathbf{w} - \dot{\mathbf{r}}) + \mathbf{i} \right] \Big|_{\alpha} \cdot \mathbf{n}^{\alpha\pi} = 0 \quad (4.11)$$

where \mathbf{w} is the velocity of the interface, $\mathbf{n}^{\pi\alpha}$ is the unit normal vector pointing out of the π phase and into the α phase, with $\mathbf{n}^{\pi\alpha} = -\mathbf{n}^{\alpha\pi}$ and $\Big|_{\pi}$ indicates that the preceding term [...] must be evaluated with respect to the π phase.

No thermomechanical properties are attributed to these interfaces. This assumption does not exclude the possibility of exchange of mass, momentum or energy between the constituents.

Moreover the local thermodynamic equilibrium hypothesis is assumed to hold because the time scale of the modelled phenomena is substantially larger than the relaxation time required to reach equilibrium locally.

4.2.3 Macroscopic balance equations

Instead of deriving the macroscopic balance equation separately for each quantity to which the conservation law applies, in (Lewis & Schrefler 1998) it is derived for the generic quantity ψ as in (de Boer et al. 1991) and (Bear & Bachmat 1984) and the law is specialised afterwards for specific quantities: mass, linear momentum, angular momentum and energy. Note that the balance equations are written in a material free manner. The constitutive equations are introduced successively.

A general, average macroscopic balance equation is obtained from the microscopic balance equation (4.12) by multiplying it with the distribution function $\gamma^{\pi}(\mathbf{r}, t)$ and by integrating this product over the volume element, dv , and over the total volume, V . In this elaboration of the balance equations, macroscopic quantities are obtained through the previously defined averaging operators.

This averaging procedure yields that ((de Boer et al. 1991) and (Bear & Bachmat 1984)) :

$$\begin{aligned}
& \int_V \left[\frac{1}{dv} \int_{dv} \frac{\partial(\rho(\mathbf{r},t)\psi(\mathbf{r},t))}{\partial t} \gamma^\pi(\mathbf{r},t) dv_m \right] dV \\
& + \int_V \left[\frac{1}{dv} \int_{dv} \operatorname{div}(\rho(\mathbf{r},t)\dot{\mathbf{r}}(\mathbf{r},t)\psi(\mathbf{r},t)) \gamma^\pi(\mathbf{r},t) dv_m \right] dV \\
& - \int_V \left[\frac{1}{dv} \int_{dv} \operatorname{div} \mathbf{i}(\mathbf{r},t) \gamma^\pi(\mathbf{r},t) dv_m \right] dV \\
& - \int_V \left[\frac{1}{dv} \int_{dv} \operatorname{div} \mathbf{i}(\mathbf{r},t) \gamma^\pi(\mathbf{r},t) dv_m \right] dV \\
& - \int_V \left[\frac{1}{dv} \int_{dv} \rho(\mathbf{r},t) \mathbf{b}(\mathbf{r},t) \gamma^\pi(\mathbf{r},t) \right] dV \\
& = \int_V \left[\frac{1}{dv} \int_{dv} \rho(\mathbf{r},t) \mathbf{G}(\mathbf{r},t) \gamma^\pi(\mathbf{r},t) dv_m \right] dV
\end{aligned} \tag{4.12}$$

As suggested in, (Hassanizadeh & Gray 1979a; Hassanizadeh & Gray 1979b; Hassanizadeh & Gray 1980) and (de Boer et al. 1991), it is possible obtain the following form of the general balance equation for the macroscopic thermodynamic property $\bar{\psi}^\pi$ associated with the phase:

$$\begin{aligned}
& \int_V \left\{ \frac{\partial}{\partial t} \left[\langle \rho \rangle_\pi(\mathbf{x},t) \bar{\psi}^\pi(\mathbf{x},t) \right] + \operatorname{div} \left[\langle \rho \rangle_\pi(\mathbf{x},t) \bar{\mathbf{v}}^\pi(\mathbf{x},t) \bar{\psi}^\pi(\mathbf{x},t) \right] \right\} dV \\
& - \int_V \left\{ \frac{1}{dv} \sum_{\alpha \neq \pi}^k \int_{da^{\pi\alpha}} \rho(\mathbf{r},t) \psi(\mathbf{r},t) [\mathbf{w}(\mathbf{r},t) - \dot{\mathbf{r}}(\mathbf{r},t)] \cdot \mathbf{n}^{\pi\alpha}(\mathbf{r},t) da_m \right\} dV \\
& - \int_V \left[\frac{1}{dv} \sum_{\alpha \neq \pi}^k \int_{da^{\pi\alpha}} \mathbf{i}(\mathbf{r},t) \cdot \mathbf{n}^{\pi\alpha}(\mathbf{r},t) da_m \right] dV \\
& - \int_A \left\{ \frac{1}{da} \int_{da} [\mathbf{i}(\mathbf{r},t) - \rho(\mathbf{r},t) \tilde{\psi}^\pi(\mathbf{x},\xi,t) \tilde{\mathbf{r}}^\pi] \cdot \mathbf{n}(\mathbf{r},t) \gamma^\pi da_m \right\} dA \\
& - \int_V \langle \rho \rangle_\pi(\mathbf{x},t) \bar{\mathbf{b}}^\pi(\mathbf{x},t) dV = \int_V \langle \rho \rangle_\pi(\mathbf{x},t) \bar{\mathbf{G}}^\pi(\mathbf{x},t) dV
\end{aligned} \tag{4.13}$$

or in more concise form:

$$\begin{aligned}
& \left[\int_V \left[\frac{\partial}{\partial t} \left(\langle \rho \rangle_\pi \bar{\psi}^\pi \right) + \operatorname{div} \left(\langle \rho \rangle_\pi \bar{\psi}^\pi \bar{\mathbf{v}}^\pi \right) - \operatorname{div} \mathbf{i}^\pi \right. \right. \\
& \left. \left. - \langle \rho \rangle_\pi \left[\bar{\mathbf{b}}^\pi + e^\pi(\rho\psi) + \mathbf{I}^\pi \right] \right] dV = \int_V \rho_\pi \bar{\mathbf{G}}^\pi dv
\end{aligned} \tag{4.14}$$

where \mathbf{i}^π is the flux vector associated with $\bar{\psi}^\pi$, \bar{b}^π is the external supply of $\bar{\psi}^\pi$, $\langle \rho \rangle_\pi$ is the volume average value of mass density.

This last balance equation contains two further interaction terms, which describe chemical and physical exchanges.

Exchange of due to mechanical interactions between the constituents is given by:

$$\mathbf{I}^\pi = \frac{1}{\langle \rho \rangle_\pi} dv \sum_{\alpha \neq \pi} \int_{da^{\pi\alpha}} \mathbf{n}^{\pi\alpha} \cdot \mathbf{i} da_m \quad (4.15)$$

Phase change of a constituent or possible mass exchange between the constituent π and the other constituents α is given by:

$$e^\pi(\rho\psi) = \frac{1}{\langle \rho \rangle_\pi} dv \sum_{\alpha \neq \pi} \int_{da^{\pi\alpha}} \rho\psi (\mathbf{w} - \dot{\mathbf{r}}) \cdot \mathbf{n}^{\pi\alpha} da_m \quad (4.16)$$

4.3 Macroscopic balance equations for a non-isothermal partially saturated porous medium

In this section, the macroscopic balance equations for mass, linear momentum, angular momentum and energy (enthalpy) are obtained and then specialised for a deforming porous material where heat transfer and flow of water (liquid and vapour) and of dry air is taking place. The starting points are the microscopic balance equations (4.12), where, for each constituent, the generic thermodynamic variable, ζ , is replaced by appropriate microscopic quantities, suitable for a microscopic non polar material (Lewis & Schrefler 1998).

For the proper description of the non-isothermal unsaturated porous medium we need to take into account not only heat conduction and vapour diffusion, but also heat convection, liquid water flow due to pressure gradients or capillary effects and latent heat transfer due to water phase change (evaporation and condensation) inside the pores. Furthermore the solid is deformable, resulting in coupling of the fluid, the solid and the thermal fields. All fluid phases are in contact with the solid phase.

The constituents are assumed to be immiscible except for dry air and vapour, and chemically non reacting. Because of the local thermodynamic equilibrium hypothesis, the temperatures of each constituent at a point in the multiphase medium are taken to be equal. This does not mean

that the temperature is uniform throughout the medium but only that at each point one temperature is sufficient to characterize the state.

Momentum exchanges due to mechanical interaction are independent of the temperature gradient.

In the following, the stress is defined as tension positive for the solid phase, while pore pressure is defined as compressive positive for the fluids.

It should be noticed that in this section the formulation is still material free, i.e. no specific assumptions for the material behaviour have been introduced so far, except for the quite general ones, indicated above. For the development of the macroscopic balance equations in the following sections, we still need to specify kinematics.

4.3.1 Kinematic equations

As indicated in section 4.2 a multiphase medium can be described as the superposition of all π phases, whose material points, \mathbf{X}^π , can be thought of as occupying simultaneously each spatial point \mathbf{x} in the actual configuration. The state of motion of each phase is, however, described independently. Based on these assumptions, the kinematics of a multiphase medium is dealt with next.

In a Lagrangian or material description of motion, the position of each material point, \mathbf{x}^π , at time, t , is function of its placement in a chosen reference configuration, and of the current time, t :

$$\mathbf{x}^\pi = \mathbf{x}^\pi(\mathbf{X}^\pi, t) \quad (4.17)$$

To have this mapping continuous and bijective at all times, the Jacobian, J , of this transformation must be non-zero and strictly positive, since it is equal to the determinant of the deformation gradient tensor, \mathbf{F}^π :

$$\mathbf{F}^\pi = \text{Grad } \mathbf{x}^\pi \quad (\mathbf{F}^\pi)^{-1} = \text{Grad } \mathbf{X}^\pi \quad (4.18)$$

Because of the non-singularity of the Lagrangian relationship (4.17), it is possible to write its inverse and obtain Eulerian or spatial description of motion:

$$\mathbf{X}^\pi = \mathbf{X}^\pi(\mathbf{x}^\pi, t) \quad (4.19)$$

It is also assumed that functions which describe the motion have continuous derivatives. If the path of the particle of the π phase is known, its velocity and acceleration are, in the material description:

$$\mathbf{V}^\pi = \frac{\partial \mathbf{x}^\pi(\mathbf{X}^\pi, t)}{\partial t} \quad (4.20)$$

$$\mathbf{A}^\pi = \frac{\partial^2 \mathbf{x}^\pi(\mathbf{X}^\pi, t)}{\partial t^2} \quad (4.21)$$

The corresponding spatial expression can be obtained by introducing equation (4.36) into the above two equations. But, if only the spatial description is given for the velocity field in the form:

$$\mathbf{v}^\pi = \mathbf{v}^\pi(\mathbf{x}^\pi, t) \quad (4.22)$$

to evaluate its time derivative with material coordinates held constant, we introduce the description of motion of equation (4.17) into the last equation. By applying the chain rule of differentiation, it follows:

$$\mathbf{a}^\pi = \frac{\partial \mathbf{v}^\pi}{\partial t} + \text{grad } \mathbf{v}^\pi \cdot \mathbf{v}^\pi \quad (4.23)$$

The material time derivative of any differentiable function, $f^\pi(\mathbf{x}, t)$, given in its spatial description and referring to a moving particle of the phase is:

$$\frac{D^\pi f^\pi}{Dt} = \frac{\partial f^\pi}{\partial t} + \text{grad } f^\pi \cdot \mathbf{v}^\pi \quad (4.24)$$

If superscript α is used for the operator $\frac{D}{Dt}$, we obtain:

$$\frac{D^\alpha f^\pi}{Dt} = \frac{\partial f^\pi}{\partial t} + \text{grad } f^\pi \cdot \mathbf{v}^\alpha \quad (4.25)$$

the time derivative is taken moving with the α phase.

Subtraction of equation (4.24) from equation (4.25) yields the following relation:

$$\frac{D^\alpha f^\pi}{Dt} = \frac{D^\pi f^\pi}{Dt} + \text{grad } f^\pi \cdot \mathbf{v}^{\alpha\pi} \quad (4.26)$$

where $\mathbf{v}^{\alpha\pi} = \mathbf{v}^\alpha - \mathbf{v}^\pi$ is the velocity of the α phase with respect to the π phase. This velocity is called the diffusion velocity (Hassanizadeh & W.G. 1980).

The operator $\frac{D}{Dt}$ is a scalar operator and may be applied either to a vector quantity or a scalar quantity. If f^π is a vector property per unit volume referring to the π phase, the total time derivative of its integral over a volume, V , is given by:

$$\frac{d}{dt} \int_v f^\pi dV = \int_v \left(\frac{\partial f^\pi}{\partial t} + \text{grad } f^\pi \cdot \mathbf{v}^\pi + f^\pi \text{div } \mathbf{v}^\pi \right) dV = \int_v \left[\frac{\partial f^\pi}{\partial t} + \text{div} (f^\pi \otimes \mathbf{v}^\pi) \right] dV \quad (4.27)$$

For a scalar property, f^π :

$$\frac{d}{dt} \int_v f^\pi dV = \int_v \left(\frac{\partial f^\pi}{\partial t} + \text{div} (f^\pi \mathbf{v}^\pi) \right) dV \quad (4.28)$$

In the above equations, velocities and accelerations of the π phase are considered as mass averaged quantities since these are the quantities usually measured in a field situation or in laboratory practice. In porous media theory it is customary to describe the motion of the fluid phases in terms of mass averaged velocities relative to the moving solid. Their motion is described with reference to the actual configuration assumed by the solid skeleton. The velocities and accelerations of each fluid particle can then be written with reference to the ones of corresponding solid points, once the relative velocities are introduced. We specify the superscripts π now as s for soil, w for the liquid phase and g for the gas phase (dry air plus vapour) and write for the relative velocities of water and gas phase respectively:

$$\mathbf{v}^{ws} = \mathbf{v}^w - \mathbf{v}^s \quad (4.29)$$

$$\mathbf{v}^{gs} = \mathbf{v}^g - \mathbf{v}^s \quad (4.30)$$

Water and gas acceleration are given from (4.23), (4.25), (4.29) and (4.30) as:

$$\mathbf{a}^w = \mathbf{a}^s + \frac{D^s \mathbf{v}^{ws}}{Dt} + \text{grad} (\mathbf{v}^s + \mathbf{v}^{ws}) \cdot \mathbf{v}^{ws} \quad (4.31)$$

$$\mathbf{a}^g = \mathbf{a}^s + \frac{D^s \mathbf{v}^{gs}}{Dt} + \text{grad} (\mathbf{v}^s + \mathbf{v}^{gs}) \cdot \mathbf{v}^{gs} \quad (4.32)$$

The deformation process of the solid skeleton can be described by the velocity gradient tensor, \mathbf{L}^s , which, referred to spatial co-ordinates, is given by (Chen & Tsui 1992) and (Molenkamp 1986) :

$$\mathbf{L}^s \equiv \text{grad} \mathbf{v}^s = \mathbf{D}^s + \mathbf{W}^s \quad (4.33)$$

Its symmetric part \mathbf{D}^s , is called the eulerian strain rate tensor, being related to pure straining while its skew-symmetric component \mathbf{W}^s is the spin tensor.

4.3.2 Mass balance equations

In the averaging procedure, volume density parameters η^π (volume fractions) appear which are expressed in terms of commonly used variables in multiphase flow.

For solid phase: $\eta^s = 1 - n$, where $n = \frac{dv^w + dv^g}{dv}$ is the porosity.

For water: $\eta^w = n \cdot S_w$, where $S_w = \frac{dv^w}{dv^w + dv^g}$ is the degree of water saturation.

For gas: $\eta^g = n \cdot S_g$, where $S_g = \frac{dv^g}{dv^w + dv^g}$ is the degree of gas saturation.

It follows immediately that:

$$S_w + S_g = 1 \quad (4.34)$$

Solid phase

In the microscopic situation, the variables for solid in equation (4.12) assume the following values:

$$\psi = 1, \mathbf{i} = 0, b = 0, G = 0 \quad (4.35)$$

and the microscopic mass balance equation results in:

$$\frac{\partial \rho}{\partial t} + \operatorname{div}(\rho \dot{\mathbf{r}}) = 0 \quad (4.36)$$

The averaged macroscopic solid mass balance equation is:

$$\frac{\partial \rho_s}{\partial t} + \operatorname{div}(\rho_s \bar{\mathbf{v}}^s) = \rho_s e^s(\rho) \quad (4.37)$$

where ρ_s stands simply for $\langle \rho \rangle_\pi$, the phase averaged solid density and $\bar{\mathbf{v}}^s$ is the mass averaged solid velocity. The same simplified notation will be used for the other constituents, once π is accordingly specified.

From (4.24) we have:

$$\frac{D^s \rho_s}{Dt} = \frac{\partial \rho_s}{\partial t} + \operatorname{grad} \rho_s \cdot \bar{\mathbf{v}}^s \quad (4.38)$$

By introducing the latest in the previous equation we obtain:

$$\frac{D^s \rho_s}{Dt} + \rho_s \operatorname{div} \bar{\mathbf{v}}^s = 0 \quad (4.39)$$

By introducing intrinsic phase averaged densities through equation (4.8) we have finally:

$$\frac{D^s(1-n)\rho^s}{Dt} + \rho^s(1-n)\operatorname{div} \bar{\mathbf{v}}^s = 0 \quad (4.40)$$

where the shorthand $\rho_s = \langle \rho \rangle_s^s$ has been introduced for the intrinsic phase averaged density.

Liquid phase water

As for the solid phase we have:

$$\frac{\partial \rho_w}{\partial t} + \operatorname{div}(\rho_w \bar{\mathbf{v}}^w) = \rho_w e^w(\rho) \quad (4.41)$$

$$\frac{D^w \rho_w}{Dt} + \rho_w \operatorname{div} \bar{\mathbf{v}}^w = \rho_w e^w(\rho) \quad (4.42)$$

Finally:

$$\rho_w e^w(\rho) = -\dot{m} \quad (4.43)$$

is the quantity of water per unit time and volume, lost through evaporation.

Gaseous phases: dry air and vapour

The gaseous phase here is a multi-component material, composed of two different species: dry air and vapour. These species are miscible. We first write the mass balance equations for both species.

Their microscopic mass balance equations are again given by equation (4.36) if we neglect net production of mass of each species, due to chemical reactions with the other species (Hassanizadeh 1986).

The macroscopic mass balance equation for dry air is given by equation (4.37) with appropriate super/subscripts and with exchange term zero. We introduce intrinsic phase averaged densities and use super/subscript ga to indicate dry air. Because the two species, dry air and vapour, are miscible, they have the same volume fraction nS_g :

$$\frac{\partial}{\partial t} (n S_g \rho^{ga}) + \operatorname{div} (n S_g \rho^{ga} \bar{\mathbf{v}}^{ga}) = 0 \quad (4.44)$$

Similarly we write for vapour, using super/subscript:

$$\frac{\partial}{\partial t} (n S_g \rho^{gw}) + \operatorname{div} (n S_g \rho^{gw} \bar{\mathbf{v}}^{gw}) = n S_g \rho^{gw} e^{gw}(\rho) = \dot{m} \quad (4.45)$$

We now derive the mass balance equation for the whole gaseous phase. This is obtained by summing the macroscopic balance equations of the two species and using appropriate definitions for bulk properties of the gaseous phase (Hassanizadeh 1986) :

$$\frac{\partial}{\partial t} (n S_g \rho^g) + \operatorname{div} (n S_g \rho^g \bar{\mathbf{v}}^g) = \dot{m} \quad (4.46)$$

with

$$\rho^g = \rho^{ga} + \rho^{gw} \quad (4.47)$$

and

$$\bar{\mathbf{v}}^g = \frac{1}{\rho^g} \left(\rho^{ga} \bar{\mathbf{v}}^{ga} + \rho^{gw} \bar{\mathbf{v}}^{gw} \right) = c^{ga} \bar{\mathbf{v}}^{ga} + c^{gw} \bar{\mathbf{v}}^{gw} \quad (4.48)$$

where $c^\pi = \rho^\pi / \rho^g$ is the mass fraction of component π , subject to:

$$\sum_{\pi} c^\pi = 1, \quad \pi = gw, ga \quad (4.49)$$

We introduce further the macroscopic diffusive dispersive velocity \mathbf{u}^π , $\pi = ga, gw$ defined as (Hassanizadeh 1986) :

$$\mathbf{u}^\pi = \bar{\mathbf{v}}^{\pi g} = \bar{\mathbf{v}}^\pi - \bar{\mathbf{v}}^g \quad (4.50)$$

and subject to :

$$\rho^{ga} \mathbf{u}^{ga} + \rho^{gw} \mathbf{u}^{gw} = \rho^g \sum_{\pi} c^\pi \mathbf{u}^\pi = 0 \quad (4.51)$$

Transformation of (4.46) as in the case of the mass balance equation for the solid phase yields for gas:

$$\frac{\overset{g}{D}(n S_g \rho^g)}{Dt} + n S_g \rho^g \operatorname{div} \bar{\mathbf{v}}^g = \dot{m} \quad (4.52)$$

With a procedure similar to the previous one we obtain the following form of the mass balance equation for vapour:

$$\frac{\overset{g}{D}(n S_g \rho^{gw})}{Dt} + \operatorname{div}(n S_g \rho^{gw} \mathbf{u}^{gw}) + n S_g \rho^{gw} \operatorname{div} \bar{\mathbf{v}}^g = \dot{m} \quad (4.53)$$

We introduce now the diffusive-dispersive mass flux of component gw as (Eringen & Suhubi 1964) :

$$\mathbf{J}_g^{gw} = n S_g \rho^{gw} \mathbf{u}^{gw} \quad (4.54)$$

and now we can write:

$$\frac{D}{Dt} \left(n S_g \rho^{gw} \right) + \text{div } \mathbf{J}_g^{gw} + n S_g \rho^{gw} \text{div } \bar{\mathbf{v}}^s = \dot{m} \quad (4.55)$$

4.3.3 Linear momentum balance equation

The linear momentum balance equation for the solid phase is as following:

$$\text{div } \mathbf{t}^s + \rho_s (\bar{\mathbf{g}}^s - \bar{\mathbf{a}}^s) + \rho_s \hat{\mathbf{t}}^s = \mathbf{0} \quad (4.56)$$

For the liquid phase:

$$\text{div } \mathbf{t}^\pi + \rho_\pi (\bar{\mathbf{g}}^\pi - \bar{\mathbf{a}}^\pi) + \rho_\pi [\mathbf{e}^\pi (\rho \dot{\mathbf{r}}) + \hat{\mathbf{t}}^\pi] = \mathbf{0} \quad (4.57)$$

where $\bar{\mathbf{g}}^\pi = \frac{1}{\rho_\pi} \int_{dv} \rho \mathbf{g} \gamma^\pi dv_m$ is the external momentum supply, which is assumed to be related

to gravitational effects, $\bar{\mathbf{a}}^\pi = \dot{\bar{\mathbf{v}}}^\pi = \frac{\partial \bar{\mathbf{v}}^\pi}{\partial t} + \text{grad } \bar{\mathbf{v}}^\pi \cdot \bar{\mathbf{v}}^\pi$, is the π phase acceleration and the term

$\mathbf{I}^\pi = \hat{\mathbf{t}}^\pi = \frac{1}{\rho_\pi} \sum_{\alpha \neq \pi}^k \int_{da^{\pi\alpha}} \mathbf{t}_m \cdot \mathbf{n}^{\pi\alpha} da_m$ accounts for the exchange of momentum due to mechanical

interaction of π phase with the other α phases.

4.3.4 Angular momentum balance equation

As indicated in section 4.3, all phases of the semi-saturated porous medium are considered microscopically non-polar. The following microscopic variables are necessary for the balance equation (4.10) when angular momentum balance is considered:

$$\begin{aligned} \boldsymbol{\psi} &= \mathbf{r} \times \dot{\mathbf{r}} \\ \mathbf{i} &= \mathbf{r} \times \mathbf{t}_m \\ \mathbf{b} &= \mathbf{r} \times \mathbf{g} \\ \mathbf{G} &= \mathbf{0} \end{aligned} \quad (4.58)$$

Following a procedure similar to the earlier balance equation, or with an appropriate method chosen for the development of the average angular momentum equation (de Boer et al. 1991) and (Hassanizadeh & Gray 1979b), that for non-polar media, also at macroscopic level, it can be shown that the partial stress tensor is symmetric:

$$\mathbf{t}^\pi = (\mathbf{t}^\pi)^T \quad (4.59)$$

and that the sum of the coupling vectors of angular momentum between the phases vanishes.

4.3.5 Balance of energy equation

For the energy balance, the following components must be taken into account in the generic microscopic balance equation (4.12):

$$\begin{aligned} \psi &= E + \frac{1}{2} \dot{\mathbf{r}} \cdot \dot{\mathbf{r}} \\ \mathbf{i} &= \mathbf{t}_m \dot{\mathbf{r}} - \mathbf{q} \\ \mathbf{b} &= \mathbf{g} \cdot \dot{\mathbf{r}} + h \\ G &= 0 \end{aligned} \quad (4.60)$$

where $E(\mathbf{r}, t)$ is the specific intrinsic energy, $\mathbf{q}(\mathbf{r}, t)$ is the heat flux vector and $h(\mathbf{r}, t)$ is the intrinsic heat source.

The energy balance equation can be written as follows:

$$\rho_\pi \frac{D \bar{E}^\pi}{Dt} = \mathbf{t}^\pi : \mathbf{D}^\pi + \rho_\pi h^\pi - \text{div} \tilde{\mathbf{q}}^\pi + \rho_\pi R^\pi \quad (4.61)$$

where $\rho_\pi R^\pi = \rho_\pi \left[e^\pi(\rho \hat{E}) - e^\pi(\rho) \bar{E}^\pi + Q^\pi \right]$.

The equilibrium between all the phases can be written:

$$\sum_\pi \rho_\pi \left[e^\pi(\rho \hat{E}) + e^\pi(\rho \tilde{\mathbf{r}}) \cdot \bar{\mathbf{v}}^\pi + \frac{1}{2} e^\pi(\rho) \bar{\mathbf{v}}^\pi \cdot \bar{\mathbf{v}}^\pi + \hat{\mathbf{t}}^\pi \cdot \bar{\mathbf{v}}^\pi + Q^\pi \right] = 0 \quad (4.62)$$

and physically means that the total balance of energy exchange between all the phases is zero.

4.3.6 Entropy inequality

Exploitation of entropy inequality is a tool for developing constitutive equations in a systematic manner, leading to a consistent thermodynamic description of the material behaviour at macroscale. The use of entropy inequality further assures that the second law of thermodynamics is not violated. The procedure was proposed by (Coleman & Noll, 1963). It is, for instance, exploited in (Sampaio & Williams 1979), and by (Gray & M. Hassanizadeh

1991) for the development of constitutive equations for unsaturated flow in dry or partially saturated soil, including interfacial phenomena.

The variables in the microscopic balance equation (4.12) are now:

$$\begin{aligned}\psi &= \lambda \\ \mathbf{i} &= \Phi \\ b &= s \\ G &= \varphi\end{aligned}\tag{4.63}$$

where λ is the specific entropy Φ the entropy flux vector and s an intrinsic entropy source.

The net production φ denotes an increase of entropy. The balance equation then becomes :

$$\frac{\partial}{\partial t}(\rho\lambda) + \text{div}(\rho\lambda \mathbf{r}) - \text{div}\Phi - \rho s = \rho\varphi\tag{4.64}$$

Starting from this last equation, λ^π the averaged specific entropy of constituent π , and the entropy supply due to mass exchange are determined in order to obtain the entropy inequality for the mixture:

$$\sum_{\pi} \left[\rho_{\pi} \frac{D \bar{\lambda}^{\pi}}{Dt} + \rho_{\pi} e^{\pi}(\rho) \bar{\lambda}^{\pi} + \text{div} \left(\frac{1}{\theta^{\pi}} \mathbf{q}^{\pi} \right) - \frac{1}{\theta^{\pi}} \rho_{\pi} h^{\pi} \right] \geq 0\tag{4.65}$$

where $\bar{\lambda}^{\pi} = \frac{1}{\rho_{\pi}} \int_{dv} \rho \lambda^{\pi} dv_m$, \mathbf{q}^{π} is the flux of entropy for unit of temperature and $\frac{h^{\pi}}{\theta^{\pi}}$ is

the source of entropy for each phase.

Again, this corresponds to the form used in the mixture theory as shown in (de Boer et al. 1991). Before further transformations of the macroscopic balance equations are made, the constitutive equations for the constituents are introduced.

4.4 Constitutive equations

To complete the description of the mechanical behaviour, it is needed to specify the constitutive equations. The balance equations developed in the previous sections allow for the introduction of quite elaborate constitutive theories, especially if the balance equations presented in the previous sections for the bulk material are extended to the interfaces, as done by Gray, and Hassanizadeh in (Gray & M. Hassanizadeh 1991) and (Gray & S. M.

Hassanizadeh 1991) for the aspects concerning multiphase flow. For the solid phase, second-grade material theories are also possible, where the gradients of relevant thermodynamic properties, such as densities, are considered as independent variables (Ehlers 1989). However, since this work is application oriented, i.e. we aim for the quantitative solution of real engineering problems, a different choice is made.

Following (Lewis & Schrefler 1998), the constitutive models which are selected are based on quantities currently measurable in laboratory or field experiments, and which have been extensively validated both with reference to known exact solutions and to experiments. Many of these constitutive models correspond to linearization of more complex arguments.

We deal first with the properties of the fluid phases, and only briefly mention the solid phase here, because this is the main aspect of this thesis and then this will be seen later.

4.4.1 Stress tensor in the fluid phases

By applying entropy inequality for the bulk material (Hassanizadeh & Gray 1980), (Gray & M. Hassanizadeh 1991), it can be shown that the stress tensor in the fluid phases, is :

$$\mathbf{t}^\pi = -\eta^\pi p^\pi \mathbf{I} \quad (4.66)$$

where \mathbf{I} is the identity tensor p^π is the macroscopic pressure of the π phase.

The volume fraction, η^π , appears in equation (4.66) because \mathbf{t}^π is the force exerted on the fluid-phase per unit area of multiphase medium. It should be noted that the stress vector in the fluid phase does not have any dissipating part. The macroscopic effects of deviatoric stress components will be accounted for in linear momentum balance equations through momentum exchange terms.

4.4.2 Gaseous mixture of dry air and water vapour

The moist air in the pore system is usually assumed to be a perfect mixture of two ideal gases, i.e. dry air and water vapour. Hence the ideal gas law, relating the partial pressure, $p_{g\pi}$, of species π , the mass concentration, $\rho_{g\pi}$, of species π in the gas phase and the absolute temperature, θ , is used.

The equations of state of a perfect gas, applied to dry air (ga), vapour (gw) and moist air (g) are:

$$\begin{aligned} p^{ga} &= \rho^{ga} \theta R / M_a \\ p^{gw} &= \rho^{gw} \theta R / M_w \end{aligned} \quad (4.67)$$

$$\begin{aligned} \rho^g &= \rho^{ga} + \rho^{gw} \\ p^g &= p^{ga} + p^{gw} \\ M_g &= \left(\frac{\rho^{gw}}{\rho^g} \frac{1}{M_w} + \frac{\rho^{ga}}{\rho^g} \frac{1}{M_a} \right)^{-1} \end{aligned} \quad (4.68)$$

where M_π is the molar mass of constituent π and R is the universal gas constant. The second of equations (4.68) expresses Dalton's law (Moran & Shapiro 1993). It is reminded that for the averaging process dry air, vapour and moist air occupy the same volume fraction, nS_g .

4.4.3 Sorption equilibrium

If an oven-dry porous medium is exposed to moist air, the weight of such solid increases because the moisture is adsorbed on the inner surfaces of the pores starting with the finest ones. In the cases of interest here, the water is usually present as a condensed liquid that, because of the surface tension, is separated from its vapour by a concave meniscus (capillary water). There is then a relationship between the relative humidity, the water content (saturation) and the capillary pressure in the pores.

The capillary pressure is defined as the pressure difference between the gas phase and the liquid phase, by the capillary pressure equation:

$$p^c = p^g - p^w \quad (4.69)$$

where p^w is the pressure of the liquid-phase (water).

In (Gray & S. M. Hassanizadeh 1991), it is shown that $p^c = p^g - p^w$ is not just a definition, but a derived relationship between two independent quantities p^c and $p^g - p^w$, at equilibrium.

For the relationship between the relative humidity (R.H.) and the capillary pressure in the pores, Kelvin-Laplace law is assumed to be valid:

$$R.H. = \frac{p^{gw}}{p^{gws}} = \exp \left(\frac{p^c M_w}{\rho^w R} \right) \quad (4.70)$$

The water vapour saturation pressure, p^{gws} , which is a function of the temperature only, can be obtained from the Clausius-Clapeyron equation indicated below, or from empirical formulas such as the one proposed by Hyland and Wexler (Organisation ASHRAE 1993).

Assuming zero contact angle between the liquid phase and the solid phase, as is usually accepted for pore water, the capillary pressure can be obtained through the Laplace equation from the pore radius, r :

$$p^c = \frac{2\sigma}{r} \quad (4.71)$$

where σ is the surface tension.

These considerations are applicable if the water is present in the pores, as a condensed liquid (capillary region). When, instead, the water is present as one or more molecular layers adsorbed on the surface of a solid because of the Van der Waals and/or other interactions, the capillary pressure no longer has an obvious meaning, even if it can be retained, referring to the broader concept of water potential or moisture stress. In such a case, a direct relationship between the water content and the relative humidity is assumed to hold such as the BET equation (Organisation ASHRAE 1993).

4.4.4 Clausius-Clapeyron equation

As indicated above, this equation links the water vapour saturation pressure with temperature :

$$p^{gws}(\theta) = p^{gws0} \exp \left[-\frac{M_w \Delta H_{gw}}{R} \left(\frac{1}{\theta} - \frac{1}{\theta_0} \right) \right] \quad (4.72)$$

where θ_0 is a reference temperature, p^{gws} is the water vapour saturation pressure at θ , p^{gws0} is the water vapour saturation pressure at θ_0 , ΔH_{gw} is the specific enthalpy of evaporation. The equation is obtained from the second law of thermodynamics and is valid in the vicinity of θ_0 .

In the following, we denote T as the temperature difference above a reference value such that $T = \theta - \theta_0$.

4.4.5 Pore size distribution

As it turns out from equations (4.70) and (4.71), the problem is to know the pore size distribution of the considered porous medium, to relate the size of the largest pore filled (from which the capillary pressure depends) with the actual water content. This relationship is obtained through experimental tests, usually centrifuge tests, sorption isotherm measurements or mercury porosimetry.

The question is somewhat complex, because both the Laplace equation (4.71) and the Kelvin equation (4.70) are obtained from a force equilibrium, evaluated in a cylindrical capillary tube, and the porous medium is considered as a bundle of capillary tubes that do not intersect. The real porous media are more correctly represented as three-dimensional networks of sites (or bodies) interconnected by narrower bonds (or throats) and then intrusion, extrusion, adsorption and desorption are subjected to hysteresis. In this case, the actual value of capillary pressure can be only interpreted as a measurable quantity describing complex adsorbed water-solid matrix interaction. The determination of pore size distribution from sorption isotherms, results of centrifuge tests and mercury porosimetry should then be done following the percolation theory approach, (Bomberg & Shirtcliffe 1978).

The Rayleigh distribution or the log-normal distributions are often a good estimation of the pore size and often such distribution can be bi-modal or multi-modal.

For soils, we need the Kelvin-Laplace equation (4.70), the Clausius-Clapeyron equation (4.72) and the capillary pressure relationship:

$$S_{\pi} = S_{\pi}(p^c, T) \quad (4.73)$$

which is directly obtained in laboratory.

In later chapters, where the constitutive models are introduced, will show different relationships for the pore size distribution and one of them gives:

$$S_{\pi} = S_{\pi}(p^c, T, \varepsilon_v) \quad (4.74)$$

where ε_v is the volumetric strain.

4.4.6 Equation of state for water

From the mass conservation in differential form:

$$\frac{D^w (\rho^w V^w)}{Dt} = 0 \quad (4.75)$$

It can be possible to obtain:

$$\frac{1}{\rho^{wo}} \frac{D^w \rho^w}{Dt} = \frac{1}{K_w} \frac{D^w p^w}{Dt} - \beta_w \frac{DT}{Dt} \quad (4.76)$$

where β_w is the thermal expansion coefficient, $K_w = \frac{1}{C_w}$ the bulk modulus of water and with C_w the compressibility coefficient and where :

$$\frac{1}{\rho^{wo}} \frac{\partial \rho^w}{\partial p^w} = \frac{1}{K_w} \quad (4.77)$$

$$\frac{1}{\rho^{wo}} \frac{\partial \rho^w}{\partial T} = -\beta_w \quad (4.78)$$

4.4.7 Darcy's law

Darcy's law, generalized to allow for relative permeability:

$$\eta^\pi \bar{\mathbf{v}}^{\pi s} = \frac{k^{r\pi} \mathbf{k}}{\mu^\pi} \left(-grad p^\pi + \rho^\pi \mathbf{g} \right) \quad (4.79)$$

is assumed valid for the transport of both water and gas in slow phenomena; \mathbf{k} is the permeability of the medium, μ is the dynamic viscosity, $k^{r\pi}$ the relative permeability, a dimensionless parameter varying from zero to one.

For each particular porous medium, the relations $k^{r\pi}(S_w)$ are either predicted by models based on some more or less realistic capillary assumption or experimentally determined in laboratory as well as field conditions. For typical curves of relative permeabilities to water and air the reader is referred to Corey (Corey 1957).

The relative permeability goes to zero before the saturation reaches the value zero. The water saturation at which the relative permeability goes to zero is termed the residual water saturation or displacement residual water saturation.

Relationships used in the following are e.g. those by Brooks and Corey (Brooks & Corey 1966) :

$$k^{rw} = S_e^{\frac{(2+3\lambda)}{\lambda}} \quad (4.80)$$

$$p^c = \frac{P^b}{S_e^{\frac{1}{\lambda}}} \quad (4.81)$$

where $S_e = \frac{S_w - S_{wc}}{1 - S_{wc}}$ is the effective saturation, S_{wc} is the irreducible saturation, λ the pore size distribution index, p^b the bubbling pressure.

4.4.8 Fick's law

Diffusive-dispersive mass flux is governed by Fick's law:

$$\mathbf{J}_\alpha^\pi = -\rho^\alpha \mathbf{D}_\alpha^\pi \text{grad} \left(\frac{\rho^\pi}{\rho^\alpha} \right) \quad (4.82)$$

where \mathbf{D}_α^π is the effective dispersion tensor, π is the diffusing phase, α is the phase in which diffusion takes place ($\alpha=w, g$). \mathbf{D}_α^π is a function of the tortuosity factor, which accounts for the tortuous nature of the pathway in soil; because of mechanical dispersion, \mathbf{D}_α^π is also correlated with seepage velocity.

For dry air and water vapour (binary system) we have in particular, by the first of equations (4.68) and from the relation $\rho^g = \rho^{ga} + \rho^{gw}$:

$$\begin{aligned}
\mathbf{J}_g^{ga} &= -\rho^g \frac{M_a M_w}{M_g^2} \mathbf{D}_g \text{grad} \left(\frac{p^{ga}}{p^g} \right) = \\
&= \rho^g \frac{M_a M_w}{M_g^2} \mathbf{D}_g \text{grad} \left(\frac{p^{gw}}{p^g} \right) = -\mathbf{J}_g^{gw}
\end{aligned} \tag{4.83}$$

It is worthwhile to emphasise that gas diffusion can take place even in the absence of a gas pressure gradient, i.e. when its mass weighted velocity $\bar{\mathbf{v}}^g$ is zero.

4.4.9 Stress tensor in the solid phase and total stress

From the entropy inequality written in (Gray & M. Hassanizadeh 1991) for unsaturated flow, including interfacial phenomena, it can be shown that the stress vector in the solid phase is :

$$\mathbf{t}^s = (1-n) (\mathbf{t}_e^s - \mathbf{I} p^s) \tag{4.84}$$

the pressure in the solid phase is :

$$p^s = p^w S_w + p^g S_g \tag{4.85}$$

and

$$\boldsymbol{\sigma}' = (1-n) \mathbf{t}_e^s \tag{4.86}$$

is the effective stress tensor.

Introduction of (4.85) into (4.84) yields :

$$\mathbf{t}^s = (1-n) \left[\mathbf{t}_e^s - \mathbf{I} (S_w p^w + S_g p^g) \right] \tag{4.87}$$

The volume fraction (1-n) indicates that \mathbf{t}^s is the stress exerted on the solid phase per unit area of a multiphase medium.

The sum of (4.87) and of (4.66) written for gas and for water gives the total stress, $\boldsymbol{\sigma}$, acting on a unit area of a multiphase medium:

$$\begin{aligned}
\boldsymbol{\sigma} = \mathbf{t}^s + \mathbf{t}^w + \mathbf{t}^g &= (1-n) \left[\mathbf{t}_e^s - \mathbf{I} (S_w p^w + S_g p^g) \right] \\
-S_w n \mathbf{I} p^w - S_g n \mathbf{I} p^g &= (1-n) \mathbf{t}_e^s - \mathbf{I} (S_w p^w + S_g p^g)
\end{aligned} \tag{4.88}$$

This can be put in the usual soil mechanics form as:

$$\boldsymbol{\sigma} = \boldsymbol{\sigma}' - \mathbf{I}(S_w p^w + S_g p^g) \quad (4.89)$$

or

$$\boldsymbol{\sigma}' = \boldsymbol{\sigma} + \mathbf{I}(S_w p^w + S_g p^g) \quad (4.90)$$

From this last equation, it follows that the relationship between effective stress and total stress, in partially saturated porous media, is no longer independent of the soil type because of the saturations, while in fully saturated soils, where $S_g=0$ and $S_w=1$, the effective stress principle is unique for all soil types.

An expression of the effective stress principle was obtained by (Bishop & Blight 1963) using a phenomenological approach.

The effective stress is responsible for all major deformations in the skeleton and is linked to the strain rate tensor, \mathbf{D}^s , by means of a constitutive relationship:

$$\frac{D\boldsymbol{\sigma}'}{Dt} = \mathbf{D}_T [(\mathbf{D}^s - \mathbf{D}_0^s)] \quad (4.91)$$

where

$$\mathbf{D}_T = \mathbf{D}_T(\mathbf{D}^s, \boldsymbol{\sigma}', p^c, T) \quad (4.92)$$

is a fourth order tensor and \mathbf{D}_0^s represents the increment of all other strains not directly associated with stress changes.

4.4.10 Solid density

When considering the solid phase as compressible, a relationship for the material time derivative of the solid density can be obtained from the mass conservation equation in differential form:

$$\frac{D(\rho^s V^s)}{Dt} = 0 \quad (4.93)$$

By assuming that the solid density is a function of p^s , of temperature and of the first invariant of the effective stress, and defining the Biot's constant (Biot & Willis 1957) as:

$$\alpha = 1 - \frac{K_T}{K_s} \quad (4.94)$$

we obtain:

$$\frac{1}{\rho^s} \frac{D^s \rho^s}{Dt} = \frac{1}{1-n} \left[(\alpha - n) \frac{1}{K_s} \frac{D^s p^s}{Dt} - \beta_s (\alpha - n) \frac{DT}{Dt} - (1-\alpha) \operatorname{div} \bar{\mathbf{v}}^s \right] \quad (4.95)$$

where K_T is the bulk modulus of the skeleton, K_s is the bulk modulus of the of the grain material, β_s is the thermal expansion coefficient for the solid.

In soils volumetric strain is relatively insignificant and can be ignored ($\alpha=1$), but it is important in rock mechanics and in concrete, where the compressibility of the solid phase is comparable to that of the skeleton.

4.4.11 Fourier's Law

A constitutive assumption for the heat flux is the generalized Fourier's Law:

$$\tilde{\mathbf{q}} = -\chi_{eff} \operatorname{grad} T \quad (4.96)$$

where χ_{eff} is the effective thermal conductivity tensor and $\tilde{\mathbf{q}}$ is the heat flux of the multiphase medium.

For isotropic media the generalized Fourier's Law becomes the well-known empirical Fourier's Law :

$$\mathbf{q} = -\chi_{eff} \operatorname{grad} T \quad (4.97)$$

where χ_{eff} is the effective thermal conductivity.

The effective thermal conductivity can be predicted theoretically as well as determined experimentally.

For porous building materials, for instance, the following linear relationship may be used, which represents with sufficient accuracy the data by (Bomberg & Shirtliffe 1978) :

$$\chi_{eff} = \chi_{dry} \left(1 + 4 \frac{n S^w \rho^w}{(1-n) \rho^s} \right) \quad (4.98)$$

4.5 General field equations

The macroscopic balance laws are now transformed, and the constitutive equations introduced, to obtain the general field equations, according to (Lewis & Schrefler 1998), which will be used in the subsequent sections. The averaging symbol, overbar, will be omitted in the remainder of this thesis, because all quantities belong to the macroscopic situations.

4.5.1 Mass balance equation

Solid phase

The macroscopic mass balance equation for the solid phase (4.40), divided by ρ^s is :

$$\frac{1-n}{\rho^s} \frac{D^s \rho^s}{Dt} - \frac{Dn}{Dt} + (1-n) \operatorname{div} \mathbf{v}^s = 0 \quad (4.99)$$

Liquid phase

Upon introduction of the relative velocity (4.29) and the material time derivative with respect to the moving solid (4.26) equation (4.42) for liquid water becomes:

$$\frac{D^s \rho_w}{Dt} + \mathbf{v}^{ws} \cdot \operatorname{grad} \rho_w + \rho_w \operatorname{div} (\mathbf{v}^s + \mathbf{v}^{ws}) = -\dot{m} \quad (4.100)$$

Introduction of intrinsic phase averaged densities with the appropriate volume fractions, use of vector identity written for water and division by $S_w \rho^w$ allows us to transform last equation into:

$$\frac{D^s n}{Dt} + \frac{n}{\rho^w} \frac{D^s \rho^w}{Dt} + \frac{n}{S_w} \frac{D^s S_w}{Dt} + \frac{1}{S_w \rho^w} \operatorname{div} (n S_w \rho^w \mathbf{v}^{ws}) + n \operatorname{div} \mathbf{v}^s = -\frac{\dot{m}}{S_w \rho^w} \quad (4.101)$$

Summation with (4.99), to eliminate $\frac{Dn}{Dt}$ gives:

$$\frac{(1-n)}{\rho^s} \frac{D^s \rho^s}{Dt} + \operatorname{div} \mathbf{v}^s + \frac{n}{\rho^w} \frac{D^s \rho^w}{Dt} + \frac{n}{S_w} \frac{D^s S_w}{Dt} + \frac{1}{S_w \rho^w} \operatorname{div} (n S_w \rho^w \mathbf{v}^{ws}) = -\frac{1}{S_w \rho^w} \dot{m} \quad (4.102)$$

Introduction of (4.76) and (4.95) for the material derivatives of the solid and water densities and of (4.85) gives :

$$\begin{aligned} & \frac{\alpha-n}{K_s} \frac{D}{Dt} (S^w p^w + S^g p^g) - \beta_s (\alpha-n) \frac{D T}{Dt} + \alpha \operatorname{div} \mathbf{v}^s \\ & + n \left(\frac{1}{K_w} \frac{D p^w}{Dt} - \beta_w \frac{D T}{Dt} \right) + \frac{n}{S_w} \frac{D S_w}{Dt} + \frac{1}{S_w \rho^w} \operatorname{div} (n S_w \rho^w \mathbf{v}^{ws}) \\ & = - \frac{1}{S_w \rho^w} \dot{m} \end{aligned} \quad (4.103)$$

where p^w , p^g and T are independent variables.

For incompressible grains ($\alpha = 1$ and $\frac{1}{K_s} = 0$) this equation may be simplified as follows:

$$\frac{n S_w}{K_w} \frac{D p^w}{Dt} + S_w \operatorname{div} \mathbf{v}^s - \beta_{sw} \frac{D T}{Dt} + n \frac{D S_w}{Dt} + \frac{1}{\rho^w} \operatorname{div} (n S_w \rho^w \mathbf{v}^{ws}) = - \frac{\dot{m}}{\rho^w} \quad (4.104)$$

with $\beta_{sw} = S_w [(\alpha-n)\beta_s + n\beta_w]$.

Gaseous phase

The mass balance equation for gas as a mixture of dry air and vapour is dealt with next. In the same mode of the liquid phase, starting from (4.52) we obtain:

$$\begin{aligned} & \frac{\alpha-n}{K_s} S_w S_g \frac{D p^w}{Dt} + \frac{\alpha-n}{K_s} S_g^2 \frac{D p^g}{Dt} + \alpha S_g \operatorname{div} \mathbf{v}^s + \frac{n S_g}{\rho^g} \frac{D \left[\frac{1}{\theta R} (p^{ga} M_a + p^{gw} M_w) \right]}{Dt} + \\ & - \left(\frac{\alpha-n}{K_s} p^c S_g + n \right) \frac{D S_w}{Dt} + \frac{1}{\rho^g} \operatorname{div} (n S_g \rho^g \mathbf{v}^{gs}) - \beta_s (\alpha-n) S_g \frac{D T}{Dt} = \frac{1}{\rho^g} \dot{m} \end{aligned} \quad (4.105)$$

where p^w , p^g and T are independent variables.

For incompressible grains ($\alpha = 1$ and $\frac{1}{K_s} = 0$) this equation may be simplified as follows:

$$\begin{aligned}
& -n \frac{D S_w}{Dt} - \beta_s (1-n) S_g \frac{DT}{Dt} + S_g \operatorname{div} \mathbf{v}^s + \frac{n S_g}{\rho^g} \frac{D}{Dt} \left[\frac{1}{\theta R} (p^{ga} M_a + p^{gw} M_w) \right] \\
& + \frac{1}{\rho^g} \operatorname{div} (n S_g \rho^g \mathbf{v}^{gs}) = \frac{\dot{m}}{\rho^g}
\end{aligned} \quad (4.106)$$

For heat transfer analysis, in partially saturated porous media, it is more convenient to consider the mass balance equation for dry air separately from that of vapour (Baggio et al. 1993), (Gawin et al. 1995) and to sum the mass balance equations for both water species, liquid water and water vapour. In this way, the mass rate of water evaporation, \dot{m} , disappears from the mass balance equations. An evolution equation needed and this will be given by the energy balance equation. Note that, in this way, no constitutive model for the mass rate of water evaporation is needed.

Gaseous phase: dry air

The mass balance equation for dry air is transformed in the following equation:

$$\frac{D(n S_g \rho^{ga})}{Dt} + \operatorname{div} \mathbf{J}_g^{ga} + n S_g \rho^{ga} \operatorname{div} \mathbf{v}^g = 0 \quad (4.107)$$

The resulting equation is divided by $\rho^{ga} S_g$ and summed with (4.99) we obtained:

$$\begin{aligned}
& \frac{\alpha - n}{K_s} S_w S_g \frac{D p^w}{Dt} + \frac{\alpha - n}{K_s} S_g^2 \frac{D p^{ga}}{Dt} + \alpha S_g \operatorname{div} \mathbf{v}^s + \frac{n S_g}{\rho^{ga}} \frac{D \rho^{ga}}{Dt} + \frac{1}{\rho^{ga}} \operatorname{div} \mathbf{J}_g^{ga} + \\
& - \left(\frac{\alpha - n}{K_s} p^c S_g + n \right) \frac{D S_w}{Dt} + \frac{1}{\rho^{ga}} \operatorname{div} (n S_g \rho^{ga} \mathbf{v}^{gs}) - \beta_s (\alpha - n) S_g \frac{DT}{Dt} = 0
\end{aligned} \quad (4.108)$$

For incompressible solid grains this equation is simplified as:

$$\begin{aligned}
& -n \frac{D S_w}{Dt} - \beta_s (1-n) S_g \frac{DT}{Dt} + S_g \operatorname{div} \mathbf{v}^s + \frac{n S_g}{\rho^g} \frac{D}{Dt} \left[\frac{1}{\theta R} (p^{ga} M_a + p^{gw} M_w) \right] \\
& + \frac{1}{\rho^g} \operatorname{div} (n S_g \rho^g \mathbf{v}^{gs}) = \frac{\dot{m}}{\rho^g}
\end{aligned} \quad (4.109)$$

Introducing now the constitutive equations for ρ^{ga} and for \mathbf{J}_g^{ga} to obtain:

$$\begin{aligned}
& -n \frac{D S_w^s}{Dt} - \beta_s (1-n) S_g \frac{DT}{Dt} + S_g \operatorname{div} \mathbf{v}^s + \frac{S_g n}{\rho^{ga}} \frac{D}{Dt} \left(\frac{M_a}{\theta R} p^{ga} \right) \\
& - \frac{1}{\rho^{ga}} \operatorname{div} \left[\rho^g \frac{M_a M_w}{M_g^2} D_g \operatorname{grad} \left(\frac{p^{ga}}{p^g} \right) \right] + \frac{1}{\rho^{ga}} \operatorname{div} (n S_g \rho^{ga} \mathbf{v}^{gs}) = 0
\end{aligned} \tag{4.110}$$

Gaseous phase:vapour

The way to derive the mass balance equation for vapour is identical to that of dry air and results, for the case of incompressible solid grains, in:

$$\begin{aligned}
& -n \frac{D S_w^s}{Dt} - \beta_s (1-n) S_g \frac{DT}{Dt} + S_g \operatorname{div} \mathbf{v}^s + \frac{S_g n}{\rho^{gw}} \frac{D}{Dt} \left(\frac{M_w}{\theta R} p^{gw} \right) \\
& - \frac{1}{\rho^{gw}} \operatorname{div} \left[\rho^g \frac{M_a M_w}{M_g^2} D_g \operatorname{grad} \left(\frac{p^{gw}}{p^g} \right) \right] + \frac{1}{\rho^{gw}} \operatorname{div} (n S_g \rho^{gw} \mathbf{v}^{gs}) = \frac{\dot{m}}{\rho^{gw}}
\end{aligned} \tag{4.111}$$

This equation is now multiplied by ρ^{gw} and added to the mass balance equation of liquid water, in turn multiplied by ρ^w . This sum gives the mass balance equation for the water species, liquid and vapour, without mass rate of water evaporation as:

$$\begin{aligned}
& n(\rho^w - \rho^{gw}) \frac{D S_w^s}{Dt} - \beta_{swg} \frac{DT}{Dt} + (\rho^{gw} S_g + \rho^w S_w) \operatorname{div} \mathbf{v}^s \\
& + \frac{n \rho^w S_w}{K_w} \frac{D p^w}{Dt} + S_g n \frac{D}{Dt} \left(\frac{M_w}{\theta R} p^{gw} \right) \\
& - \operatorname{div} \left[\rho^g \frac{M_a M_w}{M_g^2} D_g \operatorname{grad} \left(\frac{p^{gw}}{p^g} \right) \right] \\
& + \operatorname{div} (n S_g \rho^{gw} \mathbf{v}^{gs}) + \operatorname{div} (n S_w \rho^w \mathbf{v}^{ws}) = 0
\end{aligned} \tag{4.112}$$

where $\beta_{swg} = \beta_s (1-n) (S_g \rho^{gw} + \rho^w S_w) + n \beta_w \rho^w S_w$.

In these equations Darcy's law for the fluid velocities relative to the solid has still to be introduced. This law was introduced in section 4.4.7 and will be derived again in its generalized form in the next section from the linear momentum balance equations.

4.5.2 Linear momentum balance equation

Fluids

A more suitable form for the linear momentum balance equation for the fluid-phases is now obtained by introducing kinematic equations and constitutive relationships.

Equations (4.31) and (4.32) allow us to write for acceleration, \mathbf{a}^π :

$$\mathbf{a}^\pi = \mathbf{a}^s + \mathbf{a}^{\pi s} + \mathbf{v}^{\pi s} \cdot \text{grad } \mathbf{v}^\pi \quad (4.113)$$

where $\mathbf{a}^{\pi s}$ is the relative acceleration.

Introduction in (4.57) of (4.113), the momentum exchange term and of the intrinsic phase averaged density yields:

$$\begin{aligned} & -\eta^\pi \rho^\pi \left(\mathbf{a}^s + \mathbf{a}^{\pi s} + \mathbf{v}^{\pi s} \cdot \text{grad } \mathbf{v}^\pi \right) - \text{div} \left(\eta^\pi p^\pi \mathbf{I} \right) \\ & + \eta^\pi p^\pi e^\pi (\rho \dot{\mathbf{r}}) + \eta^\pi p^\pi \mathbf{g} - \mathbf{R}^\pi \eta^\pi \mathbf{v}^{\pi s} = 0 \end{aligned} \quad (4.114)$$

By neglecting the term dependent on the gradient of the fluid velocity, the effects of phase change and by applying a vector identity, for the divergence of the stress tensor in the fluid-phase, we obtain the relative velocity of the fluid as :

$$\eta^\pi \mathbf{v}^{\pi s} = \left(\mathbf{R}^\pi \right)^{-1} \eta^\pi \left[-\text{grad } p^\pi + \rho^\pi \left(\mathbf{g} - \mathbf{a}^s - \mathbf{a}^{\pi s} \right) \right] \quad (4.115)$$

$$\eta^\pi \mathbf{v}^{\pi s} = \frac{\mathbf{k} k^{r\pi}}{\mu} \left[-\text{grad } p^\pi + \rho^\pi \left(\mathbf{g} - \mathbf{a}^s - \mathbf{a}^{\pi s} \right) \right] \quad (4.116)$$

Finally, neglecting the soil acceleration and the relative acceleration terms, it yields Darcy's law in the form (4.79) :

$$\eta^\pi \bar{\mathbf{v}}^{\pi s} = \frac{k^{r\pi} \mathbf{k}}{\mu^\pi} \left(-\text{grad } p^\pi + \rho^\pi \mathbf{g} \right) \quad (4.117)$$

Due to the simplifications introduced, this law is valid as a first approximation for slow flow of a macroscopically inviscid fluid through a porous medium with incompressible grains.

Solid phase

Taking into account equations (4.84), (4.85), (4.86), the linear momentum balance equation for the solid-phase becomes:

$$\begin{aligned} \operatorname{div} \left[\boldsymbol{\sigma}' - \mathbf{I} (1-n) (S_w \rho^w + S_g \rho^g) \right] + (1-n) \rho^s \mathbf{g} - (1-n) \rho^s \mathbf{a}^s \\ + \mathbf{R}^w \eta^w \mathbf{v}^{ws} + \mathbf{R}^g \eta^g \mathbf{v}^{wg} = 0 \end{aligned} \quad (4.118)$$

Multiphase medium

By summing the momentum balance equations, written for water and gas-phase respectively, with that of the solid phase (4.118), by taking into account the definition of total stress, assuming continuity of stress at the fluid-solid interfaces and by introducing the averaged density of the multiphase medium:

$$\rho = (1-n) \rho^s + n S_w \rho^w + n S_g \rho^g \quad (4.119)$$

we obtain the linear momentum balance equation for the whole multiphase medium:

$$\begin{aligned} -\rho \mathbf{a}^s - n S_w \rho^w \left[\mathbf{a}^{ws} + \mathbf{v}^{ws} \cdot \operatorname{grad} \mathbf{v}^w \right] - \\ n S_g \rho^g \left[\mathbf{a}^{gs} + \mathbf{v}^{gs} \cdot \operatorname{grad} \mathbf{v}^g \right] + \operatorname{div} \boldsymbol{\sigma} + \rho \mathbf{g} = 0 \end{aligned} \quad (4.120)$$

4.5.3 Energy balance equation

The energy balance equation for the single phase is:

$$\rho_\pi C_p^\pi \frac{D\theta^\pi}{Dt} = \rho_\pi h^\pi - \operatorname{div} \tilde{\mathbf{q}}^\pi + \rho_\pi R_H^{\pi\pi} - \rho_\pi e^\pi (\rho) H^\pi \quad (4.121)$$

where $H^\pi = H^\pi(\bar{p}^\pi, \theta^\pi)$ is the specific enthalpy of the phase π and $C_p^\pi = \left(\frac{\partial H^\pi}{\partial \theta^\pi} \right)_{\bar{p}}$ is the

specific heat at constant pressure.

For the continuum multiphase, with the impose of thermodynamic equilibrium, the energy balance equation is:

$$\left(\rho C_p \right)_{\text{eff}} \frac{\partial T}{\partial t} + \left(\rho_w C_p^w \mathbf{v}^w + \rho_g C_p^g \mathbf{v}^g \right) \cdot \operatorname{grad} T - \operatorname{div} \left(\boldsymbol{\chi}_{\text{eff}} \operatorname{grad} T \right) = -\dot{m} \Delta H_{\text{vap}} \quad (4.122)$$

where

$$\begin{aligned}
 (\rho C_p)_{eff} &= \rho_s C_p^s + \rho_w C_p^w + \rho_g C_p^g \\
 \chi_{eff} &= \chi^s + \chi^w + \chi^g \\
 \Delta H_{vap} &= H^{gw} - H^w
 \end{aligned} \tag{4.123}$$

4.6 Physical approach: extended Biot's theory

The governing equations, using Biot's theory (Biot 1941b), (Biot 1941a), (Biot 1955), (Biot 1956a), (Biot 1956b), (Biot 1963) are again derived but extended to the case of non-isothermal two-phase flow in deforming porous media. This extension was made in (Schrefler et al. 1995), (Schrefler & Zhan 1993) for the case of slow phenomena. Also, inertia forces are taken into account, as was done in (Zienkiewicz et al. 1990) for the isothermal case with the air phase at atmospheric pressure.

The physical approach works directly with macroscopic variables. However, the distinction between a macroscopic and microscopic domain is not as clear as in the previous sections, because macroscopic variables are sometimes directly used in the microscopic domain (Lewis & Schrefler 1998).

For the sake of simplicity, small displacements are assumed for the solid phase. The governing equations in the form needed for finite strain analysis are those of the previous section. For all queries regarding the assumed hypotheses the interested reader is referred to the first part of this chapter.

4.6.1 The physical model

The voids of the skeleton are filled partly with water and partly with moist air (mixture of dry air and water vapour), which is referred to as gas. The degree of water saturation S_w is given as the ratio between the pore space occupied by the water and the total pore volume in a representative elementary volume element:

$$S_w = \frac{dv^w}{dv^w + dv^g} \tag{4.124}$$

In the following equations the super or subscript π refers to the generic phase, $\pi = s$ to the solid phase, $\pi = w$ to water and $\pi = g$ to gas. The volume of the R.E.V. is dv , while the partial

volumes are dv^s , dv^w and dv^g . Their sum is dv while the sum of the respective fluid volumes is $dv^T=dv^w+dv^g$. The definition of the degree of gas saturation S_g is :

$$S_g = \frac{dv^g}{dv^w + dv^g} \quad (4.125)$$

and both degrees of saturation sum to one i.e. :

$$S_w + S_g = 1 \quad (4.126)$$

The porosity n is defined as the ratio between the volume of voids and the total volume of the R.E.V. :

$$n = \frac{dv^w + dv^g}{dv} \quad (4.127)$$

As in the first part of this chapter, the stress is defined as tension positive for the solid phase, while pore pressure is defined as compressive positive for fluids. The water pressure p^w and the gas pressure p^g are related through the capillary pressure p^c :

$$p^c = p^g - p^w \quad (4.128)$$

The relation (4.128) is determined experimentally and usually shows hysteresis characteristics, which are ignored in this case. Equation (4.128) is numerically inverted to obtain:

$$S_\pi = S_\pi(p^c, T, \varepsilon_v^p) \quad (4.129)$$

The constitutive law of the solid phase is introduced through the concept of effective stress :

$$\boldsymbol{\sigma}' = \boldsymbol{\sigma} + \mathbf{I} p^s \quad (4.130)$$

which stipulates that the main characteristics of the solid phase constitutive relation can be written in terms of $\boldsymbol{\sigma}$ where $\boldsymbol{\sigma}$ is the total stress tensor, \mathbf{I} the second order unit tensor and p^s is the average pressure of both the water and air surrounding the grains. In the case of immiscible two-phase flow we need a simple averaging technique for the calculation of p^s as described in

section 4.2. Thus the modified effective stress principle may be obtained as stated previously. The effective stress resulting from equation (4.129) is also referred to as Bishop's stress:

$$\bar{\boldsymbol{\sigma}} = \frac{1}{dv} \int \boldsymbol{\sigma} dv_m = \frac{1}{dv} \left[\int_{dv^s} \boldsymbol{\sigma} dv_m + \int_{dv^f} \boldsymbol{\sigma} dv_m \right] \quad (4.131)$$

where $\bar{\boldsymbol{\sigma}}$ is the macroscopic total stress tensor.

For the fluid phases, the stress tensor is given by:

$$\boldsymbol{\sigma}^\pi = \tau^\pi - \mathbf{I} p^\pi \quad (4.132)$$

where $\boldsymbol{\sigma}^\pi$ is the intrinsic phase averaged stress tensor in the π phase and τ^π is the shear stress.

Under the assumption that the shear stress τ^π is negligible in fluids, we obtain:

$$\bar{\boldsymbol{\sigma}} = (1-n) \boldsymbol{\sigma}^s - n \mathbf{I} [S_g p^g + S_w p^w] \quad (4.133)$$

The term in square brackets of equation (4.132) represents the intrinsically averaged (or mean) pressure p^s of the fluid phases i.e. :

$$p^s = (S_g p^g + S_w p^w) \quad (4.134)$$

This weighted pore pressures produce a stress state in the grains, but, for the moment, we assume these will not undergo any deformation due to this stress, i.e. we introduce the hypothesis of incompressible grains. The deformation of the solid skeleton, which depends on the effective stress, will be a function of the grain rearrangement only.

Equation (4.133) can be modified to:

$$\begin{aligned} \boldsymbol{\sigma} &= (1-n) \boldsymbol{\sigma}^s - n \mathbf{I} p^s \\ &= (1-n) (\boldsymbol{\sigma}^s + \mathbf{I} p^s) - (1-n) \mathbf{I} p^s - n \mathbf{I} p^s \\ &= \boldsymbol{\sigma}' - \mathbf{I} p^s \end{aligned} \quad (4.135)$$

where the overbar for the total stress has been omitted.

The stress tensor is split into two components: the pore pressure effect and the part which deforms the solid skeleton, i.e. the effective stress. This latter is given by:

$$\boldsymbol{\sigma}' = (1-n) (\boldsymbol{\sigma}^s + \mathbf{I} p^s) \quad (4.136)$$

Equation (4.135) results in a splitting of the stress tensor similar to that of Terzaghi's principle, which, in presence of several fluid phases reads:

$$\boldsymbol{\sigma}' = \boldsymbol{\sigma} + \mathbf{I} (S_w p^w + S_g p^g) \quad (4.137)$$

For greater generality, a corrective term known as Biot's constant, has to be introduced to account for the deformability of the grains (Biot & Willis 1957). Therefore a more general expression of the effective stress is assumed as follows:

$$\boldsymbol{\sigma}'' = \boldsymbol{\sigma} + \mathbf{I} \alpha (S_w p^w + S_g p^g) \quad (4.138)$$

where the corrective coefficient α will be determined in section 4.6.2. Note that this equation differs substantially from the previous one: for the determination of α we need the constitutive equations of the solid phase. This effective stress is indicated in this chapter by $\boldsymbol{\sigma}''$ as in (Zienkiewicz et al. 1990).

Another, more intuitive way of deriving equation (4.136) follows (Bishop 1959) and (Skempton 1961). Here the microscopic and macroscopic aspects are somewhat mixed. We consider for this purpose the mean stresses, i.e. :

$$\hat{\sigma} = tr \frac{\boldsymbol{\sigma}}{3} \quad (4.139)$$

and

$$\hat{\sigma}' = tr \frac{\boldsymbol{\sigma}'}{3} \quad (4.140)$$

If the pores (**Fig. 4.3**) are filled with water and air, then due to the surface tension effect we have:

$$p^w < p^g \quad (4.141)$$

If the degree of saturation is relatively low, the water is present as menisci and the corresponding pressure acts over an area χ per unit gross area, (Aitchison & Donald 1956).

Consequently, the equivalent pore pressure is given by:

$$\chi p^w + (1 - \chi) p^s \quad (4.142)$$

and the equivalent pore pressure may be written as:

$$p^s - \chi(p^s - p^w) \quad (4.143)$$

or

$$p^w + (1 - \chi)(p^s - p^w) \quad (4.144)$$

For the fully saturated case, Bishop suggested the following expression for the mean effective stress $\hat{\sigma}'$:

$$\hat{\sigma}' = \hat{\sigma} + [p^s - \chi(p^s - p^w)] \quad (4.145)$$

For the full stress tensor, this equation assumes the form:

$$\boldsymbol{\sigma}' = \boldsymbol{\sigma} + \mathbf{I} [p^s - \chi(p^s - p^w)] \quad (4.146)$$

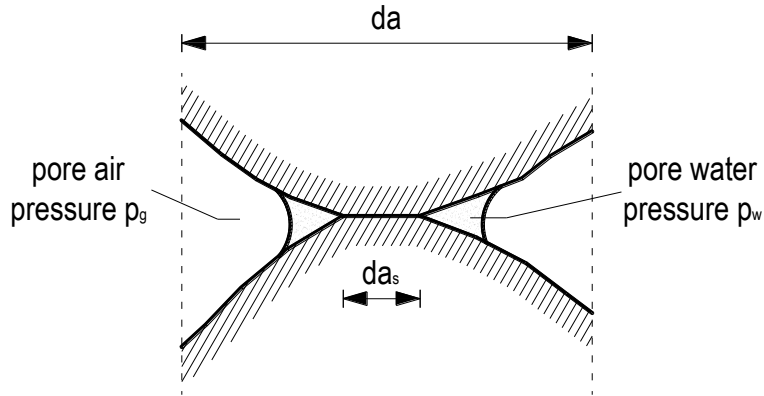


Fig. 4.3: Contact area between two grains in the partially saturated case

The coefficient χ is not the same as for problems involving shear strength and consolidation (Skempton 1961). For a given degree of saturation the coefficient χ must be determined experimentally for both types of problems.

In general the pressure is implied as being an absolute value, but in many soil mechanics problems relative pressures are used and p^s is often assumed to be equal to the atmospheric pressure. If this is the case and the atmospheric pressure is assumed as the reference pressure then the effective stress principle becomes:

$$\boldsymbol{\sigma}' = \boldsymbol{\sigma} + \mathbf{I} \chi p^w \quad (4.147)$$

The comparison between (4.137) and (4.146) is noteworthy. The former may be written as a function of the degree of saturation S_w :

$$\boldsymbol{\sigma} = \boldsymbol{\sigma}' - \mathbf{I} \left[p^g - S_w (p^g - p^w) \right] \quad (4.148)$$

and coincides with equation (4.146) if $\chi = S_w$.

The coefficient χ is related to the area of contact between solid and fluids, whereas the degrees of saturation S_π depend on the volume occupied by the π phase. We define the volume fraction as:

$$\eta^\pi = \frac{dv^\pi}{dv} \quad (4.149)$$

and cross sectional area fraction as:

$$\alpha^\pi = \frac{da^\pi}{da} \quad (4.150)$$

For the case of microstructurally isotropic constituents, such that α^π is independent of the orientation of the surface, and assuming that:

$$\alpha^\pi = \alpha^\pi (\eta^\pi) \quad (4.151)$$

it can be shown that (Morland 1972) :

$$\alpha^\pi = \eta^\pi \quad (4.152)$$

This conclusion coincides with the basic supposition of Delesse's law, see section 4.2.1.

If this assumption regarding the area and volume fraction is valid, then little difference exists between the definition of Bishop's coefficient χ and the degree of water saturation S_w . Bishop's equation (4.145) has been experimentally validated by means of a triaxial tests carried out on soil samples (Skempton 1961).

The assumption:

$$\chi = S_w \quad (4.153)$$

is acceptable for many materials as shown experimentally in (Bishop & Blight 1963).

However, other expressions may also be used, e.g. by Gudehus for clay (Gudehus 1995) :

$$\chi = S(2 - S) \quad (4.154)$$

If the solid phase is completely surrounded by a single wetting fluid phase, which is the only one in direct contact with the porous medium, then Li and Zienkiewicz (Li & Zienkiewicz 1992) use equation (4.137) with $\chi = 1$, as in the case of a fully saturated porous medium. This assumption is widely used when the two fluids are water and bitumen: only water is in contact with the solid grains.

A new expression for the effective stress principle in fully saturated conditions only, involving four parameters, has been proposed by Lade and de Boer (Lade & de Boer 1997) and experimentally tested. This formulation, based on principles of mechanics is valid for all types of materials. A distinction is made between the compressibilities of the grain particles and the skeleton due to total stresses and pore pressures.

Two distinct expressions are then obtained for effective stresses in granular material and in solid rock with interconnected pores respectively. For various special conditions these expressions become similar to the expressions found in the literature, in particular to the expression used here with Biot's constant α . Lade and de Boer (Lade & de Boer 1997) conclude that Terzaghi's proposed effective stress principle works well for stress magnitudes encountered in most geotechnical applications, but significant deviations occur at very high stresses.

4.6.2 Constitutive equations

For a full account of the constitutive relationships used the reader is referred to section 4.4, and only a few equations, needed for the remaining part of this section, are recalled. In particular an expression for Biot's constant α is derived, which was omitted in section 4.4.

The averaged pore pressure p^s of the fluids occupying the void space induce a hydrostatic stress distribution in the solid phase. The ensuing deformation is a purely volumetric strain:

$$\boldsymbol{\varepsilon}_v^s = -\frac{p^s}{K_s} \quad (4.155)$$

where K_s is the averaged bulk modulus of the solid grains.

As stated previously, the effective stress causes all relevant deformation of the solid skeleton. The constitutive relationship may be written as:

$$d\boldsymbol{\sigma}' = \mathbf{D}_T \left[\left(d\boldsymbol{\varepsilon} - d\boldsymbol{\varepsilon}^c - d\boldsymbol{\varepsilon}_v^s - d\boldsymbol{\varepsilon}^o \right) \right] \quad (4.156)$$

where $d\boldsymbol{\sigma}'$ is the stress responsible for all deformations, except for the grain compressibility $d\boldsymbol{\varepsilon}$ represents the total strain of the solid, \mathbf{D}_T is the tangent constitutive tensor:

$$\mathbf{D}_T = \mathbf{D}_T(\boldsymbol{\sigma}', \boldsymbol{\varepsilon}, \dot{\boldsymbol{\varepsilon}}) \quad (4.157)$$

$d\boldsymbol{\varepsilon}^c = g(\boldsymbol{\sigma}')dt$ accounts for the creep strain, $d\boldsymbol{\varepsilon}^o$ represents all other strains in the solid skeleton not directly dependent on effective stress.

A modified effective stress $\boldsymbol{\sigma}''$ will now be introduced which will also account for grain compression. This allows the use of Biot's constant α . Omitting, for brevity, $d\boldsymbol{\varepsilon}^c$ and $d\boldsymbol{\varepsilon}^o$ we obtain:

$$d\boldsymbol{\sigma}' = \mathbf{D}_T \left[\left(d\boldsymbol{\varepsilon} - d\boldsymbol{\varepsilon}_v^s \right) \right] = \mathbf{D}_T [d\boldsymbol{\varepsilon}] + \mathbf{D}_T [\mathbf{I}] \frac{dp^s}{3K_s} \quad (4.158)$$

Consequently, the effective stress equation written in incremental form becomes:

$$d\boldsymbol{\sigma} = d\boldsymbol{\sigma}' - \mathbf{I} dp^s = d\boldsymbol{\sigma}'' + \mathbf{D}_T [\mathbf{I}] \frac{dp^s}{3K_s} - \mathbf{I} dp^s \quad (4.159)$$

where $\boldsymbol{\sigma}''$ represents the stress responsible for all deformation of the solid.

For the following developments we use indicial notation and the Kronecker Symbol δ instead of the unit tensor \mathbf{I} .

It can be immediately verified that equation (4.158) can be written as given by (Zienkiewicz & Shiomi 1985):

$$d \sigma_{ij} = d \sigma_{ij}'' - \frac{1}{3} \left(\delta_{mn} \delta_{nm} - \delta_{mn} D_{mnkl} \delta_{kl} \frac{1}{3K_s} \right) \delta_{ij} dp^s \quad (4.160)$$

For an isotropic, elastic material:

$$\delta_{mn} D_{mnkl} \delta_{kl} = \frac{3E}{1-2\nu} = 9K_T \quad (4.161)$$

where E is the Young's modulus, ν is the Poisson's ratio, K_T is the bulk modulus of the overall skeleton.

Hence equation (4.160) can be written as:

$$d \sigma_{ij} = d \sigma_{ij}'' - \left(1 - \frac{K_T}{K_s} \right) \delta_{ij} d p^s = d \sigma_{ij}'' - \alpha \delta_{ij} dp^s \quad (4.162)$$

where α is Biot's constant.

The resultant expression of the constitutive relationship is therefore:

$$d\boldsymbol{\sigma}'' = \mathbf{D}_T d\boldsymbol{\varepsilon} \quad (4.163)$$

The intrinsic pore pressure p^π of the π fluid phase causes a purely volumetric strain of that phase, which is represented by:

$$\boldsymbol{\varepsilon}_v^\pi = -\frac{p^\pi}{K_\pi} \quad (4.164)$$

4.6.3 Governing equations

In the following a material coordinate system is employed for the solid phase and a spatial coordinate system for the fluid phases; convective terms, unless specified otherwise, are neglected. Because of this choice of reference systems the fluid velocities are conveniently referred to the solid phase by means of the relative velocities for water and gas respectively:

$$\mathbf{v}^{ws} = \mathbf{v}^w - \mathbf{v}^s \quad (4.165)$$

$$\mathbf{v}^{gs} = \mathbf{v}^g - \mathbf{v}^s \quad (4.166)$$

and the accelerations, without convective terms, are:

$$\mathbf{a}^w = \mathbf{a}^s + \mathbf{a}^{ws} \quad (4.167)$$

$$\mathbf{a}^g = \mathbf{a}^s + \mathbf{a}^{gs} \quad (4.168)$$

where \mathbf{a}^{ws} is the acceleration of water relative to the solid phase and \mathbf{a}^{gs} the relative acceleration of gas.

Linear momentum balance equation of the multiphase medium

The linear momentum balance equation for the multiphase system is the sum of the dynamics equations for the individual constituents, but relative to the solid phase via equations (4.167) and (4.168) :

$$-\rho \mathbf{a}^s - n S_w \rho^w \mathbf{a}^{ws} - n S_g \rho^g \mathbf{a}^{gs} + \text{div} \boldsymbol{\sigma} + \rho \mathbf{g} = 0 \quad (4.169)$$

where

$$\rho = (1-n) \rho^s + n S_w \rho^w + n S_g \rho^g \quad (4.170)$$

is the averaged density of the multiphase systems, ρ^s is the intrinsic density of the solid phase, i.e. the density referred to the volume occupied by the solid phase only, as opposed to the volume occupied by the multiphase system, ρ^w is the intrinsic density of water, ρ^g the intrinsic density of gas, \mathbf{g} an acceleration usually related to gravitational effects.

The linear momentum balance equation for each fluid phase yields the generalized form of Darcy's law, where the dissipative terms arising in a multiphase flow system at the interfaces are taken into account through the relative permeabilities:

$$n S_w \mathbf{v}^{ws} = \frac{\mathbf{k} k^{rw}}{\mu_w} \left[-\text{grad } p^w + \rho^w (\mathbf{g} - \mathbf{a}^s - \mathbf{a}^{ws}) \right] \quad (4.171)$$

$$nS_g \mathbf{v}^{gs} = \frac{\mathbf{k}k^{rg}}{\mu_g} \left[-grad p^g + \rho^g (\mathbf{g} - \mathbf{a}^s - \mathbf{a}^{gs}) \right] \quad (4.172)$$

where \mathbf{k} is the intrinsic permeability, k^w and k^g the relative permeabilities of water and gas, μ_w and μ_g are the dynamic viscosities.

The relative permeabilities vary between 0 and 1 and are a function of the degree of saturation; the dynamic viscosities are temperature dependent. In the generalized form of Darcy's law for the gas phase the body forces are usually neglected. The L.H.S. of equations (4.171) and (4.172) are multiplied by the volume fractions nS_π because Darcy's law is expressed in terms of volume averaged relative velocities. These are the velocities measured from experiment work.

Mass balance equations

The summation of mass balance equations of mass and fluid, with opportune arrangements and yields the so-called continuity equation of the fluid phase i.e. :

$$\frac{(1-n)}{\rho^s} \frac{\partial \rho^s}{\partial t} + div \mathbf{v}^s + \frac{n}{\rho^\pi} \frac{\partial \rho^\pi}{\partial t} + \frac{n}{S_\pi} \frac{\partial S_\pi}{\partial t} + \frac{1}{S_\pi \rho^\pi} (nS_\pi \rho^\pi \mathbf{v}^{\pi s}) = \pm \frac{\dot{m}}{\rho^\pi S_\pi} \quad (4.173)$$

We consider first the continuity equation for water. Introduction of the constitutive relationships for the time derivatives of water density and solid density, of the pressure in the solid phase, and multiplication by S_w allows the continuity equation for water and then with the introduction of Darcy's law and of the definition of capillary pressure yields:

$$\begin{aligned} & \left(\frac{\alpha - n}{K_s} S_w^2 + \frac{nS_w}{K_w} \right) \frac{\partial p^w}{\partial t} + \frac{\alpha - n}{K_s} S_w S_g \frac{\partial p^g}{\partial t} + \alpha S_w div \mathbf{v}^s \\ & - \beta_{sw} \frac{\partial T}{\partial t} + \left(\frac{n - \alpha}{K_s} S_w p^c + n \right) \frac{\partial S_w}{\partial t} \\ & + \frac{1}{\rho^w} div \left\{ \rho^w \frac{\mathbf{k}k^{rw}}{\mu_w} \left[-grad p^w + \rho^w (\mathbf{g} - \mathbf{a}^s - \mathbf{a}^{ws}) \right] \right\} = - \frac{\dot{m}}{\rho^w} \end{aligned} \quad (4.174)$$

In the same way the continuity equation for gas is obtained:

$$\begin{aligned}
& \frac{\alpha - n}{K_s} S_w S_g \frac{\partial p^w}{\partial t} + \frac{\alpha - n}{K_s} S_g^2 \frac{\partial p^g}{\partial t} - \left(n + \frac{\alpha - n}{K_s} p^c S_g \right) \frac{\partial S_w^s}{\partial t} \\
& - \beta_s (\alpha - n) S_g \frac{\partial T}{\partial t} + \alpha S_g \operatorname{div} \mathbf{v}^s + \frac{n S_g}{\rho^g} \frac{\partial}{\partial t} \left(\frac{p^g M_g}{\theta R} \right) \\
& + \frac{1}{\rho^g} \operatorname{div} \left\{ \rho^g \frac{\mathbf{k} \mathbf{k}^{rg}}{\mu_g} \left[-\operatorname{grad} p^g + \rho^g (\mathbf{g} - \mathbf{a}^s - \mathbf{a}^{gs}) \right] \right\} = -\frac{\dot{m}}{\rho^g}
\end{aligned} \tag{4.175}$$

Energy balance equation

By subtracting the kinetic energy from a global energy balance, the balance equation of thermal energy may be written for constituent π as (Bird et al. 1960) :

$$\frac{\partial}{\partial t} (\rho^\pi E^\pi) = -\operatorname{div} (\rho^\pi E^\pi \mathbf{v}^\pi) - \operatorname{div} \tilde{\mathbf{q}}^\pi - \bar{p}^\pi \operatorname{div} \mathbf{v}^{\pi s} + \boldsymbol{\tau}^\pi \cdot \operatorname{grad} \mathbf{v}^\pi + \rho^\pi R^\pi \tag{4.176}$$

where E^π is the specific internal energy, $\boldsymbol{\tau}$ is the deviatoric part of the stress tensor, \bar{p}^π the hydrostatic part of the stress tensor.

The L.H.S. represents the rate of accumulation of internal energy in a control volume. The R.H.S. terms express respectively the rate of internal energy change due to convection and to conduction, the reversible rate of internal energy increase due to pressure, the irreversible rate of internal energy increase by viscous dissipation and the contribution of heat sources.

In small strain the energy balance equation becomes:

$$\rho^\pi \frac{\partial E^\pi}{\partial t} + \rho^\pi \mathbf{v}^\pi \cdot \operatorname{grad} E^\pi = -\operatorname{div} \tilde{\mathbf{q}}^\pi - \bar{p}^\pi \operatorname{div} \mathbf{v}^\pi + \boldsymbol{\tau}^\pi \cdot \operatorname{grad} \mathbf{v}^\pi + \rho^\pi R^\pi \tag{4.177}$$

The irreversible part of the internal energy increase by viscous dissipation is neglected in what follows. It is convenient to express this equation in terms of temperature and heat capacity instead of internal energy (Bird et al. 1960). This is done through the concept of enthalpy. Hence with sufficient accuracy for geomechanical applications the energy balance equation can be rewritten as:

$$\rho^\pi C_p^\pi \left(\frac{\partial T^\pi}{\partial t} + \mathbf{v}^\pi \cdot \operatorname{grad} T^\pi \right) = -\operatorname{div} \tilde{\mathbf{q}}^\pi + \rho^\pi R^\pi \tag{4.178}$$

for $\pi=s,w$, which for the purpose of the energy balance only may be considered as incompressible, and

$$\rho^\pi C_p^g \left(\frac{\partial T^g}{\partial t} + \mathbf{v}^g \cdot \mathit{grad} T^g \right) = -\mathit{div} \tilde{\mathbf{q}}^g + \frac{\partial p^g}{\partial t} + \mathbf{v}^g \cdot \mathit{grad} p^g + \rho^g R^g \quad (4.179)$$

where C_p^g is the specific heat at constant pressure.

Some insignificant terms which are related to the mechanical work induced by density variations due to temperature changes of the water and solid phases have been neglected.

Gas pressure changes are usually very slow and their gradients small in geomaterials, hence the time derivatives of gas pressure, as well as the convective terms, are negligible with respect to other terms in equation (4.179). Also, because gas pressure changes are usually small when compared to atmospheric pressure, the specific heat at constant pressure may be utilised instead of specific heat at constant volume.

A local equilibrium state is assumed to hold i.e. :

$$T^s = T^w = T^g = T \quad (4.180)$$

We also introduce the constitutive equation for heat fluxes, and add together equations (4.178) and (4.179), and introduce the appropriate heat sources to obtain the following form of the energy balance equation:

$$\left(\rho C_p \right)_{\text{eff}} \frac{\partial T}{\partial t} + \left(\rho^w C_p^w \mathbf{v}^w + \rho^g C_p^g \mathbf{v}^g \right) \cdot \mathit{grad} T - \mathit{div} \left(\chi_{\text{eff}} \mathit{grad} T \right) = -\dot{m} \Delta H_{\text{vap}} \quad (4.181)$$

where ΔH_{vap} is the latent heat of evaporation.

The convective heat flux in the solid phase has been neglected.

4.7 Quasi – static case

The relationships shown in 4.6.3 are now presented for quasi static conditions. In poor words, the equations are rewritten by not taking into account the terms in which appear the acceleration, so is possible neglect the terms \mathbf{a}^w , \mathbf{a}^s , \mathbf{a}^{ws} , \mathbf{a}^g and \mathbf{a}^{gs} used in the relationship (4.167) and (4.168).

For this work of PhD, the equations used are those in quasi static condition.

4.7.1 Equilibrium equation of the multiphase medium

The equation (4.169) becomes:

$$\operatorname{div} \boldsymbol{\sigma} + \rho \mathbf{g} = 0 \quad (4.182)$$

where, as already mentioned above:

$$\rho = (1-n)\rho^s + n S_w \rho^w + n S_g \rho^g \quad (4.183)$$

is the averaged density of the multiphase systems, ρ^s is the intrinsic density of the solid phase, i.e. the density referred to the volume occupied by the solid phase only, as opposed to the volume occupied by the multiphase system, ρ^w is the intrinsic density of water, ρ^g the intrinsic density of gas, \mathbf{g} an acceleration usually related to gravitational effects.

4.7.2 Mass balance equations

The equations (4.174) and (4.175) become:

$$\begin{aligned} & \left(\frac{\alpha-n}{K_s} S_w^2 + \frac{n S_w}{K_w} \right) \frac{\partial p^w}{\partial t} + \frac{\alpha-n}{K_s} S_w S_g \frac{\partial p^g}{\partial t} + \alpha S_w \operatorname{div} \mathbf{v}^s \\ & - \beta_{sw} \frac{\partial T}{\partial t} + \left(\frac{n-\alpha}{K_s} S_w p^c + n \right) \frac{\partial S_w}{\partial t} \\ & + \frac{1}{\rho^w} \operatorname{div} \left\{ \rho^w \frac{\mathbf{k}k^{rw}}{\mu_w} [-\operatorname{grad} p^w + \rho^w \mathbf{g}] \right\} = 0 \end{aligned} \quad (4.184)$$

In the same way the continuity equation for gas is obtained:

$$\begin{aligned} & \frac{\alpha-n}{K_s} S_w S_g \frac{\partial p^w}{\partial t} + \frac{\alpha-n}{K_s} S_g^2 \frac{\partial p^g}{\partial t} - \left(n + \frac{\alpha-n}{K_s} p^c S_g \right) \frac{\partial S_w}{\partial t} \\ & - \beta_s (\alpha-n) S_g \frac{\partial T}{\partial t} + \alpha S_g \operatorname{div} \mathbf{v}^s + \frac{n S_g}{\rho^g} \frac{\partial}{\partial t} \left(\frac{p^g M_g}{\theta R} \right) \\ & + \frac{1}{\rho^g} \operatorname{div} \left\{ \rho^g \frac{\mathbf{k}k^{rg}}{\mu_g} [-\operatorname{grad} p^g + \rho^g \mathbf{g}] \right\} = 0 \end{aligned} \quad (4.185)$$

4.7.3 Energy balance equation

The equation (4.181) does not change for the quasi static case but, by using Darcy' law, can be rewritten in a complete mode as follows:

$$\begin{aligned}
& \left(\rho C_p \right)_{eff} \frac{\partial T}{\partial t} + \rho^w C_p^w \left[\frac{\mathbf{k} \mathbf{k}^{rw}}{\mu^w} \left[-grad(p^g) + grad(p^c) + \rho^w g \right] \right] \cdot grad T \\
& \rho^g C_p^g \left[\frac{\mathbf{k} \mathbf{k}^{rg}}{\mu^g} \left[-grad(p^g) + \rho^g g \right] \right] \cdot grad T - div(\chi_{eff} grad T) = -\dot{m} \Delta H_{vap}
\end{aligned} \tag{4.186}$$

4.7.4 Further developments of the model

The same equations see for this model, hence the linear momentum balance equation, the mass balance equations and the energy balance equation, were developed by considering air dissolved in water by Gawin and Sanavia. For further information, see (Gawin & Sanavia 2010) and (Gawin & Sanavia 2009).

4.8 Boundary and initial conditions

For the model closure the initial and boundary conditions are needed. The initial conditions specify the full fields of primary state variables at time $t=t_0$, in the whole analysed domain B and on its boundary ∂B :

$$\partial B = \partial B_\pi \cup \partial B_\pi^q \quad \pi = g, c, T, \mathbf{u} \tag{4.187}$$

$$\begin{aligned}
p^g &= p_0^g \\
p^c &= p_0^c \\
T &= T_0 \\
\mathbf{u} &= \mathbf{u}_0
\end{aligned} \quad \text{on } B \cup \partial B \tag{4.188}$$

The boundary conditions (BCs) can be of Dirichlet's type on ∂B_π for $t \geq t_0$:

$$\begin{aligned}
p^g &= \hat{p}^g \quad \text{on } \partial B_g \\
p^c &= \hat{p}^c \quad \text{on } \partial B_c \\
T &= \hat{T} \quad \text{on } \partial B_T \\
\mathbf{u} &= \hat{\mathbf{u}} \quad \text{on } \partial B_u
\end{aligned} \tag{4.189}$$

or of Cauchy's type (the mixed BCs) on ∂B_π^q for $t \geq t_0$:

$$\left(nS_g \rho^{ga} \mathbf{v}^{gs} + \mathbf{J}_d^{ga} \right) \cdot \mathbf{n} = q^{ga} \quad \text{on } \partial B_g^q \quad (4.190)$$

$$\left(nS_w \rho^w \mathbf{v}^{ws} + nS_g \rho^{gw} \mathbf{v}^{gs} + \mathbf{J}_d^{gw} \right) \cdot \mathbf{n} = q^{gw} + q^w + \beta_c \left(\rho^{gw} - \rho_\infty^{gw} \right) \quad \text{on } \partial B_c^q \quad (4.191)$$

$$\left(nS_w \rho^w \mathbf{v}^{ws} \Delta H_{vap} - \chi_{eff} grad T \right) \cdot \mathbf{n} = q^T + q^w + \alpha_c (T - T_\infty) + e \sigma_0 (T^4 - T_\infty^4) \quad \text{on } \partial B_T^q \quad (4.192)$$

$$\boldsymbol{\sigma} \cdot \mathbf{n} = \bar{\mathbf{t}} \quad \text{on } \partial B_u^q \quad (4.193)$$

where $\mathbf{n}(\mathbf{x},t)$ is the unit normal vector, $q^{ga}(\mathbf{x},t)$ is the imposed fluxes of dry air, $q^{gw}(\mathbf{x},t)$ is the imposed fluxes of vapour, $q^w(\mathbf{x},t)$ is the imposed fluxes of liquid water, $q^T(\mathbf{x},t)$ is the imposed imposed heat flux, $\bar{\mathbf{t}}(\mathbf{x},t)$ is the imposed traction vector related to the total Cauchy stress tensor $\boldsymbol{\sigma}(\mathbf{x},t)$, $\rho_\infty^{gw}(\mathbf{x},t)$ is the mass concentration of water vapour, $T_\infty(\mathbf{x},t)$ is the temperature in the far field of undisturbed gas phase, $e(\mathbf{x},t)$ is the emissivity of the interface, $\sigma_0(\mathbf{x},t)$ is the Stefan-Boltzmann constant, $\beta_c(\mathbf{x},t)$ is the convective heat exchange coefficients, $\alpha_c(\mathbf{x},t)$ is the convective mass exchange coefficients.

The boundary conditions with only imposed fluxes are called Neumann' BCs. The purely convective boundary conditions for heat and moisture exchange are also called Robin' BCs.

5 The code Comes-Geo

5.1 Introduction

The COMES-GEO finite element code carries out the hydro-thermo-mechanical analysis of porous materials with interconnected pores in which the flow of one or more fluid phases takes place.

The interactions between fluid and solid phases are taken into account. Geomaterials (soils, rocks, concrete), are the most common examples of such porous media. The majority of the codes which are currently available in the market, do not deal with more than a single fluid phase. Therefore it is not possible to carry out realistic numerical studies of porous materials structures in partially saturated conditions as:

1. stability analysis of soil slopes;
2. seismic analysis of soil dams where in the upper part wide zones, containing pores filled with air and water, are present;
3. simulation of the subsidence phenomena in presence of gas extraction from deep reservoir. In this case water and different gases are present in the pores. The gas reservoirs in the northern Adriatic Sea are an important example in Italy.

The COMES-GEO code, developed by the University of Padova, is able to deal with these problems and also with many others applications in environmental geomechanics.

The problem unknowns are the following: temperature, capillary pressure, gas pressure and displacements. These data allow the calculation of interesting derived outputs (e.g. saturation, stress-strain fields).

To reach the solution of the problem using the considered model, four balance equations are imposed (see chapter 4): mass of the dry air, mass of the water species (both liquid water and

vapour; phase change is considered); energy conservation of the mixture and the equilibrium equation of the multiphase medium. They are completed by an appropriate set of constitutive and state equations, as well as some thermodynamic relationships.

COMES-GEO allows finite element analysis in plane strain and axisymmetric conditions, using four node bilinear elements or Serendipity eight node elements or Lagrange nine node elements.

The source is written in FORTRAN 90.

5.2 Finite element method

Numerical solution to the mathematical system presented in chapter 4, is obtained by using the finite element method. In what follows, we describe the particular method employed for the spatial discretization of the numerical system.

More specifically, we have applied the Galerkin form of the method of weighted residuals (MWR) to produce an integral representation of the governing equations.

These relations are then specialized to finite element method.

For further information see (Sanavia et al. 2006).

5.2.1 Method of Weighted Residuals: discretization in space

To apply the MWR to the particular problem at hand, we assume that the region of interest Ω is divided into a number of simply shaped regions, the finite elements, as shown in **Fig. 5.1**.

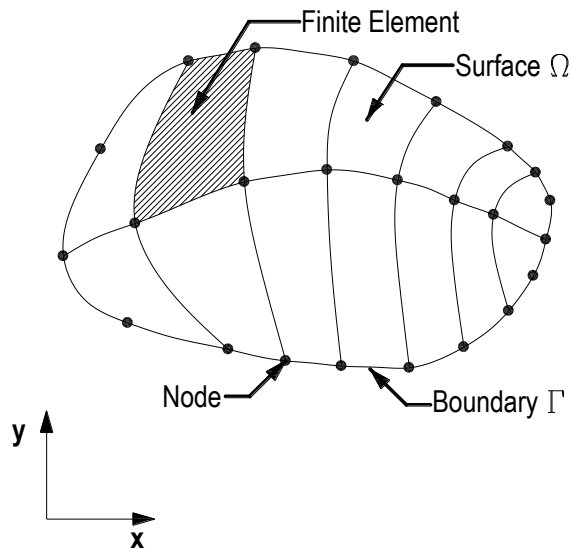


Fig. 5.1 Schematic division in simply regions

Within each element, a set of nodal points is established at which the dependent variables p_g , p_c , T , u_x and u_y are evaluated, where

1. p_g is the pressure of gas (dry air, vapour or any other perfect gas) expressed in Pa
2. p_c is the capillary pressure (or matric suction) expressed in Pa
3. T is the temperature expressed in K
4. u_x and u_y are the displacement expressed in m

For the purpose of developing the equations for these nodal unknowns, an individual element is separated from the assemblage.

Within each element, it is assumed that the dependent variables can be expressed in terms of approximating function to shape functions by:

$$p_g(t) = N_p \bar{p}_g(t) \quad (5.1)$$

$$p_c(t) = N_p \bar{p}_c(t) \quad (5.2)$$

$$T(t) = N_T \bar{T}(t) \quad (5.3)$$

$$\mathbf{u}(t) = N_u \bar{\mathbf{u}}(t) \quad (5.4)$$

where the upper line indicates the nodal values. Substitution of the relations (5.1)(5.2)(5.3) and (5.4) into the partial differential equations see in chapter 4, and boundary conditions, will result in a set of residual equations due to the approximate nature of relations (5.1)(5.2)(5.3) and (5.4).

The MWR is then used to reduce the residual expression to zero in a weighted integral sense through the introduction of:

$$\int_{\Omega} N_x \mathbf{R}_x d\Omega + \int_{\Gamma} N_x \mathbf{R}_x d\Gamma = \mathbf{0} \quad (5.5)$$

where $\mathbf{x}^T = \{\bar{p}_g, \bar{p}_c, \bar{T}, \bar{\mathbf{u}}\}$, N_x are weighting or test functions, \mathbf{R} is the residual for a field equation, $\mathbf{R}_x(\text{b.c.})$ is the residual for the boundary condition

The integral or weak form of the heat and mass transfer equations (and of the other ones required to complete the model), obtained by means of the Galerkin procedure (weighted

residuals), (Zienkiewicz & Taylor 1989; Zienkiewicz & Taylor 1991), can be expressed in matrix form as (Gawin et al. 1996; Schrefler & Gawin 1996):

$$\begin{aligned}
C_{gg}\bar{\mathbf{p}}_g + C_{gc}\bar{\mathbf{p}}_c + C_{gT}\bar{\mathbf{T}} + C_{gu}\bar{\mathbf{u}} + \mathbf{K}_{gg}\bar{\mathbf{p}}_g + \mathbf{K}_{gc}\bar{\mathbf{p}}_c + \mathbf{K}_{gT}\bar{\mathbf{T}} + \mathbf{f}_g &= \mathbf{0} \\
C_{cg}\bar{\mathbf{p}}_g + C_{cc}\bar{\mathbf{p}}_c + C_{cT}\bar{\mathbf{T}} + C_{cu}\bar{\mathbf{u}} + \mathbf{K}_{cg}\bar{\mathbf{p}}_g + \mathbf{K}_{cc}\bar{\mathbf{p}}_c + \mathbf{K}_{cT}\bar{\mathbf{T}} + \mathbf{f}_c &= \mathbf{0} \\
C_{Tg}\bar{\mathbf{p}}_g + C_{Tc}\bar{\mathbf{p}}_c + C_{TT}\bar{\mathbf{T}} + C_{Tu}\bar{\mathbf{u}} + \mathbf{K}_{Tg}\bar{\mathbf{p}}_g + \mathbf{K}_{Tc}\bar{\mathbf{p}}_c + \mathbf{K}_{TT}\bar{\mathbf{T}} + \mathbf{f}_T &= \mathbf{0} \\
C_{uu}\bar{\mathbf{u}} + C_{ug}\bar{\mathbf{p}}_g + C_{uc}\bar{\mathbf{p}}_c + C_{uT}\bar{\mathbf{T}} + \mathbf{f}_u &= \mathbf{0}
\end{aligned} \tag{5.6}$$

The above non-symmetric, non-linear and coupled system of ordinary differential equations can be rewritten in compact form as:

$$\mathbf{C}(\mathbf{x})\dot{\mathbf{x}} + \mathbf{K}(\mathbf{x})\mathbf{x} + \mathbf{f}(\mathbf{x}) = \mathbf{0} \tag{5.7}$$

where $\mathbf{x}^T = \{\bar{\mathbf{p}}_g, \bar{\mathbf{p}}_c, \bar{\mathbf{T}}, \bar{\mathbf{u}}\}$ and the non-linear (matrix) coefficients $\mathbf{C}(\mathbf{x})$, $\mathbf{K}(\mathbf{x})$ and $\mathbf{f}(\mathbf{x})$ are obtained by assembling the sub-matrices indicated in (5.6).

5.2.2 Linearization. Discretization in time

Finite differences in time, (Zienkiewicz & Taylor 1989; Zienkiewicz & Taylor 1991), are used for the solution of the initial value problem over a finite time step:

$$\Delta t = t_{n+1} - t_n \tag{5.8}$$

where n is the time step number.

Following the Generalised Trapezoidal Method as shown for instance in (Lewis & Schrefler 1998), equation (5.7) is rewritten at time t_{n+1} using the relationships:

$$\left. \frac{\partial \mathbf{x}}{\partial t} \right|_{n+\theta} = \frac{\mathbf{x}_{n+1} - \mathbf{x}_n}{\Delta t} \tag{5.9}$$

$$\mathbf{x}_{n+\theta} = (1-\theta)\mathbf{x}_n + \theta\mathbf{x}_{n+1} \quad \text{with } \theta = [0, 1] \tag{5.10}$$

where \mathbf{x}_n is the state vector at time t_n , \mathbf{x}_{n+1} is the state vector at time t_{n+1} , Δt is the time step length, thus obtaining:

$$\mathbf{G}(\mathbf{x}_{n+1}) = (\mathbf{C} + \theta \Delta t \mathbf{K})_{n+\theta} \mathbf{x}_{n+1} - (\mathbf{C} - (1-\theta) \Delta t \mathbf{K})_{n+\theta} \mathbf{x}_n - \Delta t \mathbf{F}_{n+\theta} = \mathbf{0} \quad (5.11)$$

Linearized analysis of accuracy and stability suggests the use of $\theta \geq 1/2$. In the present work implicit one-step time integration has been performed ($\theta = 1$).

After time integration the non-linear system of equation is linearized, thus obtaining the equations system that can be solved numerically (in compact form):

$$\left. \frac{\partial \mathbf{G}}{\partial \mathbf{x}} \right|_{\mathbf{x}_{n+1}^i} \cdot \Delta \mathbf{x}_{n+1}^{i+1} \cong -\mathbf{G}(\mathbf{x}_{n+1}^i) \quad (5.12)$$

where $(\bullet)_{n+1}^{i+1}$ indicates the current iteration (i+1) in the current time step (n+1).

The Jacobian matrix has the following form:

$$\left. \frac{\partial \mathbf{G}}{\partial \mathbf{x}} \right|_{\mathbf{x}_{n+1}^i} = \begin{bmatrix} \frac{\partial G_g}{\partial \bar{p}_g} & \frac{\partial G_g}{\partial \bar{p}_c} & \frac{\partial G_g}{\partial \bar{T}} & \frac{\partial G_g}{\partial \bar{u}} \\ \frac{\partial G_c}{\partial \bar{p}_g} & \frac{\partial G_c}{\partial \bar{p}_c} & \frac{\partial G_c}{\partial \bar{T}} & \frac{\partial G_c}{\partial \bar{u}} \\ \frac{\partial G_T}{\partial \bar{p}_g} & \frac{\partial G_T}{\partial \bar{p}_c} & \frac{\partial G_T}{\partial \bar{T}} & \frac{\partial G_T}{\partial \bar{u}} \\ \frac{\partial G_u}{\partial \bar{p}_g} & \frac{\partial G_u}{\partial \bar{p}_c} & \frac{\partial G_u}{\partial \bar{T}} & \frac{\partial G_u}{\partial \bar{u}} \end{bmatrix} \quad (5.13)$$

Owing to the strong coupling between the mechanical, thermal and the pore fluids problem, a monolithic solution of (5.12) is preferred using a Newton scheme, so it can be written:

$$\begin{aligned} & \frac{1}{\Delta t} \left[\frac{\partial}{\partial \mathbf{x}} \mathbf{C}(\mathbf{x}_{n+1}^l) (\mathbf{x}_{n+1}^l - \mathbf{x}_n) + \mathbf{C}(\mathbf{x}_{n+1}^l) \right] \Delta \mathbf{x}_{n+1}^l + \\ & + \left[\frac{\partial}{\partial \mathbf{x}} \mathbf{K}(\mathbf{x}_{n+1}^l) \mathbf{x}_{n+1}^l + \mathbf{K}(\mathbf{x}_{n+1}^l) + \frac{\partial}{\partial \mathbf{x}} \mathbf{f}(\mathbf{x}_{n+1}^l) \right] \Delta \mathbf{x}_{n+1}^l = \\ & = - \left[\mathbf{C}(\mathbf{x}_{n+1}^l) \frac{\mathbf{x}_{n+1}^l - \mathbf{x}_n}{\Delta t} + \mathbf{K}(\mathbf{x}_{n+1}^l) \mathbf{x}_{n+1}^l + \mathbf{f}(\mathbf{x}_{n+1}^l) \right] \end{aligned} \quad (5.14)$$

Finally, the solution vector $\mathbf{x}^T = \{\bar{p}_g, \bar{p}_c, \bar{T}, \bar{u}\}$ is then updated by the incremental relationship:

$$\mathbf{x}_{n+1}^{l+1} = \mathbf{x}_{n+1}^l + \Delta \mathbf{x}_{n+1}^l \quad (5.15)$$

For the convergence and error analysis of the method applied here the interested reader is referred to (Gawin & Schrefler 1996).

5.3 Finite element library

Three basic elements are utilized in the COMES-GEO code: the isoparametric quadrilateral elements with four and eight node Lagrangian elements and the eight node Serendipity element.

Within a particular element, the state variables are approximated using linear or quadratic shape functions:

$$p_g = p_g(t) = N_p \bar{p}_g(t) \quad (5.16)$$

$$p_c = p_c(t) = N_p \bar{p}_c(t) \quad (5.17)$$

$$T = T(t) = N_T \bar{T}(t) \quad (5.18)$$

$$\mathbf{u} = \mathbf{u}(t) = N_u \bar{\mathbf{u}}(t) \quad (5.19)$$

Basic concepts of Finite Element Method element construction and isoparametric element formulation are thoroughly described e.g. by Zienkiewicz (Zienkiewicz & Taylor 1989).

The interpolation functions for any elements shown below can be found in (Zienkiewicz & Taylor 1989).

5.3.1 Four node quadrilateral elements

The basic four node quadrilateral element used in the code has 20 degrees of freedom as shown in **Fig. 5.2** :

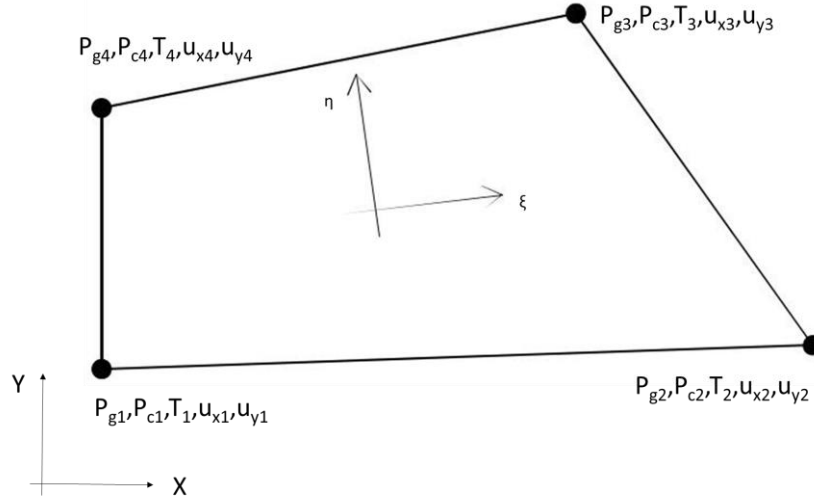


Fig. 5.2 Four node quadrilateral element

5.3.2 Eight node quadrilateral elements

The basic four node quadrilateral element used in the code has 40 degrees of freedom as shown in **Fig. 5.3** :

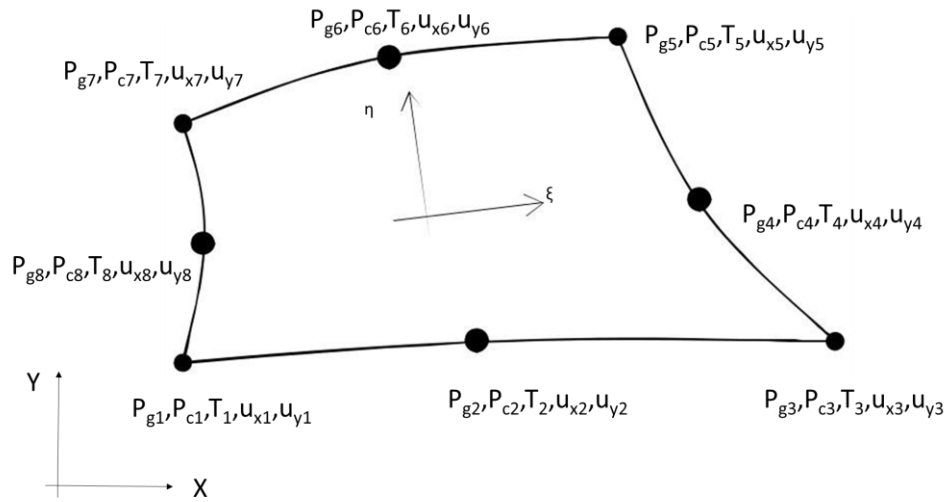


Fig. 5.3 Eight node quadrilateral element

5.3.3 Nine node quadrilateral elements

The basic nine node quadrilateral element used in the code has 45 degrees of freedom as shown in **Fig. 5.4** :

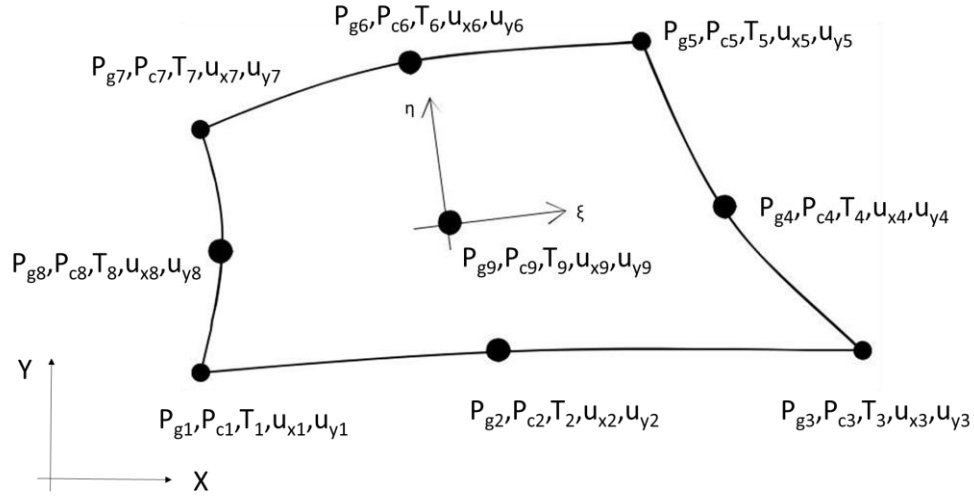


Fig. 5.4 Nine node quadrilateral element

5.4 Numerical integration

As far as the numerical integration is concerned, the classical Gauss method is implemented in the code.

In this method the required matrix integrals, used in F.E.M., are in practice evaluated numerically using, for the case treated here:

$$\int \mathbf{F}(r, s) dr ds = \sum_{i,j} \alpha_{ij} \mathbf{F}(r_i, s_j) \quad (5.20)$$

The above formula is directly applicable to the calculation of matrices of rectangular elements, in which all integration limits are -1 to +1. Thus we can apply the one-dimensional integration formulas successively in each direction. As the analytical evaluation of multi-dimensional integrals, in this procedure, successively, the innermost integral is evaluated by keeping the variables corresponding to the other integrals constant.

Therefore, we have for a two dimensional integral:

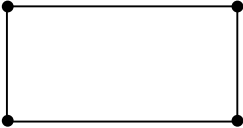
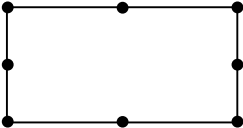
$$\int_{-1}^{+1} \int_{-1}^{+1} \mathbf{F}(r, s) dr ds = \sum_i \alpha_i \int_{-1}^{+1} \mathbf{F}(r_i, s) ds \quad (5.21)$$

or

$$\int_{-1}^{+1} \int_{-1}^{+1} \mathbf{F}(r, s) dr ds = \sum_{i,j} \alpha_i \alpha_j \mathbf{F}(r_i, s_j) \quad (5.22)$$

In COMES-GEO code we have the possibility to use different orders of integration. The possible numerical integration are presented in the following table, but for the kind of problems resolved using COMES-GEO, fully coupled and strongly non-linear, it is suggest to use eight node quadrilateral elements with a 3×3 numerical integration.

Table 2 Type of element and order of integration

Type of element	Order of integration	Note
	2×2	There is not stabilization in case of reduced interpolation (i.e. with 1 gauss point)
	3×3	also 2×2 is available

5.5 Matrix solution procedure

When the solution algorithms of the theory section are applied to a given iteration or time step, the general result is a matrix equation of the form: $\mathbf{Ax} = \mathbf{b}$.

In the problem considered here the \mathbf{A} matrix is large (e.g. several thousand equations), sparse, banded, and generally non-symmetric.

The solution of the equations system (4.14) may be approached by a direct method.

The solution procedure used in COMES-GEO is a form of Gauss elimination developed by Irons, called frontal solution method. In particular it is a super-fast frontal elimination routine using diagonal pivoting reduced fill-in version which assembles the contribution of each element to form the global stiffness matrix and global load vector and to solve the resulting set of simultaneous equations by Gaussian direct elimination (Bianco et al. 2003).

The main feature of the frontal solution technique is that it assembles the equations and eliminates the variables at the same time.

In fact the basic premise of the frontal method is that the process of assembling the system matrix A , from the individual element matrices and the reduction of A by standard Gauss elimination may be efficiently intertwined.

In processing each element in sequence, the frontal procedure passes through the following steps:

1. assembly of element equations into global matrix A ;
2. check each equation in the assembled system to determine if all contributions to this equation have been made;
3. condense from the system (by Gaussian elimination) the equations for all degrees of freedom that have been completely assembled;
4. return to step 1. for the next element.

By combining the assembly and reduction process, computer storage is effectively minimized since only the currently “active” (i.e. incompletely assembled) degrees of freedom are retained in the core storage.

Following the reduction of the matrix A to an upper triangular form, a back-substitution algorithm completes the solution process for the vector x .

Since the frontal method is structured around the individual element, it is especially adaptable for general purpose code with an element library.

The processing of higher order elements (e.g. quadratic basis functions) is also handled efficiently by frontal method.

The frontal procedure in COMES-GEO employs diagonal pivoting reduced fill-in. In our case it is a total pivoting which is related to the numerical stability in a strong manner, and works on rows and columns to find the “pivot”. The pivoting technique allows improving the convergence of the numerical system.

5.6 Convergence and error analysis

The discretization in space of the balance equations (and of the other ones required to complete the model) with the standard Galerkin method (weighted residuals), results in a non-symmetric, non-linear and coupled system of ordinary differential equations as shown in the section 5.2:

$$\mathbf{C}(\mathbf{x})\dot{\mathbf{x}} + \mathbf{K}(\mathbf{x})\mathbf{x} + \mathbf{f}(\mathbf{x}) = \mathbf{0} \quad (5.23)$$

where $\mathbf{x}^T = \{\bar{\mathbf{p}}_g, \bar{\mathbf{p}}_c, \bar{\mathbf{T}}, \bar{\mathbf{u}}\}$, and the non-linear (matrix) coefficients $\mathbf{C}(\mathbf{x})$, $\mathbf{K}(\mathbf{x})$ and $\mathbf{f}(\mathbf{x})$ are obtained by assembling the sub-matrices indicated in (4.6).

We assume consistency and convergence of the finite element discretization in space. The time discretization is accomplished through a fully implicit finite difference scheme (backward difference):

$$\mathbf{A}\mathbf{x}_{n+1} - \mathbf{B}\mathbf{x}_n - \mathbf{F} = \mathbf{0} \quad (5.24)$$

where

$$\mathbf{A} = \mathbf{C}(\mathbf{x}_{n+1}) + \mathbf{K}(\mathbf{x}_{n+1})\Delta t \quad (5.25)$$

$$\mathbf{B} = \mathbf{C}(\mathbf{x}_{n+1}) \quad (5.26)$$

$$\mathbf{F} = -\mathbf{f}(\mathbf{x}_{n+1})\Delta t \quad (5.27)$$

We focus our attention on the global error:

$$\mathbf{e}_{n+1}^L = \tilde{\mathbf{x}}_{n+1} - \tilde{\mathbf{x}}_{n+1}^L \quad (5.28)$$

where $\tilde{\mathbf{x}}_{n+1}$ is the exact solution of the equation (5.24), L is the number of performed iterations for the time step n+1.

To simplify calculations, we assume that there are not round-off errors generated by the algorithm, except those introduced by the initial values at time t_0 .

If we replace \mathbf{x}_{n+1} and \mathbf{x}_n in equation (5.24) by the corresponding exact values, we obtain:

$$\mathbf{A}\tilde{\mathbf{x}}_{n+1} = \mathbf{B}\tilde{\mathbf{x}}_n + \tilde{\mathbf{F}} + \mathbf{r}_{n+1} \quad (5.29)$$

where \mathbf{r}_{n+1} is the local truncation error of equation (5.24).

The calculated numerical solution \mathbf{x}_{n+1}^L satisfies equation (5.24), so we can subtract equation (5.24) written for \mathbf{x}_{n+1}^L and \mathbf{x}_n^L respectively from the equation (5.29).

This results in:

$$\mathbf{A}\mathbf{e}_{n+1}^L = \mathbf{B}\mathbf{e}_n^L + \mathbf{r}_{n+1} \quad (5.30)$$

Neither symmetry nor positive definiteness of the matrices is assumed here.

By a recursive application for the index n, we have from equation (5.29) that:

$$\begin{aligned} \mathbf{e}_{n+1}^L = & (\mathbf{AB}^{-1})_{n+1} \cdots (\mathbf{AB}^{-1})_1 \mathbf{e}_0^0 + \sum_{k=0}^{n-1} (\mathbf{AB}^{-1})_{n+1} \cdots \\ & \cdots (\mathbf{AB}^{-1})_{n+1-k} (\mathbf{A}^{-1})_{n-k} \mathbf{r}_{n-k} + (\mathbf{A}^{-1})_{n+1} \mathbf{r}_{n+1} \end{aligned} \quad (5.31)$$

The total error \mathbf{e}_{n+1}^L is influenced by the local truncation error \mathbf{r}_k , being $k \leq n+1$ and by the initial round-off error \mathbf{e}_0^0 made at the starting step, because then for $n=0$ and $L=0$:

$$\mathbf{e}_0^0 = \tilde{\mathbf{x}}_0 - \mathbf{x}_0^0 \quad (5.32)$$

where $\tilde{\mathbf{x}}_0 = \mathbf{x}_0$ is the exact solution of the equation (5.24).

Thus

$$\|\mathbf{A}^{-1}\mathbf{B}\| < 1 \quad \forall n \quad (5.33)$$

is the sufficient stability condition for applied solution procedure where $\|\cdot\|$ is the spectral norm.

The stability condition and the consistency property:

$$\mathbf{r}_k = \mathbf{O}(\Delta t^2) \quad (5.34)$$

together with the iteration convergence, indicated below, are sufficient for the above procedure to be globally convergent.

Considering the non-linearity of the system of equations (5.24) the solution is obtained with a Newton-Raphson type procedure (5.14) and (5.15).

6 Numerical results and numerical investigation of the second order work criterion

6.1 Introduction

In this chapter, the numerical results of three multiphase finite element analyses are presented and discussed: shear failure is being studied through an example of a finite element analysis of a plane strain compression test on globally undrained water saturated dense sand and isochoric grain matter (Sanavia et al. 2006), followed then by the finite element analysis of a real case study from southern Italy (Sarno-Quindici flowslide events due to rainfall, May 5-6 1998) and of an experimental slope subjected to rainfall infiltration which was carried out at the University of Padova (Lora 2015).

For the numerical simulations the geometrically linear finite element code Comes-Geo developed at the University of Padova, Italy, is used (which has been described in chapter 5) in which soils are considered as non-isothermal elasto-plastic multiphase solid porous materials, (the mathematical model has been described in chapter 4- hereafter the quasi-static case is examined neglecting grain compressibility) as developed in (Sanavia et al. 2006; Sanavia et al. 2008; Sanavia 2009) following the works of (Lewis & Schrefler 1998) and (Hassanizadeh & Gray 1979a; Hassanizadeh & Gray 1979b; Hassanizadeh & Gray 1980). The constitutive models which have been used for the mechanical behavior of the soil are: the Drucker-Prager constitutive model as developed in (Sanavia et al. 2006), and additionally for the third case, the more advanced Pastor-Zienkiewicz constitutive model (Pastor et al. 1990) has been used in the final analysis.

For the detection of the instability at the material point level, the second order work criterion (detailed in chapter 2) based on Hill's sufficient condition of stability is employed. The three different expressions of the second order work criterion developed in chapter 2 for variably saturated porous materials, are also investigated, where: the second order work is expressed in terms of effective stress, of total stress and thirdly by taking into account the hydraulic energy contribution (Buscarnera & Prisco 2012) for partially saturated soils.

The results described in the following, can be found published in (Kakogiannou et al. 2016; Kakogiannou et al. 2015).

6.2 Finite element analysis of a globally undrained dense sand sample

In this section a simulation of rapid desaturation, due to cavitation, of an initially water saturated porous media is analyzed with the finite element code Comes-Geo (Sanavia et al. 2006; Sanavia et al. 2008; Sanavia 2009). The example was previously solved by (Sanavia et al. 2006) and is re-analyzed here. It is inspired by the globally undrained plane strain biaxial compression test on water saturated dense sands where strain localization and cavitation of the pore water (change of the liquid phase to vapor) were experimentally observed (Mokni & Desrues 1998). The original contribution in this section is the use of the second order work criterion to detect the unstable material points of the domain and the prediction of the failure mechanism.

A rectangular sample of homogeneous soil (Hostun dense sand) of 34 cm height and 10 cm width (**Fig. 6.1**) has been discretized using a regular grid of 340 bi-quadratic isoparametric finite elements (with the dimension of the finite elements similar to that of the experimental shear band, to fix the width of the localized zones) with reduced Gaussian (2x2) integration scheme (widely used in localization analysis). The material is initially saturated with liquid water; hydrostatic distribution of water pressure, with the free surface located at the top of the specimen and geostatic effective stress are assumed as initial conditions. These initial conditions are obtained in Comes-Geo computing the hydro-mechanical state in equilibrium with the given boundary conditions and the gravity loads.

The boundary of the sample is impervious and adiabatic. Imposed vertical displacements are applied on the top surface with the constant velocity of 1.2 mm/s until strain localization is

observed. Vertical and horizontal displacements are constrained at the bottom surface. Plane strains and quasi-static loading conditions are assumed.

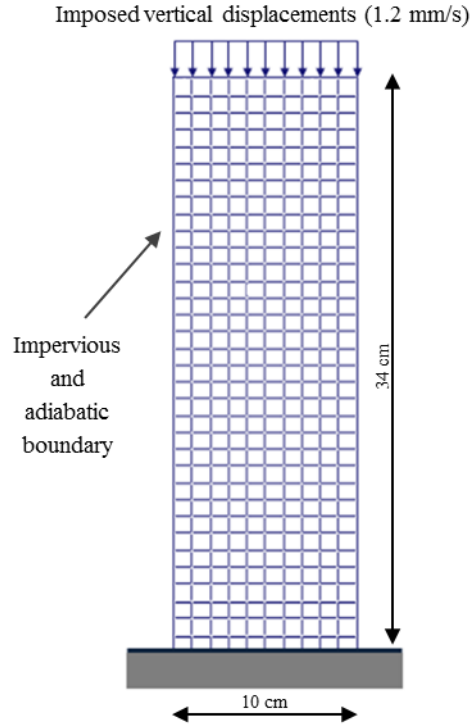


Fig. 6.1 Description of the geometry, boundary and loading conditions

The initial temperature in the sample is constant and fixed at the ambient value (i.e. 20°C). Gravity acceleration is taken into account during the computation. The mechanical behavior of the soil skeleton is described within the classical rate-independent elasto-plasticity theory for geometrically linear problems. The yield function $F(\mathbf{x}, t)$ restricting the effective stress state is assumed in the form of the Drucker-Prager yield surface with isotropic linear hardening/softening behavior and non-associated plastic flow as developed in (Sanavia et al. 2006) and is used here for the sake of simplicity:

$$F(p', \mathbf{s}', \xi) = 3\alpha_F p' + \|\mathbf{s}'\| - \beta_F \sqrt{\frac{2}{3}} [c + h\xi] \quad (6.1)$$

in which $p' = \frac{1}{3}[\boldsymbol{\sigma}' : \mathbf{1}]$ is the mean effective Cauchy stress, $\|\mathbf{s}'\|$ is the L_2 norm of the deviator effective Cauchy stress tensor $\boldsymbol{\sigma}'(\mathbf{x}, t)$, $c(\mathbf{x}, t)$ is the soil cohesion, sum of the effective cohesion $c'(\mathbf{x})$ in water saturated conditions and the apparent cohesion $p^c \tan \phi^b$, (where

$\varphi^b(\mathbf{x})$ is the internal soil friction angle associated with the capillary pressure), linked through the relation: $c = c' + p^c \tan \varphi^b$ (Fredlund et al. 1978). $\alpha_F(\mathbf{x})$ and $\beta_F(\mathbf{x})$ are two material parameters related to the internal friction angle $\varphi(\mathbf{x})$ of the soil:

$$\alpha_F = 2 \frac{\sqrt{\frac{2}{3}} \sin \varphi}{3 - \sin \varphi} \quad \beta_F = 2 \frac{6 \cos \varphi}{3 - \sin \varphi} \quad (6.2)$$

and $h(\mathbf{x})$ and $\xi(\mathbf{x}, t)$ the hardening/softening modulus and the equivalent plastic strain variable, respectively. The expression of the potential surface $Q(\mathbf{x}, t)$ is defined in (Sanavia et al. 2002) (it is similar to equation (6.1), with the parameters α and β dependent on the dilatant angle instead of the angle of internal friction used in equation (6.2)). The return mapping algorithm and the consistent tangent operator for the singular behavior of the Drucker–Prager yield surface in the apex zone are developed in (Sanavia et al. 2006) following (Sanavia et al. 2002) using the concept of multi-surface plasticity.

The material parameters used in the computation are listed in **Table 3**. In the analysis, the dilatant behavior of dense sands is simulated selecting a positive value of the angle of dilatancy ($\psi=20^\circ$).

Table 3 Material parameters assumed for dense sand (Sanavia et al. 2006)

Definition	Label	Dense sand
Solid grain density	ρ^s [kg/m ³]	2000
Young modulus	E [Pa]	3.0E+07
Poisson's ratio	ν [-]	0.4
Friction angle	φ [°]	30.0
Cohesion in water saturated conditions	c [Pa]	5.0E+05
Angle of dilatancy	ψ [°]	20
Softening modulus	h [Pa]	-1.0E+06
Hydraulic conductivity	k [m/s]	5E-7
Initial porosity	n [-]	0.2

The results of the simulation after 27 seconds of loading are presented in the following. The accumulation of plastic strains can be observed in narrow zones (shear bands) where the contour of the equivalent plastic strain (i.e. the L2 norm of the plastic strain tensor) is depicted (**Fig. 6.2a**); it can be noted that the shear bands are not centrally located in the specimen because they develop from the lower corners, which are the zones with higher stress concentration due to the initial geostatic stress, the vertical displacement load applied to the top surface and the constraints applied to the bottom surface (Sanavia et al. 2006). Other two minor shear bands develop in the upper part of the specimen. The contour of the second order work, W_2 (discretized equation (2.15)), is presented in **Fig. 6.2b**, where only the nil and negative values are plotted. As can be observed, the unstable zones ($W_2 \leq 0$) are detected inside the shear bands. Subsequently, in **Fig. 6.2c**, the positive values of the volumetric strains, which are due to the dilatant behavior of the dense sand in plasticity, are plotted and it is observed that they are also detected within the shear bands where the equivalent plastic strains are accumulated. Consequently, pore water pressure decreases, up to the development of capillary pressure (**Fig. 6.3a**).

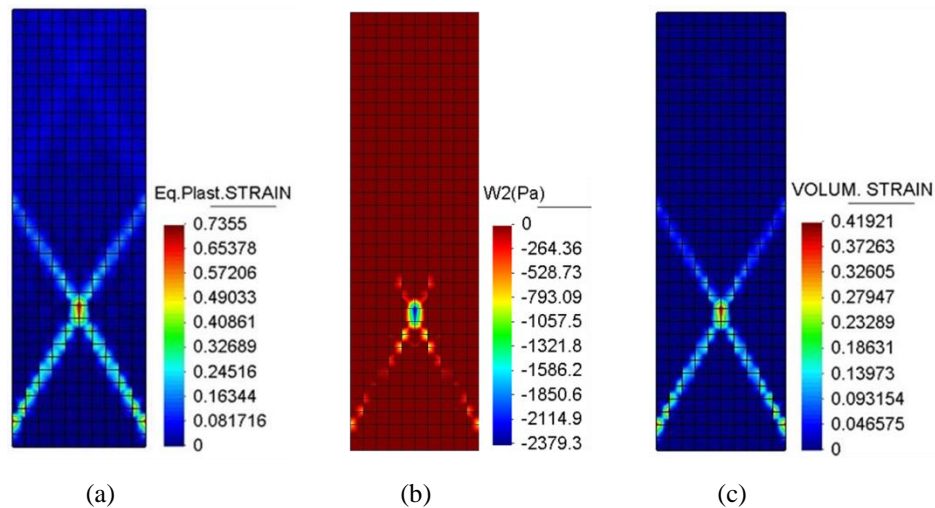


Fig. 6.2 Numerical results after 27s of loading (values plotted at the Gauss points): **a** Equivalent plastic strain contour [-]; **b** Negative values of the second order work W_2 contour [Pa]; **c** Positive values of the volumetric strain contour [-]

Subsequently, desaturation in the strain localization zones develops (**Fig. 6.3b**), as experimentally observed (Mokni & Desrues 1998), due to the formation of a vapor phase as the water pressure decreases below the water saturation pressure ($p^{gws} = 2338.8$ Pa at $T = 20^\circ\text{C}$). This effect is captured by the model, because of the coupling between the thermo-

hydro and mechanical parts, as it is shown in **Fig. 6.3c**, with the vapor phase appearing only inside the dilatant plastic zones.

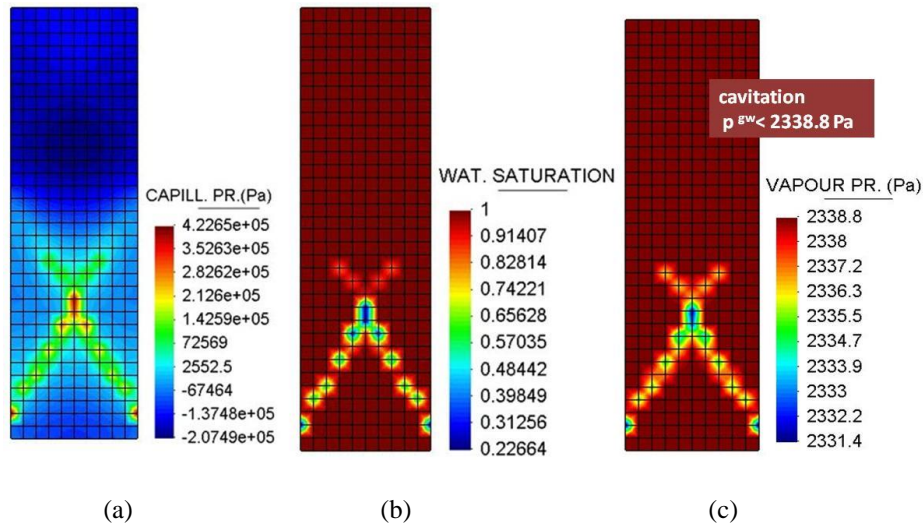


Fig. 6.3 Numerical results after 27s of loading (values plotted at the nodal points): **a** Capillary pressure contour [Pa]; **b** Water degree of saturation contour [-]; **c** Vapor pressure contour [Pa]

Finally, the contour plot of the second order work written in terms of effective stress, W_2 (equation (2.15) - **Fig. 6.2b**), is compared with the contour of the second order work written in terms of total stress, $W_{2\text{tot}}$ (equation (2.16)- **Fig. 6.4a**) and taking into account the hydraulic energy contribution, $W_{2\text{unsat}}$, (equation (2.17) - **Fig. 6.4b**). The pattern of the shear band is quite well detected in all three cases, with similar lower values, even if it is observed that the whole shear band cannot be captured (see **Fig. 6.2a**). In the case of the expression W_2 in terms of effective stress slightly more unstable points are detected and even lower values are reached according to the results.

Hereafter, the evolution of the second order work W_2 , of the water saturation degree, of the equivalent plastic strain, of the capillary pressure and the volumetric strain is presented at the Gauss points of four different elements (**Fig. 6.5**): at the center of the specimen (element 105), near the base where the shear band initiates (element 20), in the elastic zone (element 27) and at the top of the shear band (element 162, where the minimum values of the equivalent plastic strain are depicted). The location of the Gauss points is shown in **Fig. 6.5a**, within the contour of equivalent plastic strain drawn in a lower part of the specimen.

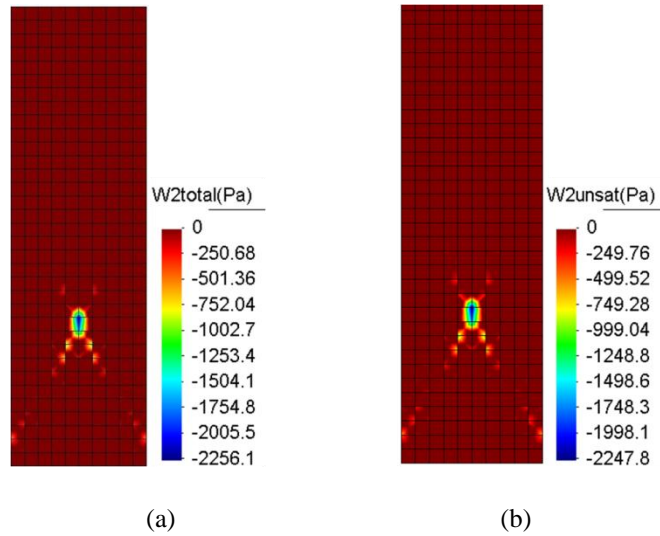


Fig. 6.4 Numerical results of the second order work [Pa] after 27s of loading (values plotted at the Gauss points): **a** in terms of total stresses W_{2tot} ; **b** expression for partially saturated soils W_{2unsat}

It is observed that the evolution of the equivalent plastic strain starts after 7 seconds of loading (**Fig. 6.5d**) and, consequently, the volumetric strain becomes positive due to the dilatant plastic behavior of the material (**Fig. 6.5f**). Negative value of the volumetric strain is observed only for the point in the elastic domain (element 27, **Fig. 6.5f**). At the same time the capillary pressure starts to increase. Positive values for the capillary pressure greater than the air entry value (equal to 2.0 kPa), which correspond to desaturation, are only obtained later on at the material points of elements 20 and 105 located within the plastic zones which cavitates (**Fig. 6.5e**). For the same elements (105 and 20) the second order work (in terms of effective stresses, W_2) at the material point level becomes negative, starting from 15s as shown in **Fig. 6.5b**, after the development of a certain amount of plastic strain.

A comparison of the results obtained from the different expressions derived for the second order work (equations (2.15) - (2.17)), at the material point of the element 105, follows in **Fig. 6.6a**. As it can be seen, the results of the three expressions are quite similar. A closer look shows that the expression of the second order work written in terms of effective stresses (W_2) and the one accounting for the partially saturated conditions (W_{2unsat}) give the same results until the point of desaturation (after 24s of loading). After that point, W_{2unsat} gives slightly higher values. The second order work in terms of total stresses (W_{2tot}) becomes zero slightly after W_2 (at 17s of loading) and obtains greater values comparing to the other two expressions.

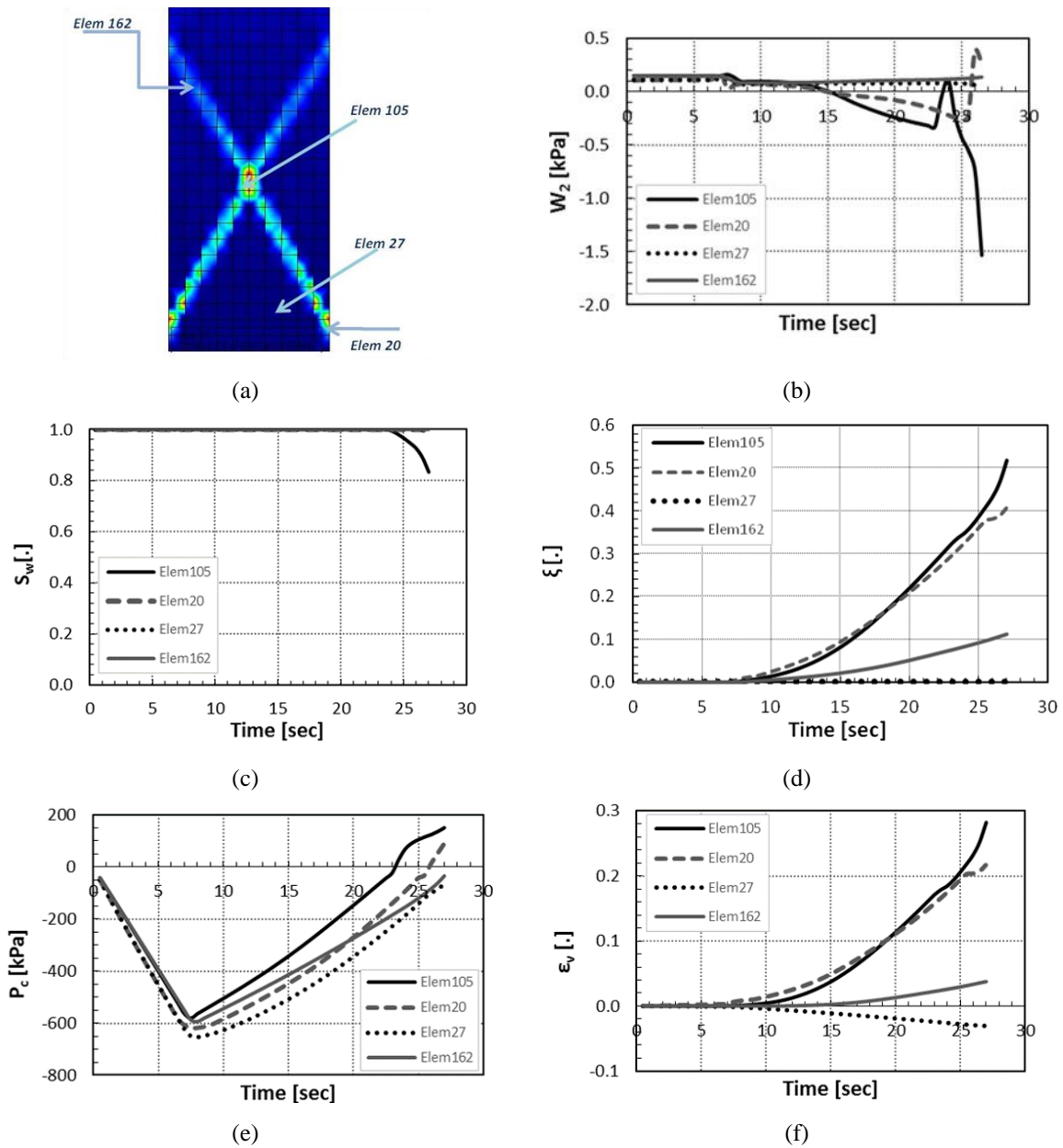


Fig. 6.5 **a** Material points location; **b** evolution of the W_2 (equation 2.15); **c** of the water saturation degree; **d** of the equivalent plastic strain; **e** of the capillary pressure; **f** of the volumetric strain, at these points

What is more important, is that the comparison with **Fig. 6.5** identifies four zones: a first stable one during the elastic behavior, a second zone in which the second order work decreases down to negative values when plasticity occurs, a third one in which the second-work increases when capillary pressure develops up to cavitation and finally, a fourth zone in which the second-work decreases rapidly because of cavitation.

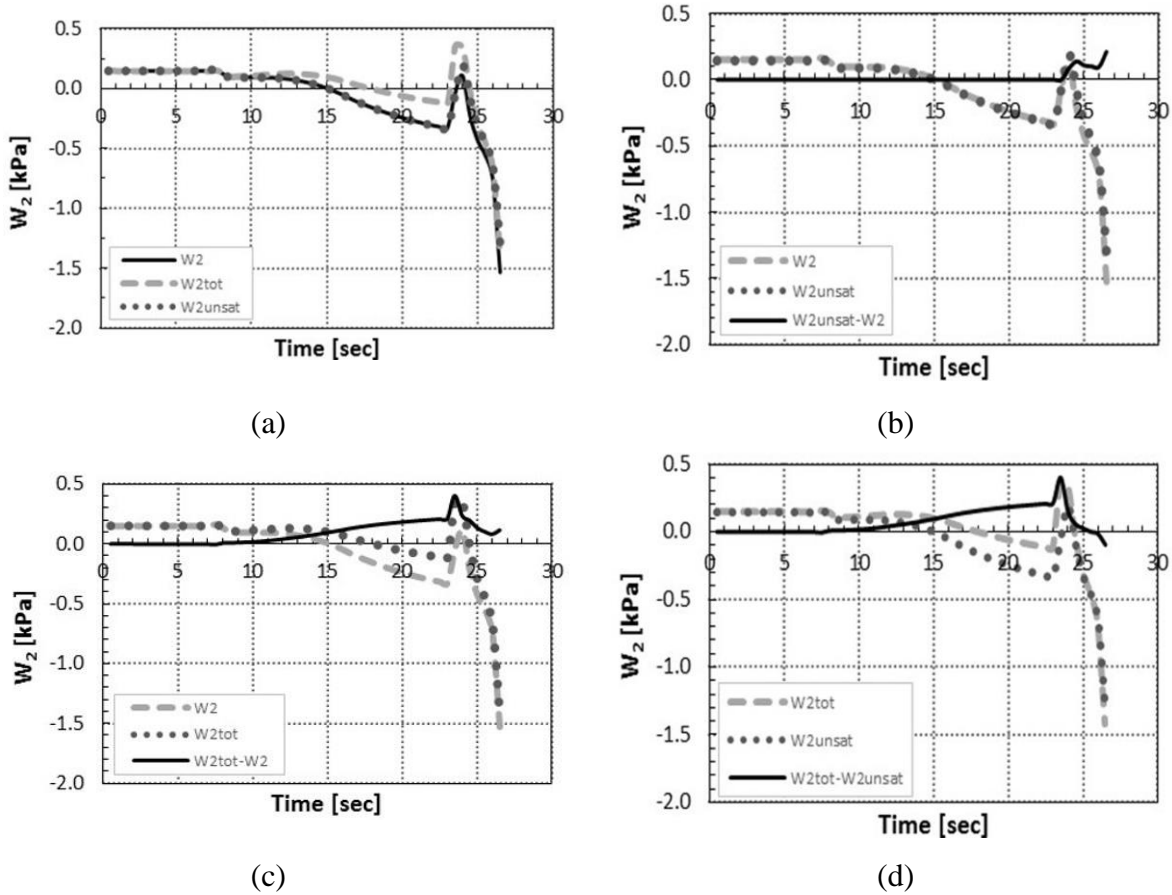


Fig. 6.6 **a** Comparison between the results obtained from the three different expressions of the second order work in the middle of the shear band; **b** evolution of the $W_{2unsat} - W_2$ difference; **c** evolution of the $W_{2tot} - W_2$ difference; **d** evolution of the $W_{2tot} - W_{2unsat}$ difference

The results of the three expressions are compared in Figures **Fig. 6.6b** and **Fig. 6.6c**, where the difference of the W_{2unsat} and of the W_{2tot} relatively to W_2 is plotted. The difference $W_{2unsat} - W_2$ (**Fig. 6.6b**) is slightly positive only after the moment of desaturation, showing that W_2 is slightly more negative than W_{2unsat} because the term $-ndp^c dS_w$ is always positive (or nil in water saturated conditions, see equation (2.17)). It is observed that also the difference $W_{2tot} - W_2$ is positive (**Fig. 6.6c**) but the time histories of the two variables are quite similar. Then, **Fig. 6.6d** compares W_{2tot} with W_{2unsat} showing similar trends of **Fig. 6.6c**.

Additionally, the von Mises constitutive model has been also tested on the same analysis. As this model is reduced from the Drucker-Prager one, equation (6.1), by setting the coefficients α_F and β_F to zero and one, respectively and assuming associated plastic flow, the values of the elasto-plastic model parameters (Young modulus, Poisson's ratio, initial yield and softening modulus) are those reported in **Table 3**.

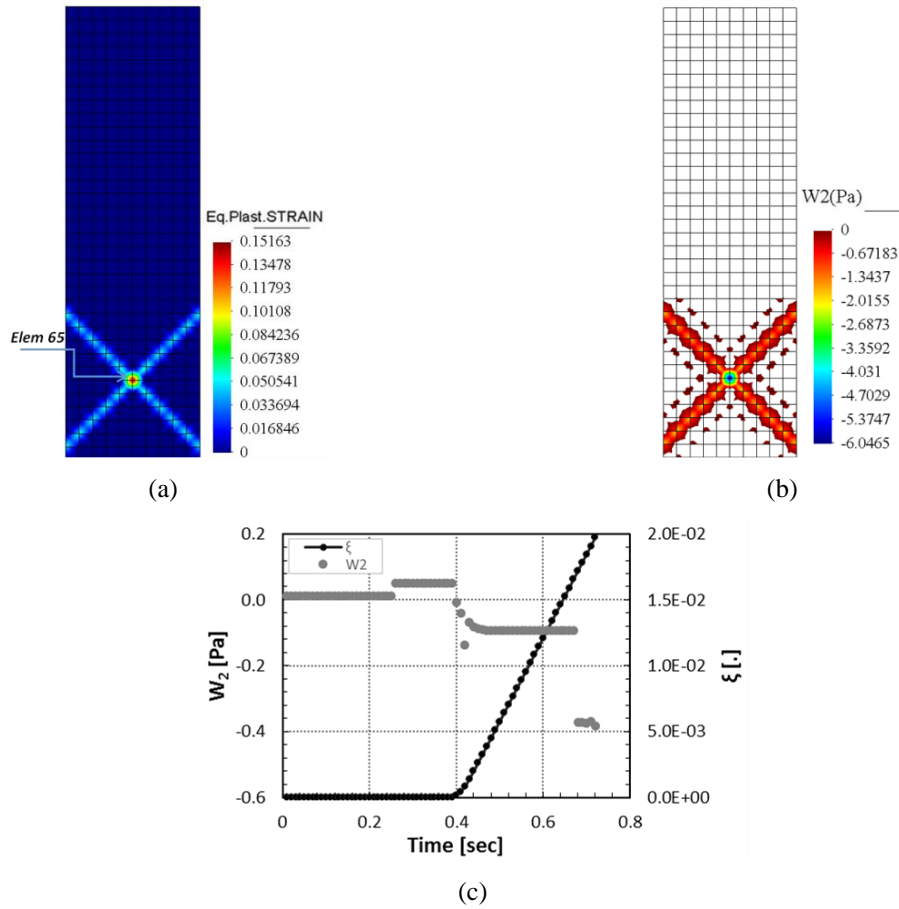


Fig. 6.7 Numerical results after 0.77 s of loading using the von Mises constitutive model: **a** equivalent plastic strain contour [.]; **b** nil and negative values of the second order work W_2 [Pa] contour; **c** evolution of the equivalent plastic strain and of W_2 in the middle of the shear band

Also the values of the parameters for the porous material (solid grain density, hydraulic conductivity and porosity) are those of **Table 3**. In this case it is observed that the second order work W_2 captures the whole shear band (**Fig. 6.7b**) and that the equivalent plastic strain starts appearing at the same time step with the first negative value of the second order work at the material point level (**Fig. 6.7c**). This is explained by the fact that von Mises plasticity considers associated plastic flow; in the case of associated plasticity, since the tangent stiffness matrix \mathbf{M} of the solid is symmetric, the second order work criterion ($\det \mathbf{M}_s = 0$) will give the same results as the limit criterion ($\det \mathbf{M} = 0$), (Darve et al. 2004).

In summary, the analysis of the strain localization test simulated in this section shows that the three expressions of the second order work (equations (2.15) - (2.17)) give similar results in terms of spatial and temporal distribution, especially for W_2 and $W_{2\text{unsat}}$.

Moreover, the second order work criterion is able to capture the instability induced by cavitation of the pore water. The comparison between the results obtained from the Drucker Prager and the von Mises constitutive model evidences the role of the volumetric plasticity, which delays instability up to the development of a certain amount of plastic strains, because the first indication of instability (negative second order work) is obtained later than the beginning of the plastic strains.

6.3 Finite element analysis of the Sarno flowslide

At the beginning of May 1998, landslides of the flow-type occurred along the slopes of the Pizzo d’Alvano carbonate massif (Campania region, southern Italy) because of a severe rainfall event throughout the area (Cascini 2004; Cascini et al. 2008). The case addressed in this section occurred on May 5-6 1998 and constitutes one of these hundred slope instability events. In the sample area shown in **Fig. 6.8**, the section A-A has been analyzed which is of 400 m length, with a variable thickness between 2 and 5 m and composed by 3 type of materials: upper ash, pumice and lower ash.

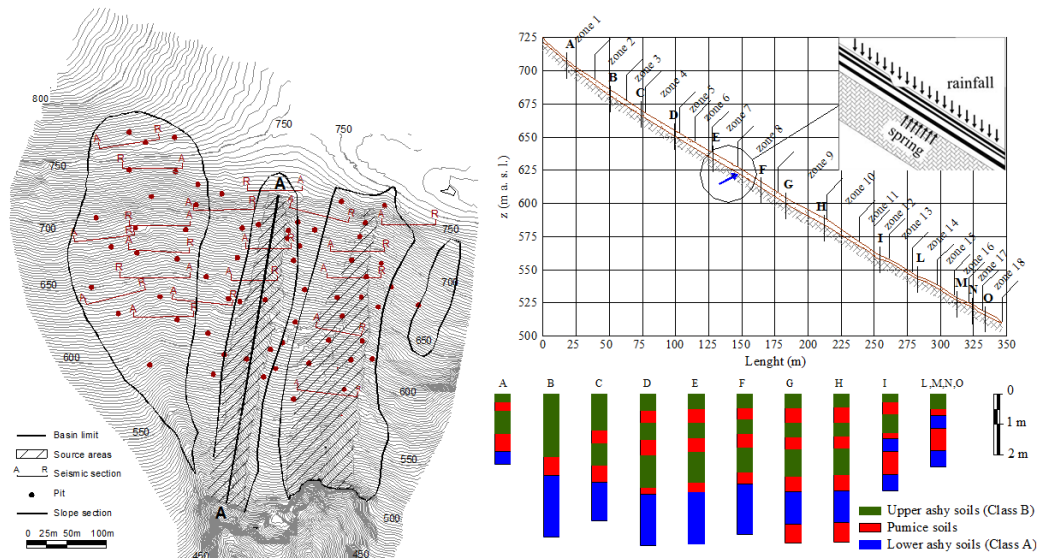


Fig. 6.8 Field site plan- geometry and stratigraphy of the section A-A (Cascini et al. 2008)

The mechanical behavior of the solid skeleton is simulated also in this case by using the elasto-plastic Drucker-Prager constitutive model with isotropic linear softening behavior and non-associated plastic flow, as described in section 6.2. The values of the mechanical and hydraulic properties of each material layer which were used in the analysis are summarized in **Table 4**. These values were selected in agreement with (Sorbino & Foresta 2002; Bilotta et al. 2005). From the list of the material parameters, we can deduce that the pumice layers should be the first collapsible layers because of the lower value of cohesion in water saturated condition and Young modulus; they are also those with the higher permeability and hence the

liquid water infiltrated with the rainfall and from the bedrock will penetrate easier and faster in the pumice layers, reducing their cohesion in unsaturated condition.

Table 4 Geotechnical characterization of soil layers

Definition	Label	Lower Ashy	Upper Ashy	Pumice
Solid grain density	ρ^s [kg/m ³]	2393	2169	2039
Young modulus	E [Pa]	5E+05	4E+05	2E+05
Poisson's ratio	ν [-]	0.316	0.294	0.30
Friction angle	ϕ [°]	32.0	36.0	37.0
Friction angle associated with capillary pressure	ϕ^b [°]	25.0	25.0	25.0
Cohesion in water saturated conditions	c [Pa]	4.7E+03	4.7E+03	3.3E+02
Angle of dilatancy	ψ [°]	-4.75	-5.5	5
Softening modulus	h [Pa]	6.5E+04	8.0E+04	1.1E+04
Hydraulic conductivity	k [m/s]	1E-06	1E-05	1E-04
Initial porosity	n [-]	0.664	0.584	0.69

The rain-gauges located at the toe of Pizzo d'Alvano massif recorded a cumulated rainfall value of more than 160 mm, for the period April 27 – May 5, 1998. The daily rainfall for the analyzed period is shown in **Fig. 6.9**. However, according to (Cascini et al. 2003) the cumulated rainfall must have been higher than the one measured at the toe, as the rain gauges which were installed at the top of the massif frequently gave higher values.

For the discretization of the geometry of the slope (**Fig. 6.8**) a rather coarse mesh has been used (as shown in **Fig. 6.10**), composed of 1565 nodes and 480 eight node quadrilateral isoparametric elements with a Gaussian integration of 3x3 order. In **Fig. 6.10b** the elements at toe are presented as an example of the spatial discretization adopted in the computation; the size of these elements are variable in the range 0.11-0.34 m in height and about 9m in length. This choice, with high aspect ratio, was made on the base of reducing the computational cost (min 2h – max 52h/day of rain) and because the hydro-mechanical behavior (water flux and displacements) develops mainly along the axial direction (moreover, it is also observed that

the numerical solution is convergent and consistent with the flowslides observed in situ, as described below in this section). When meshing the geometry of the stratigraphic section of **Fig. 6.8**, the toe of the slope was cut with a vertical side to avoid the generation of highly distorted finite elements in the toe region (see **Fig. 6.10c**).

Vertical and horizontal displacements are constrained at the bottom surface, which is also assumed impervious. The vertical boundary at toe of the discretized domain is not constrained to displacements, because it can move with the deformation of the slope, as can be seen in the **Fig. 6.10c**, and, similarly, it is assumed impervious because the water flow at toe at the occurrence of the flowslide is unknown. This condition is realistic up to the saturation of the thickness of the slope at toe; then, when the condition of water saturation is reached, it overestimates the liquid water accumulation at toe and represents an upper bound for the numerical solution.

This choice can be reasonable as a first approximation and influences the numerical solution only during the 8th day of rain; during this period, the failure at toe of the slope was observed in situ. In fact, the numerical computation shows that: (i) the displacement of the vertical boundary at toe of the mesh remains very small and the behavior of the materials up to the first third of the 8th day of rain remains in the elastic regime (**Fig. 6.17a**); (ii) the saturation of the thickness at toe occurs during the 8th day of rain (**Fig. 6.18b**) at which, simultaneously, the computed displacements increase continuously with high rate (**Fig. 6.17a**).

As a first step of the simulation, the stress state is computed in equilibrium with the gravity load, the boundary conditions and the initial hydro-thermal conditions (**Fig. 6.11**), which, because of the low thickness of the slope, are a uniform capillary pressure of 10kPa (reasonable

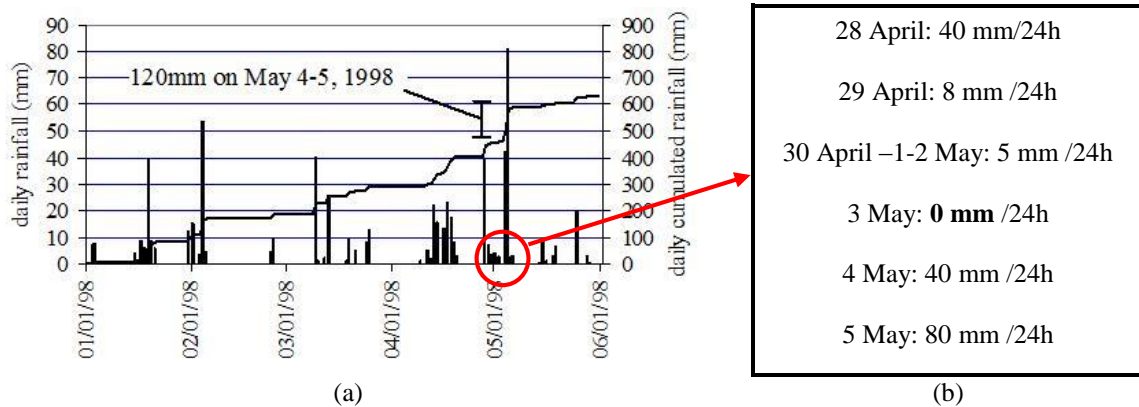


Fig. 6.9 a Rainfall recorded at the toe of Pizzo d'Alvano massif (Cascini et al. 2003); b Rainfall loading function on the upper surface

value for the slope in the days before the rainfall, which were not rainy – see **Fig. 6.9a**), a uniform gas pressure at atmospheric value of 101.325 kPa and a uniform temperature at ambient value of 293.15 K.

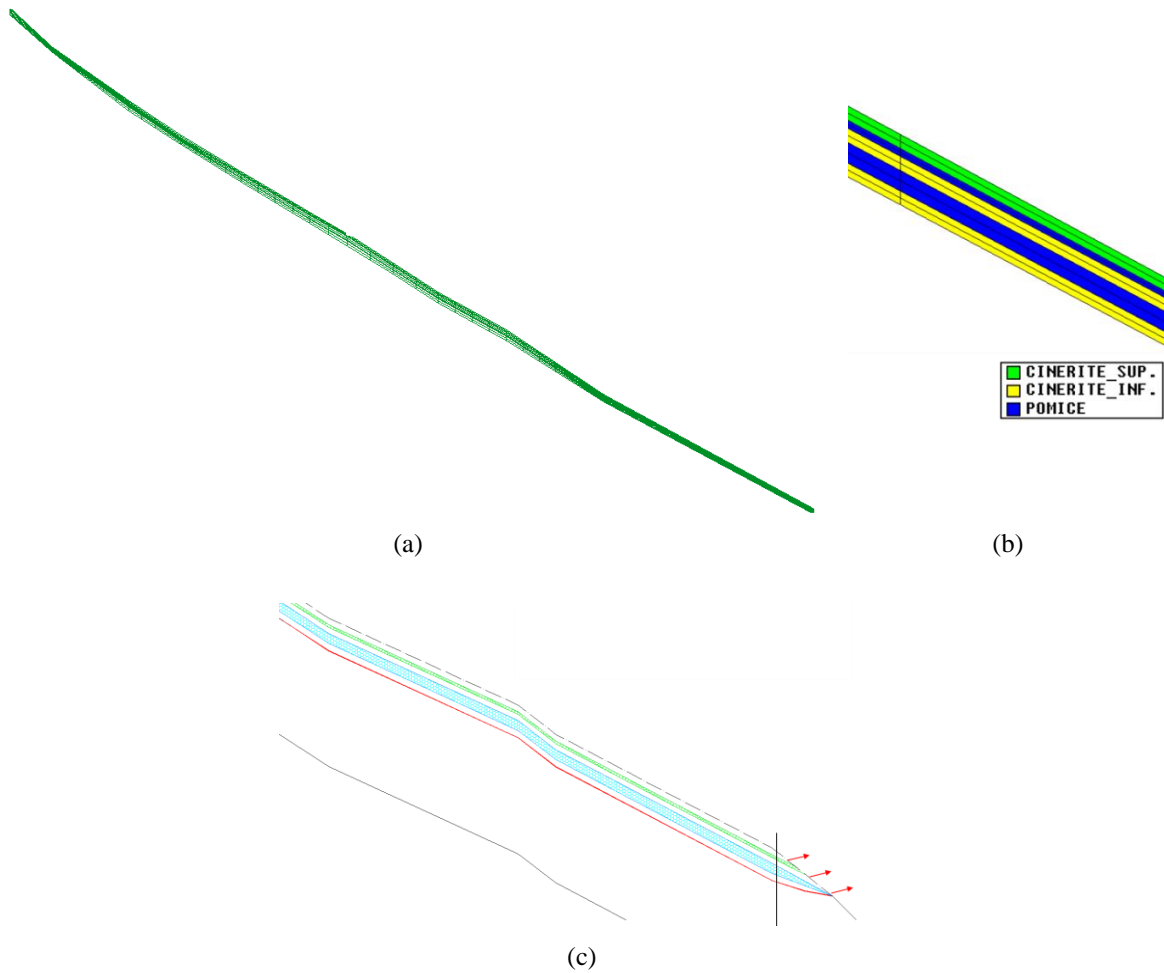


Fig. 6.10 **a** Discretisation of the section A-A; **b** finite element discretization at the basis of the slope; **c** stratigraphic section of the slope at toe. The vertical line indicates the vertical boundary of the mesh at toe (figure 6.10b)

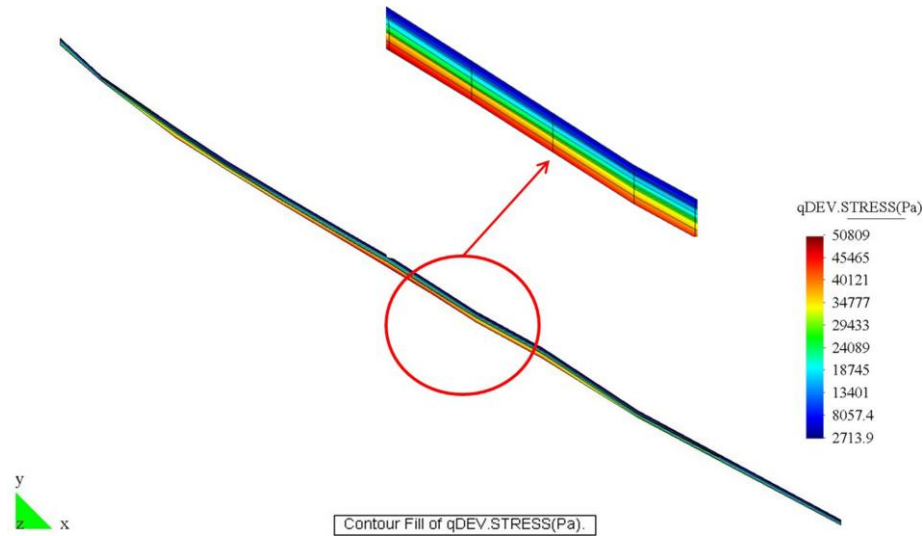


Fig. 6.11 Distribution of the deviatoric stress after the equilibrium with the initial and boundary hydro-thermal conditions

After applying the rainfall load history, the results at the end of May 6 are presented below. In **Fig. 6.12** it is observed that the displacements are mainly concentrated at the lower part of the slope (near the toe, affecting a zone of 15m length), with a maximum value of about 2 m.

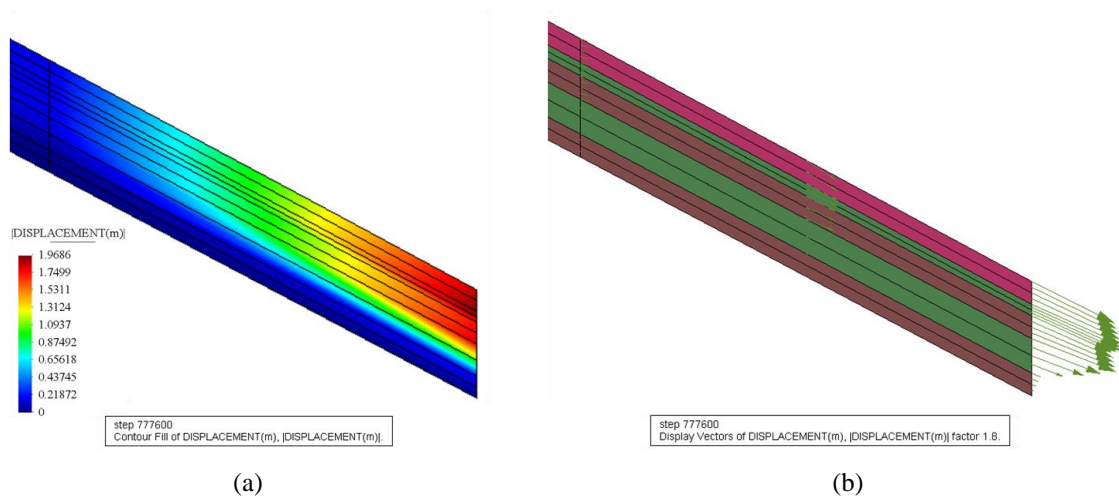


Fig. 6.12 a Displacement contour [m]; **b** displacement vectors at the end of May 6 (lower part of the slope)

The displacements are due to the accumulation of the plastic strain at the toe, as it is presented in the contour plot of the equivalent plastic strain variable on **Fig. 6.13**. In particular, as it was expected, the higher values are detected within the pumice layers which are the less resistant and the most permeable. The extent of the plastic zone and of the zone of displacements coincides with the zone of the increased degree of saturation thus showing clearly the localized effect of the infiltrated water.

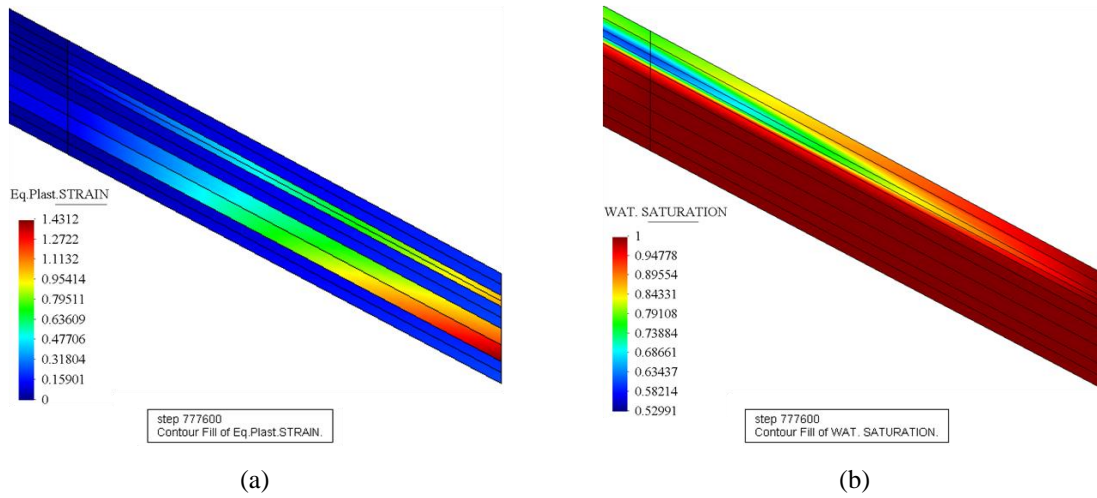


Fig. 6.13 a Equivalent plastic strain [-]; b water saturation [-] contour at the end of May 6 (lower part of the slope)

Apart from the localized effect at the lower portion of the slope, where the upslope groundwater flow is collected, the multiphase analysis reveals also the effect of the temporary spring from the bedrock observed after the event (Cascini et al. 2000). To this end, a flux condition was imposed at the basis of the pyroclastic deposits (**Fig. 6.8**, central part of the slope) with a volumetric inflow rate equal to $2.893 \text{ m}^3/\text{s}$ from May 2.

The results presented in Figures **Fig. 6.14-Fig. 6.15** at the end of May 5 highlight the important role of the local water circulation inside the bedrock showing, in particular, that the area around the spring zone has been saturated (**Fig. 6.15b**), causing loss of soil strength and development of plastic strains at the base of the pyroclastic soils (**Fig. 6.15a**). This leads to the increase of the displacements (**Fig. 6.14a, b**), sliding and instabilizing this zone (**Fig. 6.15a, c**, respectively) earlier than at the toe, as observed in situ during the flowslide events. These results are confirmed by the analysis of the W_2 value (equation (2.15)) showing that the strongest indication of W_2 at the outlet occurs five hours before the toe (the white regions in **Fig. 6.15c** represent zones with value of W_2 larger than $-1.0\text{E}-10 \text{ Pa}$).

In order to understand better the main failure mechanism at the toe of the slope, we present hereafter the evolution of the above contour quantities in time, as this was captured on the different nodes (**Fig. 6.16**).

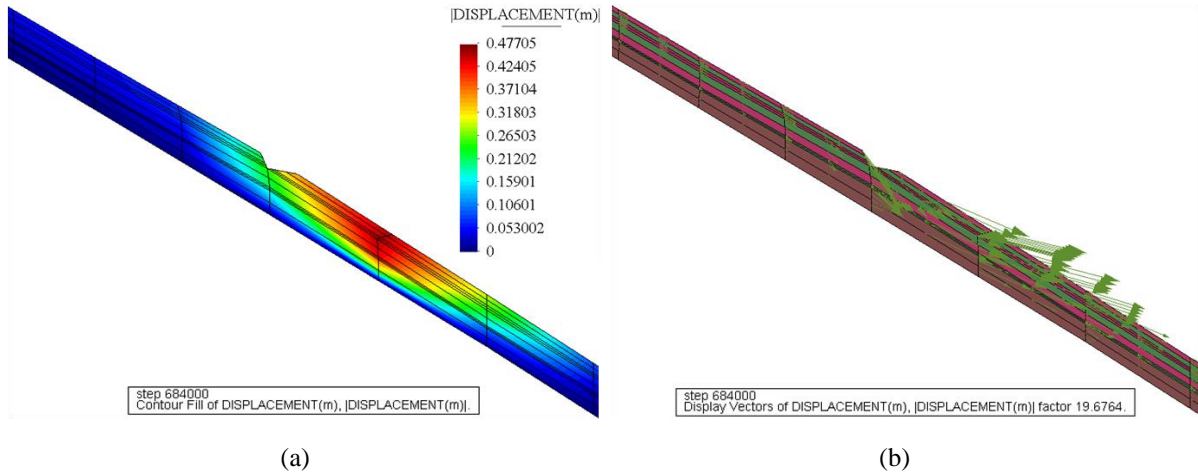


Fig. 6.14 a Displacement contour [m]; b displacement vectors at the end of May 5 (spring zone)

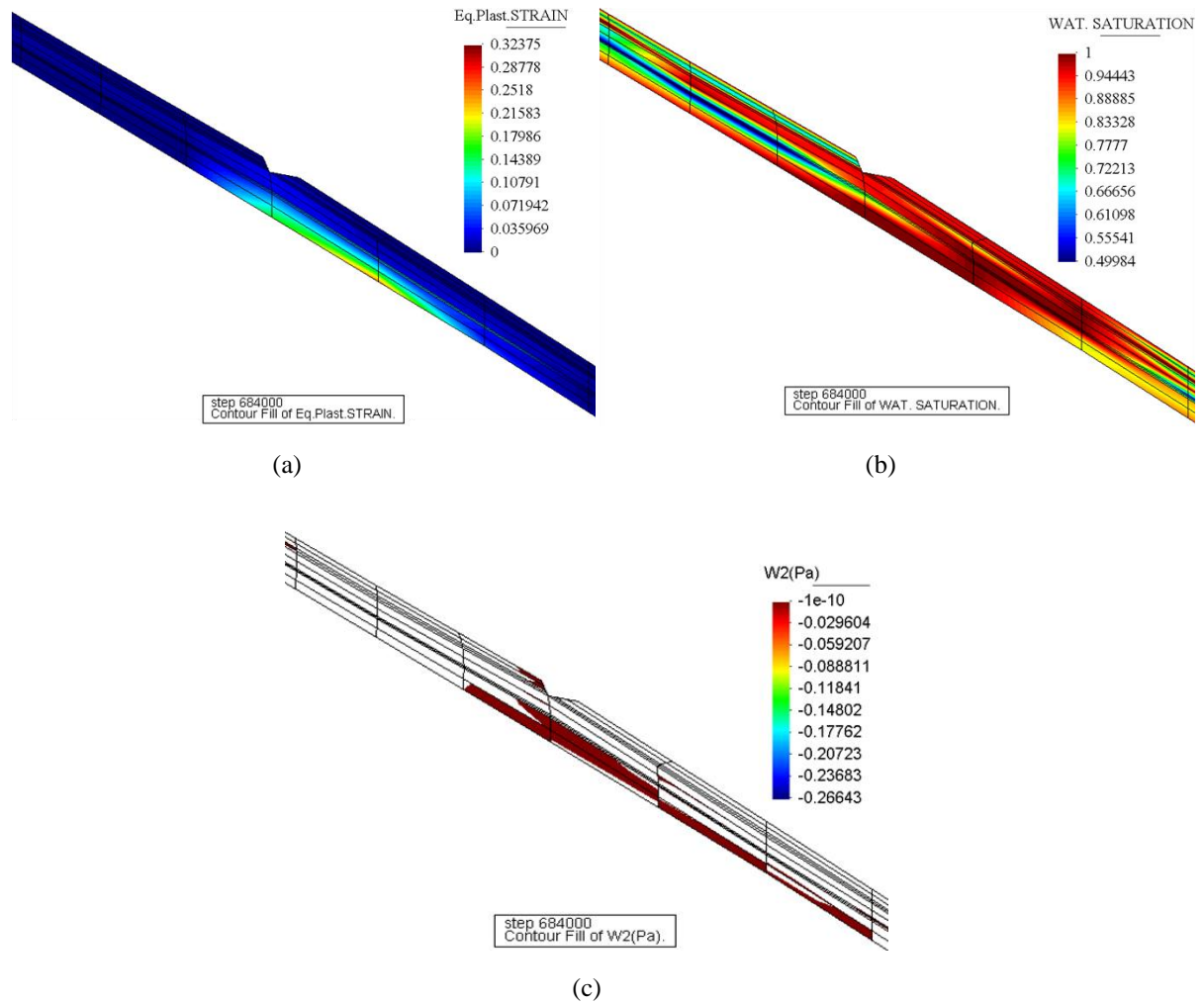


Fig. 6.15 a Equivalent plastic strain [-] contour; b water saturation [-] contour; c second order work W_2 [Pa] contour at the end of May 5 (spring zone)

The calculated surface displacements, which are displayed on **Fig. 6.17a**, indicate a strong and continuous increase in nodal displacements during the 8th day of rain infiltration (May 6th) when the slope approaches failure. At the same time large irreversible deformations occur at the toe of the slope with the largest values to be detected on the layers of the pumice (nodes 7, 15) as expected due to its low strength.

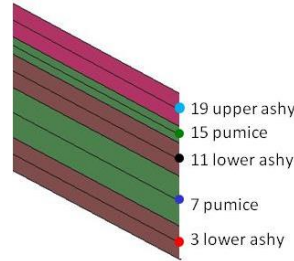


Fig. 6.16 Node location for the analysis at the lower part of the slope

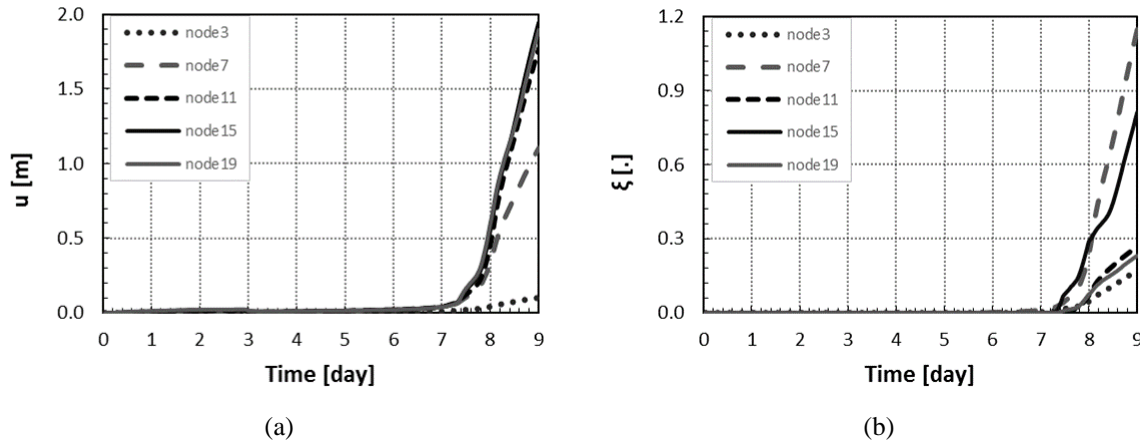


Fig. 6.17 a Evolution of the displacements [m]; **b** the equivalent plastic strain [-] at the lower part of the slope

The contour of the equivalent plastic strain at the moment of failure is mainly due to the fact that by that time this zone has become fully saturated as it can be observed from the **Fig. 6.18a**. The evolution of the water table starts from the bottom on the 4th day (node3) until it reaches the surface layers (nodes 19, 15) at the beginning of the 8th day.

This allows us to understand and analyze the mechanical response of the slope to rain infiltration: with increasing water content, the capillary forces acting between the soil particles decrease up to saturation of the pores (**Fig. 6.18a**) and pore water pressure develops (**Fig. 6.18b**). This de-bonding effect of wetting is taken into account in the model through the

effective stress in the form $\sigma' = \sigma + [p^s - S^w p^c] \mathbf{1}$ (Schrefler 1984), which decreases during rain infiltration and as a consequence the soil reduces its strength. When the point of significant excess pore water development is reached, there be little or no effective confining stress acting on the soil and the soil state may approach a zone of instability in which the shear strength decreases.

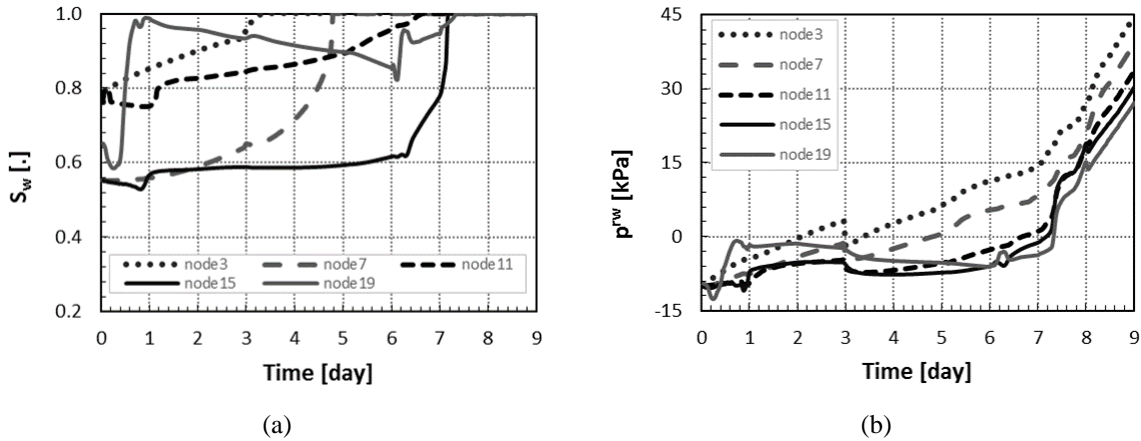


Fig. 6.18 a Evolution of the water saturation [-]; b the relative water pressure [kPa] at the lower part of the slope

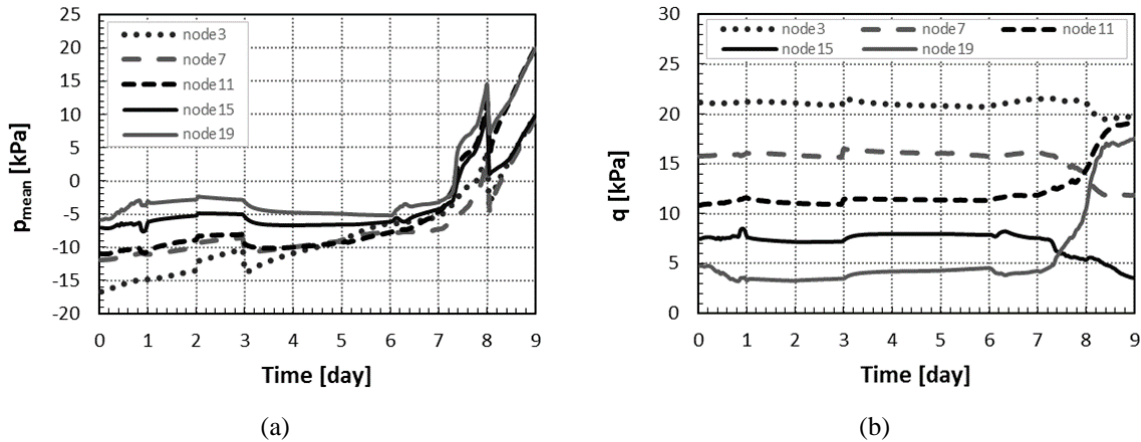


Fig. 6.19 a Evolution of the mean stress [kPa]; b deviatoric stress [kPa] at the lower part of the slope

Figures **Fig. 6.19a, b** describe this phenomenon in particular in the pumice layers (nodes 7 and 15), where it is observed that the capillary pressure (negative relative water pressure) vanishes up to the development of liquid water pressure (**Fig. 6.18b**), the mean pressure decreases down to zero and the deviatoric stress starts to decrease, suggesting a probable achievement of liquefaction (this state is then not described by the Drucker-Prager constitutive model adopted in this simulation because the loss of stiffness due to liquefaction is not modeled

and the mean pressure starts to increase – **Fig. 6.19a**). This point would merit further investigation using a more advanced constitutive model able to describe the liquefaction state in soils both at stress and at stiffness level (e.g. the Pastor-Zienkiewicz model (Pastor et al. 1990) and its extension to variably saturated conditions, (Bolzon et al. 1996; Manzanal et al. 2011)).

As far as the results of the second order work W_2 are concerned, at the beginning of May 6 (8th day) we have the strongest indication of instability at the toe as shown on the **Fig. 6.20a**. The negative values are concentrated in the pumice layers, at the upper ashly soil and at the base of the toe affecting a zone of about 21m in length.

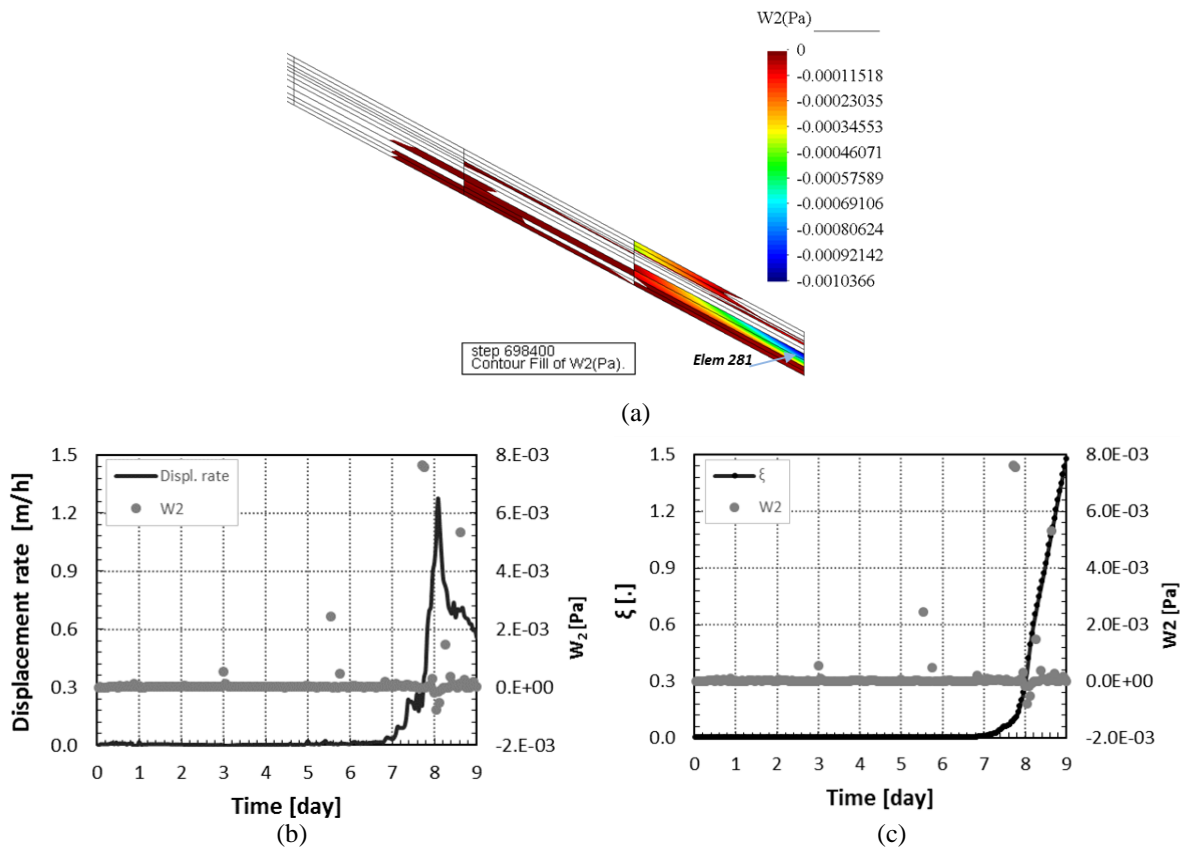


Fig. 6.20 a Second order work contour in terms of effective stresses at the beginning of May 6th (lower part of the slope); Comparison between the evolution of the second order work W_2 and the displacement rate **b**; and the equivalent plastic strain **c**, at the material point level in the lower pumice layer at toe

In Figures **Fig. 6.20b** and **Fig. 6.20c** the evolution of the second order work W_2 (equation (2.15)) is plotted in comparison with the evolution of the displacement rate and of the equivalent plastic strain at the material point level of the lower pumice layer (a gauss point of

element 281, **Fig. 6.20a**, close to node 7 in the lower pumice layer, **Fig. 6.16**). It is observed that the second order work W_2 becomes negative during the sharp increase of the displacement rate (**Fig. 6.20b**) and the continuous development of plastic strain (**Fig. 6.20c**) and displacement (**Fig. 6.17a**). This behavior is observed also in other points, e.g. in a Gauss point at 4.5m on the left of node 7. Few points of **Fig. 6.20b-c** deviate from the averaged interpolation line of the numerical results, but the general trend is not modified. It is observed also in the analysis of this section that the indication of the potential local instability from the W_2 comes later (difference of almost one day) than the beginning of plastic strains development, similarly to what is observed for the strain localization test. It can be also seen that the contour plot area of negative second order work (**Fig. 6.20a**) coincides with that of the equivalent plastic strain at the toe of the slope (**Fig. 6.13a**) and the magnitude is greater than that corresponding to high displacements (**Fig. 6.12a**).

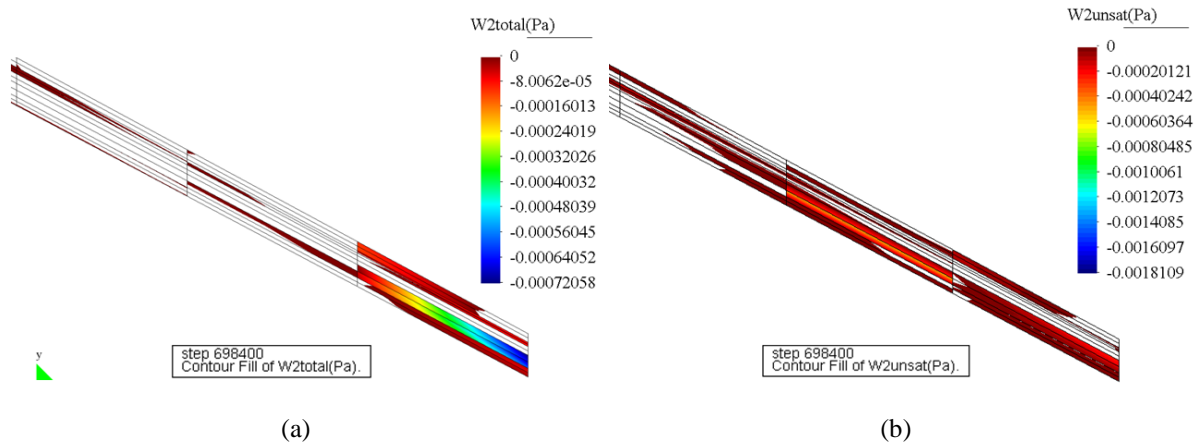


Fig. 6.21 Second order work contour at the beginning of May 6th (lower part of the slope): **a** in terms total stresses, W_{2tot} ; **b** expression for partially saturated soils, W_{2unsat}

Finally, the numerical results of the second order work W_{2tot} and W_{2unsat} as expressed from equations (2.16) and (2.17), respectively, are presented in **Fig. 6.21**. When compared with the contour plot of the second order work in terms of effective stresses W_2 (**Fig. 6.20a**) it can be observed that the results of all the expressions are similar, especially for the part of the slope which is saturated, with a greater extent for the W_{2unsat} variable (**Fig. 6.21b**). The comparison of the values between them shows that they are slightly different, with the expression of the

second order work accounting for the partially saturated conditions ($W_{2\text{unsat}}$) to be giving lower values.

6.4 Finite element analysis of an experimental slope

The experiment which was carried out in the University of Padua (Lora 2015), (Lora et al. 2016a; Lora et al. 2016b) reproduces a stability problem of a large-scale slope due to rain infiltration.

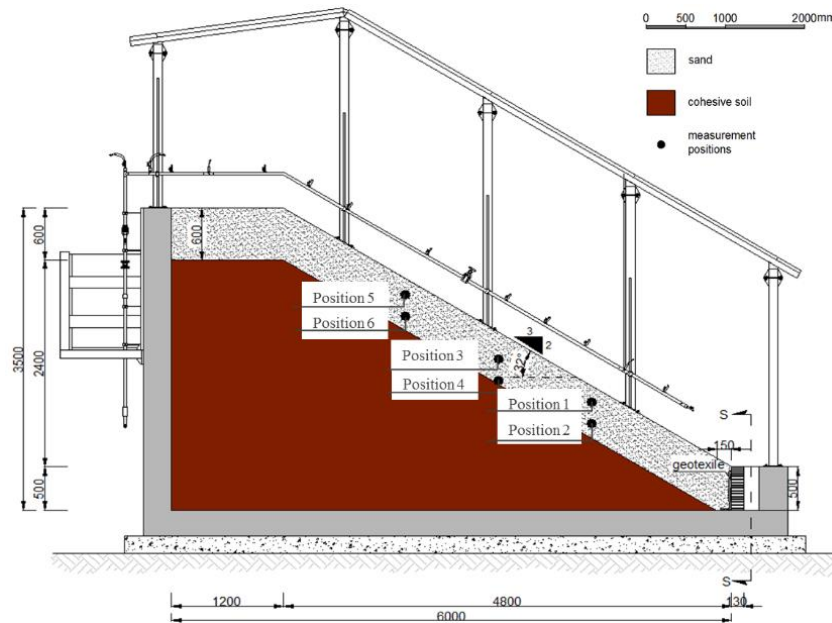


Fig. 6.22 Geometry and stratigraphy of the slope (longitudinal section) and representation of the measurement positions (Lora 2015)

To this end, a steady rainfall intensity equal to 150mm/h is applied until the mobilization of the soil. The slope consists of two soil layers: a shallow permeable layer of loose sand overlying a dense clayey soil substratum. The height varies linearly from 3.5m to 0.5m, such that a sloping angle of 32° can be assigned to the soil. The dimensions of the model and the stratigraphy are presented in **Fig. 6.22**. The values of the mechanical properties of each material layer, which were used in the computation when the Drucker-Prager model is employed, are presented in **Table 5**.

The Pastor-Zienkiewicz constitutive model (Pastor et al. 1990), which is developed within the framework of the Generalized Plasticity (Zienkiewicz & Mroz 1984), is additionally employed for the description of the mechanical behaviour of the loose sand layer.

Table 5 Soil parameters used in the computation for the DP model

Definition	Label	Loose Sand	Clay
Density	ρ^s [kg/m ³]	2718	2680
Friction angle	ϕ [°]	34.0	22.0
Cohesion	c [Pa]	1.0E+03	1.0E+04
Initial Young modulus	E [Pa]	2.5E+06	1.0E+07
Poisson's ratio	ν [-]	0.3	0.3
Angle of dilatancy	ψ [°]	0	4
Hardening modulus	h [Pa]	4.8E+03	0.0
Initial porosity	n [-]	0.569	0.384

Generalized Plasticity Theory introduces the dependence of the constitutive tensor relating increments of stress and strain on the direction of the increment of stress via a unit tensor \mathbf{n} which discriminates the states of loading (L) and unloading (U):

$$d\boldsymbol{\varepsilon} = \mathbf{C}^L : d\boldsymbol{\sigma}, \quad \mathbf{n} : d\boldsymbol{\sigma}^e > 0 \rightarrow \text{loading} \quad (6.3)$$

$$d\boldsymbol{\varepsilon} = \mathbf{C}^U : d\boldsymbol{\sigma}, \quad \mathbf{n} : d\boldsymbol{\sigma}^e < 0 \rightarrow \text{unloading} \quad (6.4)$$

where $d\boldsymbol{\sigma}^e$ is the elastic stress increment obtained if the material behaved elastically, $d\boldsymbol{\sigma}^e = \mathbf{D}^e : d\boldsymbol{\varepsilon}$ and \mathbf{D}^e is the elastic constitutive tensor. The neutral loading corresponds to the limit case for which $\mathbf{n} : d\boldsymbol{\sigma}^e = 0$.

After imposing the condition between loading and unloading states, we arrive to :

$$\begin{aligned} \mathbf{C}^L &= \mathbf{C}^e + \frac{1}{H_L} \mathbf{n}_{gL} \otimes \mathbf{n} \\ \mathbf{C}^U &= \mathbf{C}^e + \frac{1}{H_U} \mathbf{n}_{gU} \otimes \mathbf{n} \end{aligned} \quad (6.5)$$

where \mathbf{C}^e is a fourth order tensor characterising the elastic behavior of the material, $H_{L/U}$ are two scalar functions defined as loading (L) and unloading (U) plastic modulus and $\mathbf{n}_{gL/U}$ are two unit tensors defining the plastic flow direction in loading (L) and unloading (U).

From equation (6.5) it follows that the total strain increments can be divided into elastic and plastic components as:

$$\begin{aligned}
d\boldsymbol{\varepsilon} &= d\boldsymbol{\varepsilon}^e + d\boldsymbol{\varepsilon}^p \\
d\boldsymbol{\varepsilon}^e &= \mathbf{C}^e : d\boldsymbol{\sigma}, \quad d\boldsymbol{\varepsilon}^p = \frac{1}{H_{L/U}} (\mathbf{n}_{gL/U} \otimes \mathbf{n}) : d\boldsymbol{\sigma}
\end{aligned} \tag{6.6}$$

The main advantage of Generalised Plasticity Theory is that all ingredients can be postulated without introducing any yield or plastic potential surface.

The Pastor-Zienkiewicz constitutive model (Pastor et al. 1990), in the following referred as PZ model, suitably defines the three directions \mathbf{n} , \mathbf{n}_{gL} , \mathbf{n}_{gU} and the scalar functions $H_{L/U}$ to reproduce the main aspects of sand behavior.

Starting with the definition of the elastic components of the strain increment, expressed in the space of invariants p , q , θ , the model introduces two elastic moduli \mathbf{K}^e and \mathbf{G}^e dependent on the confining pressure as:

$$d\boldsymbol{\varepsilon}_v^e = \frac{dp'}{\mathbf{K}^e}, \quad \text{where } \mathbf{K}^e = \mathbf{K}_0^e \frac{p'}{p_0} \tag{6.7}$$

$$d\boldsymbol{\varepsilon}_s^e = \frac{dq}{3\mathbf{G}^e}, \quad \text{where } \mathbf{G}^e = \mathbf{G}_0^e \frac{p'}{p_0} \tag{6.8}$$

The elements characterizing the plastic strain increment $d\boldsymbol{\varepsilon}^p$ are defined in a simple manner as follows. First of all, the direction of the plastic flow is expressed in function of dilatancy as:

$$\begin{aligned}
\mathbf{n}_{gT} &= (\mathbf{n}_{gv}, \mathbf{n}_{gs}) \\
\mathbf{n}_{gv} &= d_g / (1 + d_g^2)^{1/2} \\
\mathbf{n}_{gs} &= 1 / (1 + d_g^2)^{1/2}
\end{aligned} \tag{6.9}$$

where the dilatancy d_g which is defined as the ratio between the increments of plastic volumetric and shear strain is given by:

$$d_g = (1+a)(M_g - \eta) \tag{6.10}$$

In the above M_g is the critical state line (CSL) in the q - p' space and a is a constant of the material determined from the d_g - η plot.

The expression of dilatancy in the previous equation for $\eta = M_g$ is $d_g = 0$ fulfilling one of the basic premises of the Critical State Theory.

The loading-unloading direction given by the unit vector \mathbf{n} is obtained in a similar way:

$$\begin{aligned}\mathbf{n}^T &= (\mathbf{n}_v, \mathbf{n}_s) \\ \mathbf{n}_v &= d_f / (1 + d_f^2)^{1/2} \\ \mathbf{n}_s &= 1 / (1 + d_f^2)^{1/2}\end{aligned}\quad (6.11)$$

where $d_f = (1 + a)(M_f - \eta)$.

It is important to note that the associative behavior can be recovered by choosing $M_g = M_f$. The third ingredient is the plastic modulus, which was postulated directly without introducing any hardening law and consistency condition as:

$$H_L = H_0 \cdot p' \cdot H_{DM} \cdot f(\eta) \quad \text{where } f(\eta) = H_f \cdot [H_v + H_s] \quad (6.12)$$

$$H_f = \left(1 - \frac{\eta}{\eta_f}\right)^4, \quad H_v = \left(1 - \frac{\eta}{M_g}\right), \quad H_s = \beta_1 \cdot e^{(-\beta_0 \cdot \xi_{dev})} \quad (6.13)$$

$$\eta_f = \left(1 + \frac{\eta}{\alpha}\right) \cdot M_f \quad (6.14)$$

$$H_{DM} = \left(\frac{\zeta_{max}}{\zeta}\right) \quad \text{and } \zeta = p' \cdot \left[1 - \left(\frac{a}{1+a}\right) \cdot \frac{\eta}{M_f}\right]^{-1/a} \quad (6.15)$$

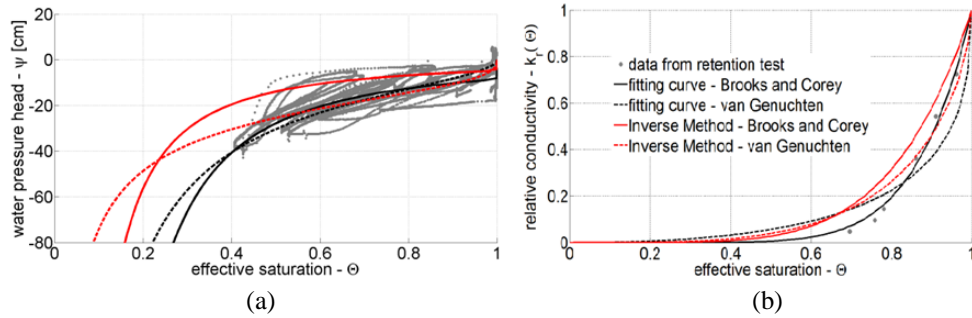
where ξ_{dev} is the accumulated shear plastic deformation, H_0 is a multiplying factor related to plastic strains at the beginning of the loading process, H_v, H_s refer respectively to volumetric and deviatoric strain hardening, H_{DM} is a function which incorporates material memory in a simple manner, η_f defines an asymmetric cone in the space of stress invariants which acts as a limit between admissible internal states and impossible external states and $\gamma, a, \beta_1, \beta_0$ are material parameters assumed to be constant during loading process.

The values of the mechanical properties that were used for this model are presented in **Table 6**.

Table 6 Additional soil parameters (Bahda 1997) used in the computation with the PZ model

Parameters	Loose Sand
M_f [-]	0.569
M_g [-]	1.35
a [-]	0.45
β_0 [-]	2.25
β_1 [-]	0.2
H_0 [-]	4000

The estimates of the retention functions for the loose sand layer were inferred by fitting the retention tests data as well as by an inverse modelling, applied to the measurements data which were obtained from the landslide test. The curves (the continuous and dashed black lines in **Fig. 6.23**) were obtained in accordance to the Brooks and Corey (Brooks & Corey 1964) and van Genuchten (van Genuchten 1980) models.


Fig. 6.23 Retention curves of the loose sand layer: (a) the relation of the effective saturation with the pressure head; (b) the relation of the relative conductivity with the effective saturation (Lora 2015)

The Brooks and Corey (Brooks & Corey 1964) model appeared to approach better the field data especially in terms of water pressure head and therefore it was the expression that was implemented on the numerical code:

$$\Theta = \left(\frac{h}{h_b} \right)^{-\lambda} \quad \text{and} \quad K(\Theta) = K_s \cdot \Theta^{\frac{2}{\lambda} + l + 2} \quad \text{if } h < h_b \quad (6.16)$$

where $\Theta = \frac{\theta - \theta_r}{\theta_s - \theta_r}$ is the effective saturation, with θ_r and θ_s the residual and the saturated

volumetric water content respectively; h is the water pressure head and h_b the bubbling pressure; $K(\Theta)$ and K_s are the hydraulic conductivity in partially saturated conditions,

respectively; λ and l are shape parameters.

Regarding the clayey layer, the only measured hydraulic parameter was the hydraulic conductivity in saturated conditions. Other unknown parameters concerning the retention curves are assigned from the literature (Carsel & Parrish 1988). The values of the parameters used for the Brooks & Corey retention and relative permeability curves are presented in **Table 7**.

Table 7 Parameters used for the Brooks & Corey retention and relative permeability curves (Brooks & Corey 1964)

Definition	Label	Loose Sand	Clay
Residual water content	$\theta_r[-]$	0.05	0.05
Saturated water content	$\theta_s[-]$	0.578	0.47
Intrinsic permeability	$k [m^2]$	2.091E-11	2.98E-13
Matric potential-air entry value	$h_b[cm]$	-4.805	-23.015
Parameter λ	$\lambda [-]$	0.65	1.57
Parameter l	$l[-]$	0.1008	0.06156

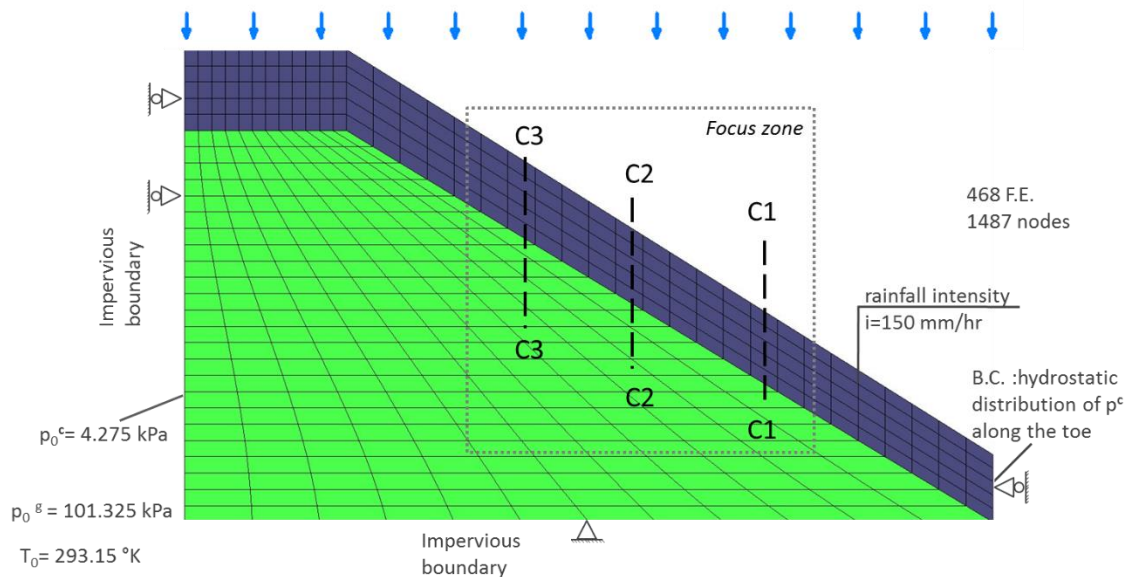


Fig. 6.24 Description of the discretization of the slope, initial and boundary conditions

In **Fig. 6.24** the mesh which has been created, is presented along with the initial and boundary conditions applied to the slope. The finite element mesh is composed of 468 eight-noded quadratic quadrilateral elements. Vertical and horizontal displacements are constrained

at the bottom and horizontal displacements at the lateral surfaces. Initially, the stress state is computed in equilibrium with the gravity load and the initial hydro-thermal conditions (**Fig. 6.24**).

The stress state and the state variables calculated by this first analysis form the initial conditions for the successive run. Subsequently, rainfall infiltration is simulated by means of an imposed boundary flux of 150mm/hr along the upper surface (the rain input has the real value as this that was applied during the experiment). When the toe of the slope saturates, hydrostatic pressure is applied along its vertical side.

Numerical results with the use of the DP model

After 1.8 hr of the applied rainfall, the numerical solution became unstable and the numerical convergence was lost. This was also the actual time failure of the field experiment. **Fig. 6.25** illustrates the contours of degree of saturation nearly at the beginning of the simulation and after 1.8hr, when the convergence of the norm of displacements cannot be achieved any further. In more detail, in **Fig. 6.25a**, it can be observed the procedure of rainfall infiltration: a wetting front percolating vertically downwards, across the sand layer. The wetting front does not saturate the sand in this case as the infiltration capacity is not exceeded by the rainfall intensity. While in **Fig. 6.25b** it can be observed that there has been formed a water table in the fill material (loose sand layer). Once the water front reached the interface between the two layers, a thin seepage layer was formed which started increasing upwards and more precisely from the toe towards the top due to the rainfall integration along the slope.

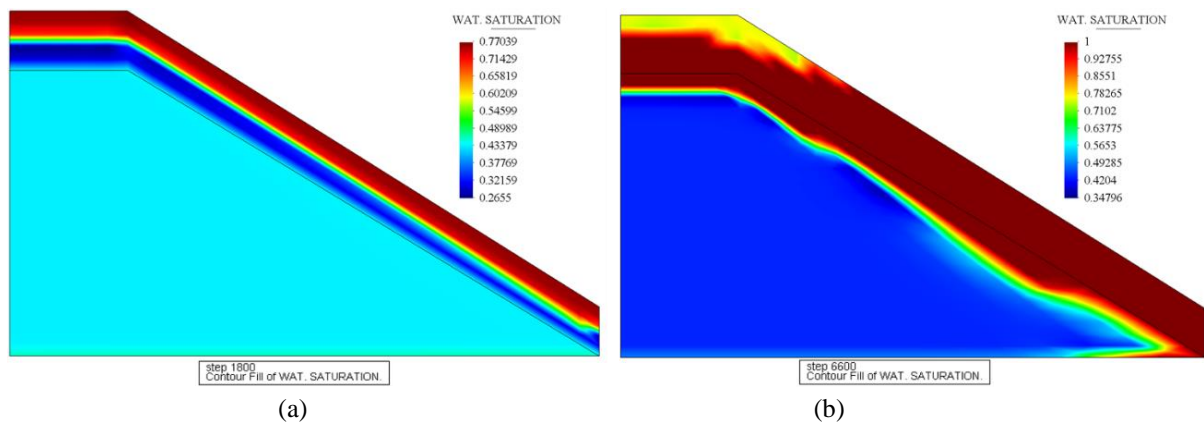


Fig. 6.25 Evolution of the wetting front (a) and the water table (b), during the rainfall infiltration

Only a small fraction was absorbed by the clay layer due to the large difference in the

permeability values between the two layers: in fact the cohesive soil represents an unsaturated permeability barrier in the short time.

The hydraulic response of the model is also depicted in **Fig. 6.26**, through the volumetric water content time evolution at two different positions of the slope; at position 5 (TDR5) near the top of the sand layer and at position 6 (TDR6) near the interface between the two layers.

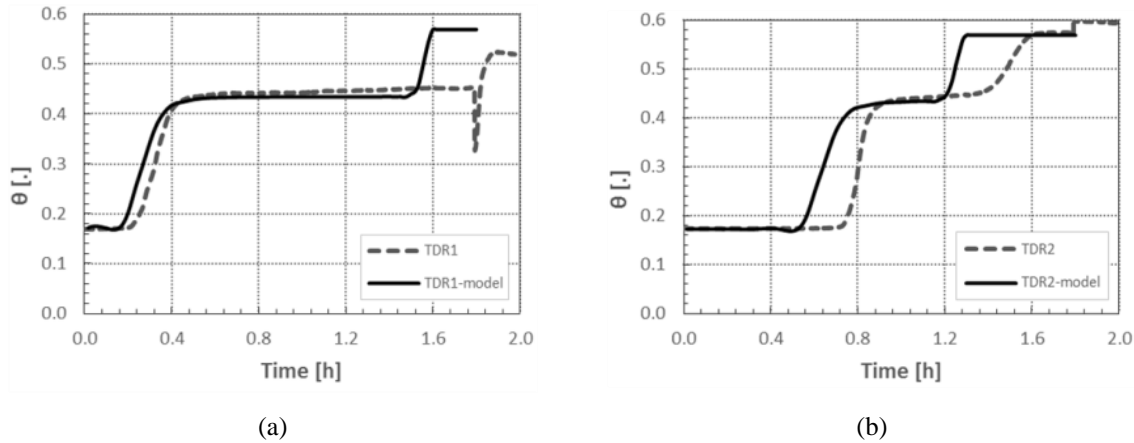


Fig. 6.26 Comparison between computed and in-situ measured volumetric water content at the positions 5 and 6 (TDR5 and TDR6 respectively)

The comparison is shown between the in-situ measurements and the prediction of the model. A two-step evolution is noted: the water content increases from 0.18 to approximately 0.45 and subsequently it increases up again to 0.578. The first rise involves the probes from the top to the bottom while the second one progresses from the bottom to the top. As it can be observed the computed volumetric contents are in a good agreement with the field measurements.

The maximum displacements are concentrated at the lower part of the slope, as illustrated in **Fig. 6.27**. The vectors of the incremental displacements indicate that the sand layer is sliding downwards and that the lower part is also under swelling conditions at the end of the analysis because of the water overpressure and the constrained displacements at the toe. The equivalent plastic strain is also concentrated at the lower part of the slope and coincides with the contours of the second order work (**Fig. 6.27c-d**). The fact that the maximum displacements contour coincides with the contour of the equivalent plastic strains and the second order work contour, indicates that the onset of the failure is located at the lower part of the slope.

This is what is actually expected since it is the most sensitive point of the slope: there concentrates the seepage water within the layer and, at the same time, it is being received the rainfall infiltration water as a flux input from the upper boundary surface. With increasing

water content, the capillary forces acting between the soil particles decrease. This de-bonding effect of wetting is taken into account in the model through Schrefler’s effective stress (Schrefler 1984) $\sigma' = \sigma + [p^g - S^w p^c] \mathbf{1}$ which decreases during rain infiltration and, as a consequence, the soil loses its strength. When the point of significant excess pore water development is reached, there will be little or no effective confining stress acting on the soil. Eventually, the soil state approaches a zone of instability in which the shear strength can decrease significantly. Figures **Fig. 6.28a-b** describe exactly this phenomenon of a probable liquefaction occurrence, as it was captured, indicatively, on node 158 at the lower part of the slope near the surface of the sand layer. Nearly at 1.68 hr the capillary pressure becomes negative (relative water pressure) and it is at that moment that the mean pressure becomes zero. At the same time, the deviatoric stress increases considerably and slightly after (1.78 hr) drops abruptly.

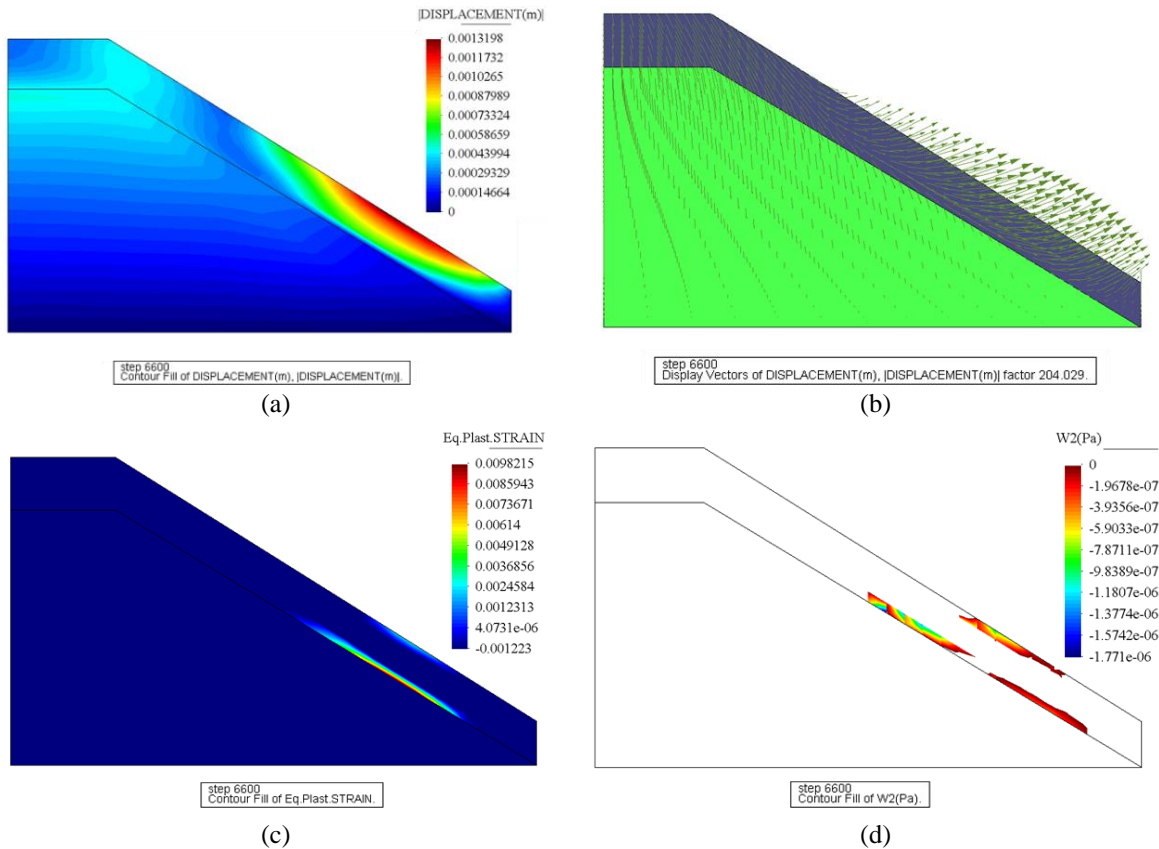


Fig. 6.27 Displacement contours (a) and displacement vectors (b), equivalent plastic strain (c) and second order work contours (d), at the end of the analysis (after 1.8hr of rainfall input)

At the moment of the peak deviatoric stress the equivalent plastic strain begins to develop and it is obtained the first negative value of the second order work at the material point level, as illustrated in **Fig. 6.28c**.

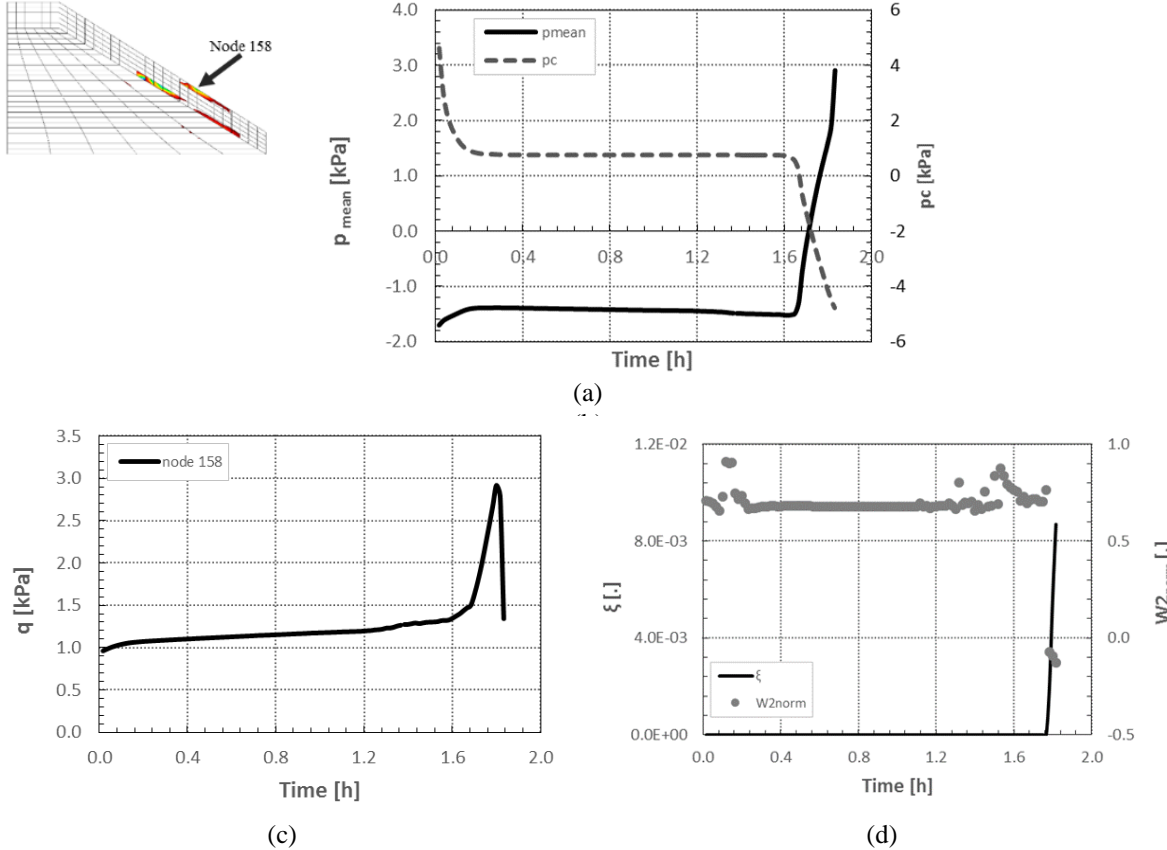


Fig. 6.28 Evolution of: the capillary pressure and the mean stress (a); deviatoric stress (b); equivalent plastic strain and the second order work (c)

Numerical results with the use of the PZ model and comparison

The results which were obtained from the analysis where the PZ model was employed, show us that the global behavior of the slope is described in a more precise way. It is observed that the displacements are distributed along the slope and are greater than the previous obtained with the DP model (**Fig. 6.27a**), with a difference of two orders of magnitude (**Fig. 6.29a**). The displacement vectors (**Fig. 6.29b**) show that the slope is sliding downwards rather than mainly swelling. This is due to the fact that the PZ model is directly dependent on the mean pressure (see eq. (6.7), (6.8) for the elastic moduli and eq. (6.12) of the plastic modulus). The mean pressure has decreased along the slope because of the saturation and so plastic strains develop as we can observe in **Fig. 6.29c**. The displacements which lead to a downward sliding are due

to these strains. The contour of the negative values of the second order work at the end of the analysis is also illustrated in **Fig. 6.29d** and as it can be observed the negative values are distributed along the slope and not only at the lower part.

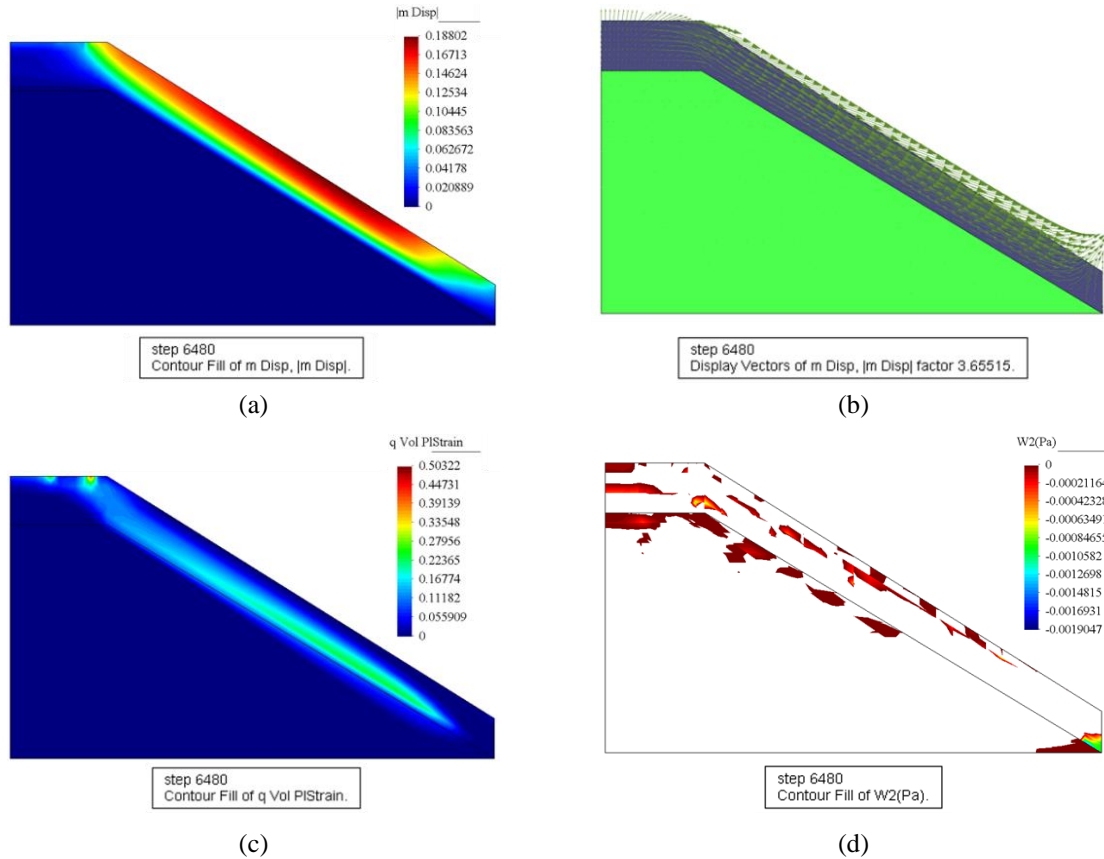


Fig. 6.29 Displacement contours (a) and displacement vectors (b), equivalent plastic strain (c) and second order work contours (d), at the end of the analysis (after 1.8hr of rainfall), using the Pastor-Zienkiewicz model (Pastor et al. 1990)

As it has been observed from the contours, the global behaviour of the slope can be captured with a better agreement with what observed during the experiment when using the PZ model. Thus, we are able now to understand in a better way the mechanisms that take place during infiltration along the slope (and not solely near the toe as before). So, if we go into detail at the TDR points we observe indicatively, at TDR2: at the moment that the water front passes from that point (0.65 hr), the capillary pressure decreases drastically and this corresponds to the first negative value of the W_2 (**Fig. 6.30c, a, e** respectively). At the same time the mean pressure increases, the deviatoric stress reaches a peak value and the volumetric strains are contractant (**Fig. 6.30d, f, b** respectively – 0.65hr) until the moment of saturation (after 1.4 hr), where the capillary pressure decreases and then it becomes negative, W_2 begins to oscillate intensively

between positive and negative values, deviatoric and mean stresses decrease drastically and volumetric strains become positive.

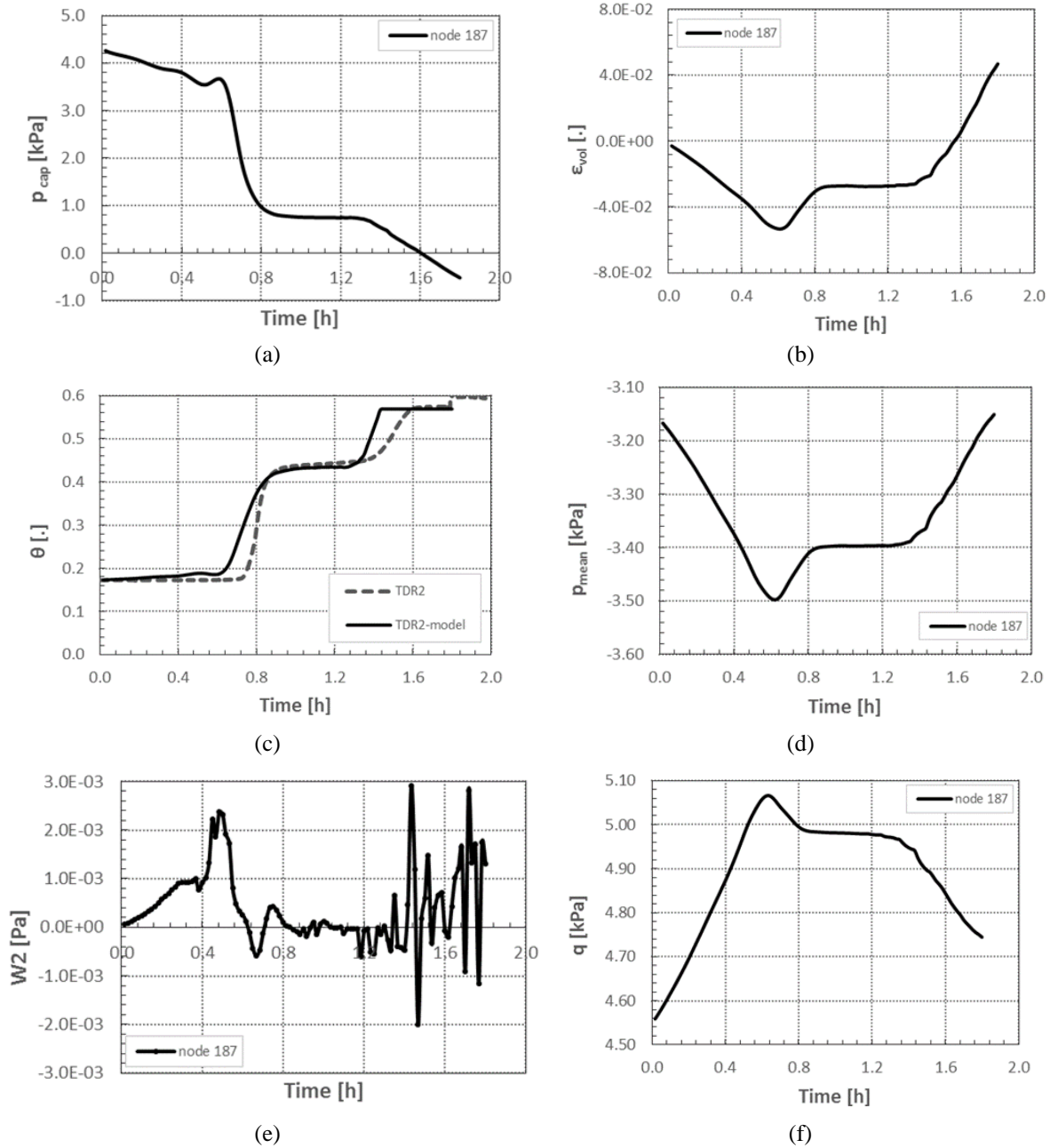


Fig. 6.30 Evolution of the capillary pressure (a), of the volumetric strains (b) of the water saturation degree (c) of the mean (d) of the second order work (e) and of the deviatoric stress at TDR2 (node 187)

7 Conclusions and perspectives for future research

This PhD thesis was devoted to numerical modelling of multi-physics processes in variably saturated slopes subjected to rainfall infiltration. Emphasis was placed on the detection of the onset of failure in rainfall-induced landslides.

To this end, this thesis provided first a synthesis of the major failure modes which prevail in geomaterials and of the main theories which are used in the stability analysis with an extended reference to the second order work criterion which is being investigated throughout this thesis.

Subsequently, the next chapter is presenting the state of knowledge on the fundamental aspects of unsaturated behavior, the physical processes and the failure mechanisms that take place in rainfall-induced landslides. The controlling factors for rain infiltration and pore water pressure changes in unsaturated slopes and the review of the main modelling concepts for the simulation of the failure onset of the rainfall-induced landslides constitute the bridge for chapters 4, 5 and justify the choice of the modelling framework which has been used in this thesis.

The multiphase model for elasto-plastic porous media (and its background) which has been employed for the simulations, is presented in chapters 4, 5 from the mathematical and the numerical point of view.

Finally, this modelling framework has been applied for the finite element analysis of:

- a plane strain compression test of water saturated dense sand and isochoric grain matter, where strain localization is observed;

- the failure initiation of a well-documented flowslide (Sarno-Quindici events, Italy, May 5-6, 1998);
- a large scale experimental test subjected to rainfall infiltration (University of Padova, 2014).

Thesis contributions

The numerical results have pointed out that a sufficiently general coupled model for multiphase geomaterials is capable of modelling a variety of phenomena as strain localization in laboratory tests and the initiation of flowslides, giving results in agreement with experimental or in-situ observations, and can be a powerful tool for the understanding of the triggering mechanisms during the progressive localized or diffused failure (in the first case-plane strain compression test, a regularization procedure should be introduced for mesh objectivity upon mesh refinement, using, e.g., local or non-local visco-plasticity as in (Lazari et al. 2015) but this topic is beyond the scope of this work. In this simulation, the width of the shear band has been fixed by the width of the finite element, with dimension similar to that of the experimental shear band).

The large scale slope experimental test which was carried out at the University of Padova in 2014 by Dr. Eng. Marco Lora is being modelled for the first time. It has been shown in particular that the model can predict the field measurements of the volumetric water content and can also provide us with the necessary mechanical results which indicate the failure mechanisms that take place at the real time of the actual failure. Furthermore, it has been shown that the constitutive model which will be used for the description of the soil mechanical behavior plays a significant role. For a first approximation of the onset of the failure, the DP model can be used. But for a more precise analysis of the global behavior of the slope an advanced constitutive model is needed to be used, suitable for the soil materials that are to be modeled. In this analysis, the Pastor-Zienkiewicz constitutive model (Pastor et al. 1990), suitable for the modelling of sand behavior, was employed, giving more precise results and a better overview of the global mechanical behavior of the slope.

Additionally, in this work, the second order work criterion is implemented in the finite element code for multiphase geomaterials, Comes-Geo, and has been used in the simulations at the material point level to detect the zones with material-point instability in the cases

mentioned above. Three different expressions have been presented, which could be used in case of variably saturated porous materials: the second order work expressed in terms of effective stress, of total stresses and thirdly by taking into account the hydraulic energy contribution (Buscarnera & Prisco 2012) for partially saturated soils.

The finite element results have shown that the set of the local negative values of the second order work computed from the three expressions gives a good indication of the spatial extent of the potentially unstable domains and is consistent with the spatial and time evolution of variables that are usually adopted to detect the occurrence of localized or diffuse unstable zones as the equivalent plastic strain and the displacement and its rate; all expressions seem equivalent, but local values and also spatial extents are different, as expected, with a slightly better agreement for the expression of the second order work in terms of effective stress, W_2 , and that taking into account the hydraulic energy contribution, $W_{2\text{unsat}}$. The numerical results indicate also that the second order work criterion detects the local instability associated with cavitation of the pore water.

Perspectives for future research

To extend these conclusions to the evaluation of the instability of the entire soil mass (the global domain), the value of the second order work obtained by integration on the whole physical domain has to be computed. If this global value is negative, then the entire domain is unstable (Lignon et al. 2009; Laouafa et al. 2011; Prunier et al. 2016) and the global value plays the role of safety factor (see (Prunier et al. 2016) in case of single phase material). When local negative values are obtained with a positive global value, the criterion indicates that the whole slope is still globally stable, possibly approaching to a properly unstable state; in this case, a limited zone with local negative values can indicate local instability and can also be an indication of a possible local failure mechanism.

Further research on the second order work criterion is encouraged, in particular to investigate how this criterion can be related to the global instability and to combine the second order work criterion with the results stemming from the bifurcation analysis for multiphase materials. This is necessary to evaluate separately the contribution of the hydro (capillary pressure/degree of saturation) and mechanical parts (stress/strain). Also the use of advanced

constitutive models for the solid skeleton is encouraged, to take into account the huge variety of the constitutive response of the materials.

8 References

- Aitchison, G.D. & Donald, I.B., 1956. Effective stress in unsaturated soils. In *2nd Australia-New Zealand Conf. Soil Mech.* pp. 192–199.
- Alonso, E.E., Gens, A. & Josa, A., 1990. A constitutive model for partially saturated soils. *Géotechnique*, 40, pp.405–30.
- Anderson, S.P., Dietrich, W.E. & Montgomery, D.R., 1997. Subsurface flow paths in a steep, unchanneled catchment. *Water Resour. Res.*, 33(12), pp.2637–2653.
- Askarinejad, A., 2013. *Failure mechanisms in unsaturated silty sand slopes triggered by rainfall*. ETH Zurich.
- Baggio, P., Bonacina, C. & Strada, M., 1993. Trasporto di calore e di massa nel calcestruzzo cellulare. *La Termotecnica*, 45, pp.53–60.
- Bear, J. & Bachmat, Y., 1984. Transport phenomena in porous media - Basic equations, from Fundamentals of Transport Phenomena in Porous Media. *Nato ASI Series*, pp.5–61.
- Bear, J. & Corapcioglu, Y., 1981. Mathematical model for regional land subsidence due to pumping. 2. Integrated aquifer subsidence equation for vertical and horizontal displacements. *Water Resources Research*, 17, pp.947–958.
- Bianco, M. et al., 2003. A frontal solver tuned for fully coupled non-linear hygro-thermo-mechanical problems. *Int. J. Numer. Meth. Engng.*, 57, pp.1801–1818.
- Bigoni, D. & Hueckel, T., 1991. Int. J. Solids Struct. *Uniqueness and localization. I. Associative and non-associative elastoplasticity*, 28(2), pp.197–213.
- Bilotta, E. et al., 2005. Geotechnical characterization of pyroclastic soils involved in huge flowslides. *Geotech. Geolog. Eng.*, 23, pp.365–402.
- Biot, M.A., 1941a. Consolidation settlement under a rectangular load. *J. Appl. Phys.*, 12,

- pp.426–30.
- Biot, M.A., 1956a. General solution of the equation of elasticity and consolidation for a porous material. *J. Appl. Mech.*, 23, pp.91–6.
- Biot, M.A., 1941b. General theory of three-dimensional consolidation. *J. Appl. Phys.*, 12, pp.155–64.
- Biot, M.A., 1956b. Theory of deformation of a porous viscoelastic anisotropic soil. *J. Appl. Phys.*, 27, pp.459–67.
- Biot, M.A., 1955. Theory of elasticity and consolidation for a porous anisotropic solid. *J. Appl. Phys.*, 26, pp.182–5.
- Biot, M.A., 1963. Theory of stability and consolidation of a porous medium under initial stress. *J. Math. Mech.*, 12, pp.521–41.
- Biot, M.A. & Willis, P.G., 1957. The elastic coefficients of the theory of consolidation. *J. Appl. Mech.*, 24, pp.594–601.
- Bird, R.B., Stewart, E.W. & Lightfoot, E.N., 1960. *Transport Phenomena*, John Wiley & Sons.
- Bishop, A.V., 1959. The principle of effective stress. *Teknisk Ukeblad*, 39, pp.859–863.
- Bishop, A.W., 1955. The use of slip circle in the stability analysis of slopes. *Géotechnique*, 5, pp.7–17.
- Bishop, A.W. & Blight, G.E., 1963. Some aspects of effective stress in saturated and partly saturated soils. *Géotechnique*, 13, pp.177–197.
- de Boer, R. et al., 1991. *Porous media, a survey of different approaches*, Forschungsbericht aus dem Fachbereich Bauwesen, 54, Universität-Gesamthochschule Essen.
- Bolzon, G., Schrefler, B. & Zienkiewicz, O., 1996. Elastoplastic soil constitutive laws generalized to partially saturated states. *Géotechnique*, 46(2), pp.279–289.
- Bomberg, M. & Shirliffe, C.J., 1978. Influence of moisture gradients on heat transfer through porous building materials. Thermal transmission measurements of insulation. In R. P. Tye, ed. *ASTM STP 660*. pp. 211–233.
- Brooks, R.H. & Corey, A.T., 1964. Hydraulic properties of porous media. *Hydrology Papers*, 3(3), p.27.
- Brooks, R.N. & Corey, A.T., 1966. Properties of porous media affecting fluid flow. *J. Irrig. Drain. Div. Am. Soc. Civ. Eng.*, 92(IR2), pp.61–68.
- Buscarnera, G. & Mihalache, C., 2014. Instability of unsaturated soils : A review of theoretical

- methods. *Journal of Geo-Engineering Sciences*, 2, pp.39–65.
- Buscarnera, G. & Prisco, C., 2012. Discussing the definition of the second-order work for unsaturated soils. *International Journal for Numerical and Analytical Methods in Geomechanics*, 36(1), pp.36–49.
- Carsel, R.F. & Parrish, R.S., 1988. Developing joint probability distributions of soil water retention characteristics. *Water Resources*, 24, pp.755–769.
- Cascini, L. et al., 2000. A preliminary model for the landslides of May 1998 in Campania Region. In E. & Picarelli, ed. *Proc, 2nd Int. Symposium on Geotechnics of Hard Soil- Soft Rock*. Napoli: Balkema, pp. 1623–1649.
- Cascini, L. et al., 2009. Modeling of rainfall-induced shallow landslides of the flow-type. *Journal of Geotechnical and Geoenvironmental Engineering*, 136(1), pp.85–98.
- Cascini, L. et al., 2010. Modeling of Rainfall-Induced Shallow Landslides of the Flow-Type. *Journal of Geotechnical and Geoenvironmental Engineering*, 136(1), pp.85–98.
- Cascini, L., 2004. The flowslides of May 1998 in the Campania region, Italy: the scientific emergency management. *Italian Geotechnical Journal*, 2, pp.11–44.
- Cascini, L., Cuomo, S. & Guida, D., 2008. Typical source areas of May 1998 flow-like mass movements in the Campania region, Southern Italy. *Engineering Geology*, 96, pp.107–125.
- Cascini, L., Cuomo, S. & Sorbino, G., 2005. Flow-like mass movements in pyroclastic soils: remarks on the modelling of triggering mechanisms. *Rivista italiana di geotecnica*, (4), pp.11–31. Available at: http://www.associazionegeotecnica.it/sites/default/files/rig/RIG_2005_4_011.pdf.
- Cascini, L., Sorbino, G. & Cuomo, S., 2003. Modelling of flowslides triggering in pyroclastic soils. In L. Picarelli, ed. *Proc. Int. Conference on “Fast Slope Movements— Prediction and Prevention for Risk Mitigation.”* Bologna: Patron, pp. 93–100. Available at: <http://scholar.google.com/scholar?hl=en&btnG=Search&q=intitle:MODELLING+OF+ FLOWSLIDE+TRIGGERING+IN+PYROCLASTIC+SOILS#0>.
- Chambon, R. & Caillerie, D., 1999. Existence and uniqueness theorems for boundary value problems involving incrementally nonlinear models. *Int. J. Solids Struct.*, 36, pp.5089–5099.
- Chen, W.F. & Tsui, Y., 1992. Limitations to the large strain theory. *Int. J. Num. Meth. Eng.*,

- 33, pp.101–114.
- Cho, S.E. & Lee, S.R., 2002. Evaluation of surficial stability for homogeneous slopes considering rainfall characteristics. *Journal of Geotechnical and Geoenvironmental Engineering*, 128(9), pp.756–763.
- Chowdhury, R.N., 1981. Stability analysis of embankments and slopes- discussion. *Journal of the Geotechnical Engineering Division*, 107(5), pp.691–3.
- Coleman, B.D. & Noll, W., 1963. The thermodynamics of elastic materials with heat conduction and viscosity. *Arch. Ration. Mech. Anal.*, 13, pp.168–178.
- Corey, A.T., 1957. Measurement of water and air permeability in unsaturated soil. In *Soil Sci. Soc. Am. Proc.* pp. 7–10.
- Daouadji, A. et al., 2011. Diffuse failure in geomaterials : Experiments, theory and modelling. *International Journal for Numerical and Analytical Methods in Geomechanics*, 35, pp.1731–1773.
- Darve, F. et al., 2007. Bifurcations in granular media: macro- and micro-mechanics approaches. *Comptes Rendus Académie des Sciences Mecanique*, 335, pp.496–515.
- Darve, F. et al., 2004. Failure in geomaterials : continuous and discrete analyses. *Computer methods in applied mechanics and engineering*, 193(27-29), pp.3057–3085.
- Darve, F., Flavigny, E. & Meghachou, M., 1995. Constitutive modeling and instabilities of soil behaviour. *Comput. Geotech*, 17, pp.203–224.
- Darve, F. & Laouafa, F., 2000. Instabilities in granular materials and application to landslides. *Mech. Cohes-Frict. Mater.*, pp.627–652.
- Desrues, J. & Chambon, R., 2002. Shear band analysis and shear moduli calibration. *International Journal of Solids and Structures*, 39, pp.3757–3776.
- Duncan, J.M., 1996. State of the art: limit equilibrium and finite element analysis of slopes. *Journal of Geotechnical Engineering*, 122(7), pp.577–96.
- Ehlers, W., 1989. *Poröse Medien, ein kontinuumsmechanisches Modell auf der Basis der Mischungstheorie*. Universität Gesamthochschule Essen.
- Eichenberger, J., 2013. *Geomechanical modelling of rainfall-induced landslides in partially saturated slopes*. École Polytechnique Fédérale de Lausanne.
- Eringen, A.C. & Suhubi, E.S., 1964. Nonlinear Theory of simple micro-elastic solids. *Int. J. Engng. Sci.*, 2, pp.189–203.

- Espinoza, R., Repetto, P. & Muhunthan, B., 1992. General framework for stability analysis of slopes. *Géotechnique*, 42(4), pp.603–15.
- Fellenius, W., 1936. Calculation of the stability of earth dams. In *2nd International Congress on Large Dams*. Washington.
- Fernandez Merodo, J.A. et al., 2004. Modelling of diffuse failure mechanisms of catastrophic landslides. *Comput. Methods Appl. Mech. Eng.*, 193, pp.2911–2939.
- Fredlund, D., Morgenstern, N. & Widger, R., 1978. The Shear Strength of Unsaturated Soils. *Canadian Geotechnical Journal*, 15(3), pp.313–321.
- Fredlund, D.G., 1998. Bringing unsaturated soil mechanics into engineering practice. In *Second International Conference on Unsaturated Soil Mechanics*. Beijing, pp. 1–36.
- Fredlund, D.G. & Morgenstern, N.R., 1977. Stress state variables for unsaturated soils. *Journal of the geotechnical engineering division*, ASCE 103, pp.447–466.
- Fredlund, D.G. & Rahardjo, H., 1993. *Soil mechanics for unsaturated soils*, John Wiley & Sons.
- Gawin, D., Baggio, P. & Schrefler, B.A., 1995. Coupled heat, water and gas flow in deformable porous media. *I.J. Num. Methods in Fluids*, 20, pp.969–987.
- Gawin, D., Baggio, P. & Schrefler, B.A., 1996. Modelling heat and moisture transfer in deformable porous building materials. *Arch. of Civil Engng*, 42((3)), pp.325–349.
- Gawin, D. & Sanavia, L., 2009. A unified approach to numerical modelling of fully and partially saturated porous materials by considering air dissolved in water. *Computer Modeling in Engineering & Sciences*, 53(3), pp.255–302.
- Gawin, D. & Sanavia, L., 2010. Simulation of cavitation in water saturated porous media considering effects of dissolved air. *Transport in porous media*, 81, pp.141–160.
- Gawin, D. & Schrefler, B.A., 1996. Thermo-hydro-mechanical analysis of partially saturated porous materials. *Engineering Computations*, 13(7), pp.113–143.
- van Genuchten, M.T., 1980. A closed-form equation for predicting the hydraulic conductivity of unsaturated soils. *Soil Science Society of America Journal*, 44(5), pp.892–898.
- Gray, W.G. & Hassanizadeh, M., 1991. Unsaturated flow theory including interfacial phenomena. *Water Resources Research*, 27, pp.1855–1863.
- Gray, W.G. & Hassanizadeh, S.M., 1991. Paradoxes and realities in unsaturated flow theory. *Water Resour. Res.*, 27, pp.1847–1854.

- Griffiths, D. & Lane, P., 1999. Slope stability analysis by finite elements. *Géotechnique*, 49(3), pp.387–403.
- Gudehus, G., 1995. A comprehensive concept for non-saturated granular bodies. In *Proc. 1st Int. Conf. on Unsaturated Soils*. Paris: Balkema Rotterdam.
- Hassanizadeh, M. & Gray, W.G., 1979a. General conservation equations for multi-phase systems: 1. Averaging procedure. *Advances in Water Resources*, 2(C), pp.131–144.
- Hassanizadeh, M. & Gray, W.G., 1979b. General conservation equations for multi-phase systems: 2. Mass, momenta, energy and entropy equations. *Advances in Water Resources*, 2(C), pp.191–203.
- Hassanizadeh, M. & Gray, W.G., 1980. General conservation equations for multi-phase systems: 3. Constitutive theory for porous media flow. *Advances in Water Resources*, 3(1), pp.25–40.
- Hassanizadeh, M. & W.G., G., 1980. General conservation equations for multiphase systems: 3. Constitutive theory for porous media flow. *Adv. Water Resources*, 3, pp.25–40.
- Hassanizadeh, S.M., 1986. Derivation of basic equations of mass transport in porous media, Part. 2 Generalized Darcy's law and Fick's law. *Adv. Water Resources*, 9, pp.207–222.
- Hill, R., 1958. A general theory of uniqueness and stability in elastic-plastic solids. *Journal of the Mechanics and Physics of Solids*, 6(3), pp.239–249.
- Iverson, R.M., 2000. Landslide triggering by rain infiltration. *Water Resources Research*, 36(7), p.1897.
- Janbu, N., 1968. Slope stability computations. In *Soil Mech. and Found. Engrg. Report*. Trondheim, Norway: Technical University of Norway.
- Johnson, K.A. & Sitar, N., 1990. Hydrologic conditions leading to debris-flow initiation. *Can Geotech J/Geotech J*, 27, pp.789–801.
- Kakogiannou, E. et al., 2016. A porous media finite element approach for soil instability including the second-order work criterion. *Acta Geotechnica*, 11(4), pp.805–825. Available at: <http://link.springer.com/10.1007/s11440-016-0473-5>.
- Kakogiannou, E., Lora, M. & Sanavia, L., 2015. Hydro-mechanical continuum modelling of an experimental slope with a material stability criterion. In *Int. Conf. on Particle-based Methods: Fundamentals and Applications – PARTICLES 2015*. Barcelona, pp. 128–139.
- Kasim, F.B., 1997. *Effects of Steady State Rainfall on Long Term Matric Suction Conditions*

- in Slopes*, Saskatoon, Canada: Unsaturated Soils Group, University of Saskatchewan.
- Khoa, H.D.V., 2005. *Modélisation des glissements de terrains comme un problème de bifurcation*. INPG.
- Lade, P.V., 1993. Initiation of static instability in the submarine Nerlerk berm. *Can Geotech J*, 30, pp.895–904.
- Lade, P.V. & de Boer, R., 1997. The concept of effective stress for soil, concrete and rock. *Géotechnique*, 47(1), pp.61–78.
- Lade, P.V. & Pradel, D., 1990. Instability and plastic flow of soils. I: Experimental observations. *J Eng Mech-ASCE*, 116(11), pp.2532–2550.
- Lammers, A.R. & Zurcher, U., 2011. Stability During Arboreal Locomotion. In V. Klika, ed. *Theoretical Biomechanics*.
- Laouafa, F. et al., 2011. Stability in geomechanics, experimental and numerical analyses. *International Journal for Numerical and Analytical Methods in Geomechanics*, 35, pp.112–139.
- Laouafa, F. & Darve, F., 2002. Modelling of slope failure by a material instability mechanism. *Computers and Geotechnics*, 29(4), pp.301–325.
- Lazari, M., Sanavia, L. & Schrefler, B.A., 2015. Local and non-local elasto-viscoplasticity in strain localization analysis of multiphase geomaterials. *International Journal for Numerical and Analytical Methods in Geomechanics*, 39(14), pp.1570–1592.
- Lee, Y.S., Cheuk, C.Y. & Bolton, M.D., 2008. Instability caused by a seepage impediment in layered fill slopes. *Can Geotech J*, 45, pp.1410–1425.
- Leger, A. & Potier-Ferry, M., 1993. Elastic–plastic post-buckling from a heterogeneous state. *Journal of the Mechanics and Physics of Solids*, 41(4), pp.783–807.
- Lemaitre, J. & Chaboche, J., 1988. *Mécanique des matériaux solides* Dunod., Paris.
- Leroy, Y. & Ortiz, M., 1989. Finite element analysis of strain localization in frictional materials. *Int J Numer Anal Meth Geomech*, 13, pp.53–74.
- Leroy, Y., Ortiz, M. & Needleman, A., 1987. A finite element method for strain localized failure analysis. *Computer Methods Appl Mech Eng*, 61, pp.189–224.
- Lewis, R.W. & Schrefler, B.A., 1998. *The Finite Element Method in the Static and Dynamic Deformation and Consolidation of Porous Media* Second., Chichester, UK: John Wiley & Sons.

- Li, X. & Zienkiewicz, O.C., 1992. Multiphase flow in deforming porous media and finite element solutions. *Computers and Structures*, 45, pp.211–227.
- Lignon, S. et al., 2009. Hydro-mechanical modelling of landslides with a material instability criterion. *Géotechnique*, 59(6), pp.513–524.
- Lora, M., 2015. *Rainfall-triggered shallow landslides in a large-scale physical model*. University of Padua.
- Lora, M., Camporese, M. & Salandin, P., 2016a. Design and Performance of a Nozzle Rainfall Simulator for Landslide Triggering Experiments. *Catena*, 140, pp.77–89.
- Lora, M., Camporese, M. & Salandin, P., 2016b. Rainfall-triggered shallow landslides: infiltration dynamics in a physical hillslope model. *Hydrological Processes*.
- Lu, N. & Likos, W.J., 2004. *Unsaturated Soil Mechanics*, New York: John Wiley and Sons.
- Lyapunov, A., 1907. Problème général de la stabilité des mouvements. *Annales de la faculté & des sciences de Toulouse*, 9, pp.203–274.
- Manzanal, D., Pastor, M. & Merodo, J., 2011. No Title Generalized plasticity state parameter-based model for saturated and unsaturated soils. Part II: Unsaturated soil modeling. *International Journal for Numerical and Analytical Methods in Geomechanics*, 35, pp.1899–1917.
- Matsui, T. & San, K.C., 1992. Finite element slope stability analysis by shear strength reduction technique. *Soils and Foundations*, 32(1), pp.59–70.
- Mokni, M. & Desrues, J., 1998. Strain localisation measurements in undrained plane-strain biaxial tests on Hostun RF sand. *Mechanics of Cohesive-Frictional Materials*, 4, pp.419–441.
- Molenkamp, F., 1986. Limits to the Jaumann stress rate. *Int. J. Num. Anal. Meth. Geomech.*, 10, pp.151–176.
- Moran, M.J. & Shapiro, H.N., 1993. *Fundamentals of Engineering Thermodynamics* 2nd ed., New York: J. Wiley.
- Morgenstern, N.R. & Price, V.E., 1965. The analysis of the stability of general slip surfaces. *Géotechnique*, 15(1), pp.79–93.
- Morland, L.W., 1972. A simple constitutive theory for a fluid saturated porous solid. *Journal Geophys. Res.*, 77, pp.890–900.
- Nguyen, Q., 1987. Bifurcation and post-bifurcation analysis in plasticity and brittle fracture.

- Journal of the Mechanics and Physics of Solids*, 33, pp.303–324.
- Nicot, F., Daouadji, A. & Laouafa, F., 2011. Second-order work , kinetic energy and diffuse failure in granular materials. *Granular Matter*, 13(1), pp.19–28.
- Nicot, F. & Darve, F., 2007. A micro-mechanical investigation of bifurcation in granular materials. *International Journal of Solids and Structures*, 44(20), pp.6630–6652.
- Nicot, F. & Darve, F., 2011. Diffuse and localized failure modes : Two competing mechanisms. *Int. J. Numer. Anal. Meth. Geomech.*, 35, pp.586–601.
- Nicot, F., Darve, F. & Khoa, H.D. V, 2007. Bifurcation and second-order work in geomaterials. *International Journal for Numerical and Analytical Methods in Geomechanics*, 31, pp.1007–1032.
- Nova, R., 1994. Controllability of the incremental response of soil specimens subjected to arbitrary loading programmes. *Journal of the Mechanical Behavior of Materials*, 5(2), pp.193–201.
- Nuth, M. & Laloui, L., 2008. Effective stress concept in unsaturated soils: Clarification and validation of a unified framework. *Int J Numer Anal Meth Geomech*, 32, pp.771–801.
- Organisation ASHRAE, 1993. *Handbook, Fundamentals Volume*, Atlanta: ASHRAE.
- Pastor, M. et al., 2004. Modelling of landslides: (I). Failure mechanisms. In F. Darve & I. Vardoulakis, eds. *Degradations and instabilities in geomaterials, CISM course and lectures No. 461*. New York: Springer, pp. 287–317.
- Pastor, M. et al., 2002. Modelling tailing dams and mine waste dumps failures. *Geotechnique*, 52(8), pp.579–591.
- Pastor, M., Zienkiewicz, O. & Chan, A., 1990. Generalized plasticity and the modelling of soil behaviour. *International Journal for Numerical and Analytical Methods in Geomechanics*, 14(3), pp.151–190.
- Petryk, H., 1993. Theory of bifurcation and instability in time-independent plasticity. In Q. S. Nguyen, ed. *Bifurcation and Stability of Dissipative Systems, CISM Courses and Lecturers*. Springer, pp. 95–152.
- Pradel, D. & Raad, G., 1993. Effect of permeability on surficial stability of homogeneous slopes. *Journal of Geotechnical Engineering*, 109(1), pp.62–70.
- Prunier, F. et al., 2016. Designing geotechnical structures with a proper stability criterion as a safety factor. *Computers and Geotechnics*, 71, pp.98–114. Available at:

- <http://dx.doi.org/10.1016/j.compgeo.2015.09.007>.
- Rahardjo, H. et al., 2007. Factors controlling instability of homogeneous soil slopes under rainfall. *Journal of Geotechnical and Geoenvironmental Engineering*, 133(12), pp.1532–1543.
- Regueiro, R.A. & Borja, R.I., 1999. A finite element model of localized deformation in frictional materials taking a strong discontinuity approach. *Finite Elements in Analysis and Design*, 33, pp.283–315.
- Rice, J., 1976. The localization of plastic deformation. In *Theoretical and Applied Mechanics*. North-Holland: Amsterdam, pp. 207–220.
- Rudnicki, J.W. & Rice, J.R., 1975. Conditions for the localization of deformation in pressure sensitive dilatant materials. *J Mech Phys Solids*, 23, pp.371–94.
- Sampaio, R. & Williams, W.O., 1979. Thermodynamics of diffusing mixtures. *Journal de Mécanique*, 18, pp.19–45.
- Sanavia, L. et al., 2008. Finite element modelling of thermo-elasto-plastic water saturated porous materials. *Journal of Theoretical and Applied Mechanics*, 38(1-2), pp.7–24.
- Sanavia, L., 2009. Numerical modelling of a slope stability test by means of porous media mechanics. *Engineering Computations*, 26(3), pp.245–266. Available at: <http://www.emeraldinsight.com/10.1108/02644400910943608>.
- Sanavia, L., Pesavento, F. & Schrefler, B.A., 2006. Finite element analysis of non-isothermal multiphase geomaterials with application to strain localization simulation. *Computational Mechanics*, 37(4), pp.331–348.
- Sanavia, L., Schrefler, B.A. & Steinmann, P., 2002. A formulation for an unsaturated porous medium undergoing large inelastic strains. *Comput. Mech.*, 28, pp.137–151.
- Schrefler, B.A., 1984. *The finite element method in soil consolidation (with applications to surface subsidence)*. University College of Swansea.
- Schrefler, B.A. & Gawin, D., 1996. The effective stress principle: incremental or finite form? *Int. J. for Num. and Anal. Meth. in Geomechanics*, 20(11), pp.785–815.
- Schrefler, B.A., Zhan, X. & Simoni, L., 1995. A coupled model for water flow, airflow and heat flow in deformable porous media. *I.J. Heat and Fluid Flow*, 5, pp.531–547.
- Schrefler, B.A. & Zhan, X.Y., 1993. A fully coupled model for water flow and airflow in deformable porous media. *Water Resour. Res.*, 29, pp.155–167.

- Servant, G. et al., 2005. Diffuse modes of failure in geomaterials. In H. Di Benedetto, ed. *Deformation characteristics in geomaterials*. Lieden; New York: A.A. Balkema, pp. 181–200.
- Sibille, L. et al., 2015. Granular plasticity, a contribution from discrete mechanics. *J. Mechanics and Physics of Solids*, 75, pp.119–139.
- Simoni, L. & Schrefler, B.A., 1989. F.E. solution of a vertically averaged model for regional land subsidence. *Int. J. Num. Meth. Eng.*, 27, pp.215–230.
- Skempton, A.W., 1961. Effective stress in soil, concrete and rocks. In *Pore Pressure and Suction in Soils*. Butterworths London, pp. 4–16.
- Sorbino, G. & Foresta, V., 2002. Unsaturated hydraulic characteristics of pyroclastic soils. In *Proc., 3rd Int. Conf. on Unsaturated Soils*. Lisse: Swets and Zeitlinger, pp. 405–410.
- Spencer, E., 1967. A method of analysis of the stability of embankments assuming parallel interslice forces. *Géotechnique*, 17(1), pp.11–26.
- Springman, S.M. et al., 2012. Lessons learnt from field investigations in potentially unstable slopes in Switzerland. *Slovenian Geotechnical Journal*, 9(1), pp.5–29.
- Swanson, F.J. & Swanston, D.N., 1977. Complex mass-movement terrains in the western Cascade Range, Oregon. *Reviews in Engineering Geology*, 3, pp.113–124.
- Take, W.A. et al., 2004. Evaluation of landslide triggering mechanisms in model fill slopes. *Landslides*, 1(3), pp.173–184.
- Tarantino, A., 2010. Basic concepts in the mechanics and hydraulics of unsaturated geomaterials. In L. Laloui, ed. *New Trends in the Mechanics of Unsaturated Geomaterials*. John Wiley & Sons.
- Tavenas, F., Trak, B. & Leroueil, S., 1980. Remarks on the validity of stability analysis. *Can Geotech J*, 17, pp.61–73.
- Taylor DW., 1948. *Fundamentals of soil mechanics*, New York: John Wiley & Sons.
- Terzaghi, K., 1936. The Shearing Resistance of Saturated Soils. In *1st International Conference for SoilMechanics and Foundation Engineering*. Cambridge.
- Tsaparas, I. et al., 2002. Controlling parameters for rainfall-induced landslides. *Computers and Geotechnics*, 29(1), pp.1–27.
- Vardoulakis, I., Goldscheider, M. & Gudehus, G., 1978. Formation of shear bands in sand bodies as a bifurcation problem. *Int. J. Numer. Anal. Meth. Geomech*, 2(2), pp.99–128.

- Vardoulakis, I. & Sulem, J., 1995. *Bifurcation Analysis in Geomechanics*, London: Chapman & Hall Publisher.
- De Vita, P. et al., 2006. Distribution, hydrogeological features and landslide hazard of pyroclastic soils on carbonate slopes in the area surrounding Mount Somma- Vesuvius (Italy). *Italian Journal of Engineering Geology and Environment*, 1, pp.75–98.
- Wheeler, S.J., Sharma, R.S. & Buisson, M.S.R., 2003. Coupling of hydraulic hysteresis and stress-strain behaviour in unsaturated soils. *Géotechnique*, 53(1), pp.41–54.
- Zhang, L. et al., 2004. Numerical study of soil conditions under which matric suction can be maintained. *Canadian Geotechnical Journal*, 41(4), pp.569–582.
- Zhang, L.L., Zhang, L.M. & Tang, W.H., 2005. Rainfall-induced slope failure considering variability of soil properties. *Géotechnique*, 55(2), pp.183–188.
- Zienkiewicz, O.C. et al., 1990. Static and dynamic behaviour of soils: a rational approach for quantitative solutions. II Semi-saturated problems. In *Proc. R. Soc. London*. pp. 311–321.
- Zienkiewicz, O.C. & Mroz, Z., 1984. Generalized plasticity formulation and applications to geomechanics. In C. S. Desai & R. H. Gallagher, eds. *Mechanics of Engineering Materials*. Chichester: Wiley, pp. 655–679.
- Zienkiewicz, O.C. & Shiomi, T., 1985. Dynamic behaviour of saturated porous media: the general Biot's formulation and its numerical solution. *Int. J. Num. Anal. Meth. Geom.*, 5, pp.71–96.
- Zienkiewicz, O.C. & Taylor, R.L., 1989. *The Finite Element Method*, Vol. 1 4th ed., London: Mc Graw Hill.
- Zienkiewicz, O.C. & Taylor, R.L., 1991. *The Finite Element Method*, Vol. 2 4th ed., London: Mc Graw Hill.